ISSN Application No. 21818

Journal of Mechanics and Structure

Volume No. 13

Issue No. 1

January - April 2025

ENRICHED PUBLICATIONS PVT.LTD

JE - 18,Gupta Colony, Khirki Extn,
Malviya Nagar, New Delhi - 110017.
E- Mail: info@enrichedpublication.com
Phone :- +91-8877340707

Journal of Mechanics and Structure

Aims and Scope

Journal of Mechanics and Structure is a journal which offers prompt publication of structural design; this journal publishes peer-reviewed technical papers on state-of-the-art topics and future developments of the profession. Engineers, consultants, and professors detail the physical properties of engineering materials (such as steel, concrete, and wood), develop methods of analysis, and examine the relative merits of various types of structures and methods of fabrication. Subjects include the design, erection, and safety of structures ranging from bridge to transmission towers and tall buildings; technical information on outstanding, innovative, and unique projects; and the impact of natural disasters and recommendations for damage mitigation.

Journal of Mechanics and Structure

Dr. Pabitra Rajbongshi Asso. Prof. Civil Engineering Dept. NIT Silchar E-mail: prajbongshi@yahoo.com	**Mohd. Masroor Alam** Asso. Prof. Engineering Geology Dept. of Civil Engineering Aligarh Muslim University masroor8497@rediffmail.com

Journal of Mechanics and Structure

(Volume No. 13, Issue No. 1, January - April 2025)

Contents

NUMERICAL LINEAR STABILITY ANALYSIS OF A THERMOCAPILLARY-DRIVEN LIQUID BRIDGE WITH MAGNETIC STABILIZATION

YUE HUANG AND BRENT C. HOUCHENS

ABSTRACT

A full-zone model of a thermocapillary-driven liquid bridge exposed to a steady, axial magnetic field is investigated using a global spectral collocation method for low-Prandtl number (Pr) fluids. Flow insta bilities are identified using normal-mode linear stability analyses. This work presents several numerical issues that commonly arise when using spectral collocation methods and linear stability analyses in the solution of a wide range of partial differential equations. In particular, effects such as discontinuous boundary condition regularization, identification of spurious eigenvalues, and the use of pseudospectra to investigate the robustness of the stability analysis are addressed. Physically, this work provides sim ulations in the practical range of experimentally utilized magnetic field stabilization in optically heated float-zone crystal growth. A second-order vorticity transport formulation enables modeling of the liquid bridge up to these intermediate magnetic field strength ranges, measured by the Hartmann number (Ha). The thermocapillary driving and magnetic stabilization effects are observed up to Ha = 500 for Pr = 0.001 and up to Ha = 300 for Pr = 0.02. Prandtl number effects on temperature and flow fields are investigated within $Pr \in (10^{-12}, 0.0667)$ *and indicate that Pr = 0.001 is a good representation of the base state in the* $Pr \to 0$ *limit, at least up to Ha = 300.*

1. Introduction

Float-zone growth processes are methods to grow crystals with the highest purity. A cross-sectional region of a polycrystalline ingot is melted by lateral heating, for example, in an optical heating furnace [Eyer et al. 1979]. This molten region holds itself from spilling by surface tension, forming a liquid bridge between the feed rod and the grown crystal. As the liquid bridge moves through the furnace, the melt resolidifies as a single crystal if properly controlled. Throughout the process the melt never contacts a crucible, and therefore the grown crystal has very low oxygen contamination. Sufficient heat input is required to avoid the onset of morphological instability at the solidification front [Davis 1993]. The thermocapillary effect at the free surface drives a flow within the liquid bridge. This flow is susceptible to instabilities, which result in structural imperfections in grown crystals and uneven dopant distribution for doped crystals [Eyer et al. 1985; Cröll et al. 1994]. Therefore stabilization techniques are typically used in crystal growth practice. For example, two silicon crystal rods were grown in a double ellipsoidal mirror furnace with rod rotation in Spacelab-1 [Martinez and Eyer 1986]. A review of liquid bridge stabilization strategies can be found in [Lappa 2005b]. One strategy for molten semiconductors, which have properties similar to liquid metals, is to apply external magnetic fields to control flow

motion.

YUE HUANG AND BRENT C. HOUCHENS

The optically heated liquid bridge has been studied by the crystal growth community using simpler models such as the half-zone model, resembling one half of a liquid bridge, and the full-zone model. The liquid bridge has a barrel shape in microgravity and a sagged shape under terrestrial conditions. These free-surface shapes have been simulated in both half-zone [Morthland and Walker 1996] and full-zone [Lappa 2004] models, respectively. In [Nakamura et al. 1998], m = 1 and 2 oscillating instability modes were observed in molten silicon in an optically heated half-zone configuration on the TR-IA rocket. The hydrodynamic and hydrothermal instability mechanisms of low and high-Pr liquid bridges, respectively, have been confirmed in [Chen et al. 1997; Lappa 2005a; Bouizi et al. 2007] and elsewhere. Lan and Yeh [2004; 2005] performed quite complete full-zone modeling involving three-dimensional radiation, a deformable free surface and melting interfaces, dopant distribution, and axial and transverse magnetic damping. Prange et al. [1999] studied the half-zone instability with axial magnetic field stabilization up to Ha = 25.

This work presents a full-zone liquid bridge model with magnetic stabilization, with a focus on the numerical methods and analyses utilized. The goals of this paper are twofold: first, to provide insight into magnetohydrodynamic control in the liquid bridge problem which will aid in the design of floatzone crystal growth experiments and, second, to demonstrate through example the treatment of several common numerical issues, such as regularization, identification of spurious eigenvalues, and sensitivity of linear stability analyses as quantified by pseudospectral analysis, techniques relevant to a wide array of numerical analysis studies.

2. Problem description

2A. Full-zone model of a liquid bridge. A liquid bridge of a molten semiconductor is bounded by top and bottom solid boundaries (Figure 1). Both boundaries are assumed flat, electrically insulating, and at the melting temperature T^*_0 of the semiconductor. The lateral cylindrical free surface is assumed nondeformable due to high surface tension and the microgravity environment. The diameter and height

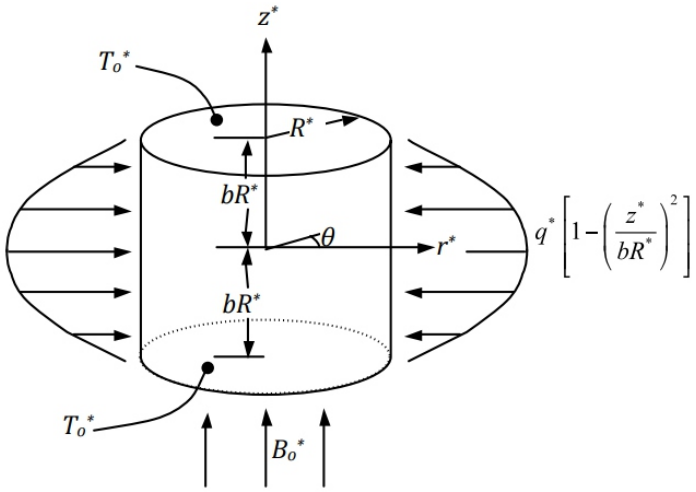

Figure 1. Full-zone model of a liquid bridge with a parabolic heat flux at the free surface and an axially applied magnetic field.

of the liquid bridge are *2R** and *2bR** respectively. The aspect ratio b is held at 1 in this paper. An axisymmetric heat flux is applied at the lateral free surface. This heat flux is approximated with a maximum intensity *q** at the equatorial plane and parabolic reduction to zero at the top and bottom boundaries. The thermal conductivity of the melt is *k**. A constant, uniform external magnetic field is applied in the axial direction with a magnetic flux density of $\boldsymbol{B}^* = \boldsymbol{B}^* o e\hat{}z$. Variables with an asterisk superscript are dimensional quantities.

The characteristic length, temperature, and magnetic flux density are R^*, $\Delta T^* = q^* R^*/k^*$, and B_o^*, respectively. Temperature is scaled as $T = (T^* - T_0^*)/\Delta T^*$. The nondimensional governing equations are incompressible continuity, the Navier–Stokes equations including the electromagnetic body force, the energy equation neglecting viscous dissipation, conservation of charge, and Ohm's law:

$$\nabla \cdot \boldsymbol{v} = 0, \tag{2-1}$$

$$\frac{\partial \boldsymbol{v}}{\partial t} + (\boldsymbol{v} \cdot \nabla)\boldsymbol{v} = -\nabla P + \nabla^2 \boldsymbol{v} + \mathrm{Ha}^2(\boldsymbol{j} \times \hat{\boldsymbol{e}}_z), \tag{2-2}$$

$$\mathrm{Pr}\left[\frac{\partial T}{\partial t} + (\boldsymbol{v} \cdot \nabla)T\right] = \nabla^2 T, \tag{2-3}$$

$$\nabla \cdot \boldsymbol{j} = 0, \tag{2-4}$$

$$\boldsymbol{j} = -\nabla\phi + \boldsymbol{v} \times \hat{\boldsymbol{e}}_z, \tag{2-5}$$

where

$$\mathrm{Ha} = \left(\frac{\sigma^*}{\mu^*}\right)^{\frac{1}{2}} B_o^* R^*, \qquad \mathrm{Pr} = \frac{\mu^* c_p^*}{k^*}. \tag{2-6}$$

The Hartmann number Ha is proportional to the magnetic flux density B*o and measures the ratio of the electromagnetic body forces to the viscous forces. The Prandtl number Pr indicates the relative

effectiveness of thermal convection to heat conduction in the melt. Pr is a material property, where c_p^* is the specific heat of the melt. For fluids with small Prandtl number (for example, $\mathrm{Pr}_{\mathrm{silicon}} \approx 0.02$), heat conduction is dominant over convection.

Nondimensional boundary conditions include a nondeformable and electrically insulating free surface ($v_r = 0$ and $j_r = 0$ at $r = 1$) with flow induced by the thermocapillary boundary conditions, (2-9), and no-slip, no-penetration and electrically insulating top and bottom boundaries ($\boldsymbol{v} = 0$ and $j_z = 0$ at $z = \pm b$) which are maintained at the melting temperature ($T = 0$ at $z = \pm b$).

The full-zone is a more realistic liquid bridge model for optically heated float-zone crystal growth as compared to the half-zone, though both capture much of the primary physics of the flow field. In the full-zone model the heat flux is input on the free surface, rather than from a hot bottom wall, as in the half-zone. Also, no constraint is enforced at the midplane in the full-zone. Thus the temperature varies at the midplane (see Figures 4a and 4b) and flow is allowed to be nonzero and even cross the midplane (see Figure 6). Note that in this work axial symmetry is assumed in the base flow for computational efficiency, but no boundary condition is imposed at the midplane. Therefore the full-zone character is maintained.

In contrast, the half-zone intends to model one half of the liquid bridge. A no-slip, no-penetration solid boundary at fixed temperature is enforced in the half-zone, at the location of the midplane. A thermally insulating free surface is commonly assumed. The half-zone is driven by the temperature difference between two bounding disks. Despite these simplifications, the half-zone is an effective liquid bridge model for both experimental and computational studies. However, the onset of flow instabilities tend to be delayed in the half-zone by the presence of the no-slip boundary that replaces the midplane and removes momentum from the flow through viscous effects. An extensive comparison of the half-zone and full-zone models can be found in [Houchens and Walker 2005].

2B. Thermocapillary-driven flow. The temperature gradient at the free surface produces surface tension differences, called the thermocapillary or Marangoni effect. The surface tension γ^* drives a flow within the liquid bridge, and is approximated as a linearly decreasing function of temperature:

$$\gamma^*(T^*) = \gamma_0^* + \frac{d\gamma^*}{dT^*}(T^* - T_0^*), \tag{2-7}$$

where $d\gamma^*/dT^*$ is a negative quantity. With the Newtonian constitutive relations

$$\tau_{rz}^* = \mu^*\left(\frac{\partial v_z^*}{\partial r^*} + \frac{\partial v_r^*}{\partial z^*}\right), \qquad \tau_{r\theta}^* = \mu^*\left[r^*\frac{\partial}{\partial r^*}\left(\frac{v_\theta^*}{r^*}\right) + \frac{1}{r^*}\frac{\partial v_r^*}{\partial \theta}\right], \tag{2-8}$$

the nondimensional thermocapillary boundary conditions become

$$\frac{\partial v_z}{\partial r} = -\mathrm{Re}_{\mathrm{FZ}}\frac{\partial T}{\partial z} \quad \text{at} \quad r = 1, \qquad \frac{\partial v_\theta}{\partial r} - \frac{v_\theta}{r} = -\mathrm{Re}_{\mathrm{FZ}}\frac{1}{r}\frac{\partial T}{\partial \theta} \quad \text{at} \quad r = 1, \tag{2-9}$$

where

$$\mathrm{Re}_{\mathrm{FZ}} = \frac{\left|\frac{d\gamma^*}{dT^*}\right|\Delta T^*}{\mu^* V_c^*} = \frac{\rho^* R^* \left|\frac{d\gamma^*}{dT^*}\right|\Delta T^*}{\mu^{*2}}. \tag{2-10}$$

The thermocapillary Reynolds number $\mathrm{Re}_{\mathrm{FZ}}$ measures the thermocapillary effect. The subscript FZ refers to the full-zone model temperature scaling. The related Marangoni number $\mathrm{Ma} = \mathrm{Re}_{\mathrm{FZ}} \times \mathrm{Pr}$ is also commonly used in thermocapillary flow studies. The viscous Reynolds number is

$$\mathrm{Re}_{\mathrm{viscous}} = \frac{\rho^* v_{\max}^* R^*}{\mu^*} = \frac{\rho^* v_{\max} V_c^* R^*}{\mu^*} = v_{\max}, \tag{2-11}$$

where $V_c^* = \mu^*/(\rho^* R^*)$ is the characteristic flow velocity. Thus the maximum dimensionless velocity $v_{\max}$ is equivalent to the viscous Reynolds number in this scaling.

Figure 2 shows the thermocapillary-driven flow in $r \in (0, 1)$, $z \in (0, b)$ at some θ plane. From $z = 0 \rightarrow 1$ the temperature decreases along the free surface ($r = 1$), and therefore the surface tension increases. The thermocapillary effect pulls fluid from the equatorial plane toward the top boundary along the free surface. This flow then hits the top boundary, turns inwards and circulates back to the equatorial plane in the interior of the liquid bridge.

3. Steady axisymmetric base flow

3A. ***Base flow assumptions.*** Periodic and/or three-dimensional flow in the liquid bridge results in imperfections in grown crystals such as striations and nonuniform dopant distribution. With sufficient magnetic stabilization, the base flow is steady ($\partial/\partial t = 0$), axisymmetric ($\partial/\partial\theta = 0$) with zero azimuthal velocity

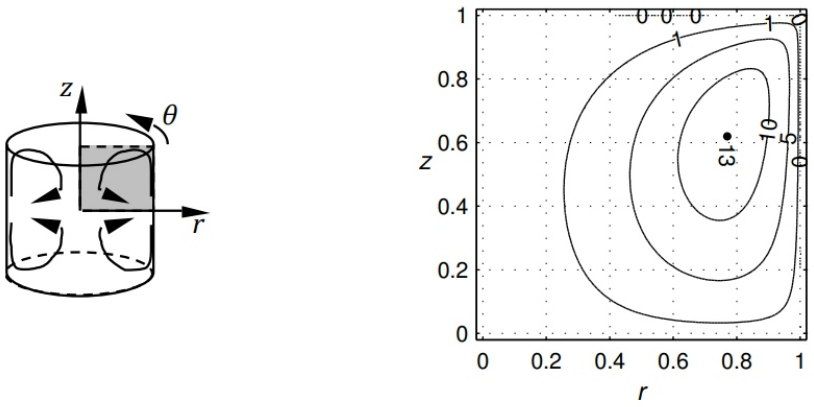

Figure 2. Stream function contours of the thermocapillary-driven flow (Pr = 0.02, Ha = 0, at the critical $\mathrm{Re}_{\mathrm{FZ}} = 1546.58$, flow grid $r \times z = 35 \times 45$, temperature grid $r \times z = 30 \times 30$, $\alpha = 300$).

($v\theta 0 = 0$), and exhibits axial symmetry about the equatorial plane. For this base flow state the governing equations simplify to

$$\frac{\partial v_{r0}}{\partial r}+\frac{v_{r0}}{r}+\frac{\partial v_{z0}}{\partial z}=0, \tag{3-1}$$

$$v_{r0}\frac{\partial v_{r0}}{\partial r}+v_{z0}\frac{\partial v_{r0}}{\partial z}=-\frac{\partial P_0}{\partial r}+\frac{\partial^2 v_{r0}}{\partial r^2}+\frac{1}{r}\frac{\partial v_{r0}}{\partial r}-\frac{v_{r0}}{r^2}+\frac{\partial^2 v_{r0}}{\partial z^2}-\mathrm{Ha}^2 v_{r0}, \tag{3-2}$$

$$v_{r0}\frac{\partial v_{z0}}{\partial r}+v_{z0}\frac{\partial v_{z0}}{\partial z}=-\frac{\partial P_0}{\partial z}+\frac{\partial^2 v_{z0}}{\partial r^2}+\frac{1}{r}\frac{\partial v_{z0}}{\partial r}+\frac{\partial^2 v_{z0}}{\partial z^2}, \tag{3-3}$$

$$\mathrm{Pr}\left(v_{r0}\frac{\partial T_0}{\partial r}+v_{z0}\frac{\partial T_0}{\partial z}\right)=\frac{\partial^2 T_0}{\partial r^2}+\frac{1}{r}\frac{\partial T_0}{\partial r}+\frac{\partial^2 T_0}{\partial z^2}, \tag{3-4}$$

with boundary conditions

$$v_{r0}=0, \quad j_{r0}=0, \quad \frac{\partial v_{z0}}{\partial r}=-\mathrm{Re}_{\mathrm{FZ}}\frac{\partial T_0}{\partial z}F(z), \quad \frac{\partial T_0}{\partial r}=1-\left(\frac{z}{b}\right)^2 \quad \text{at } r=1, \tag{3-5}$$

$$v_{r0}=0, \quad v_{z0}=0, \quad T_0=0, \quad j_{z0}=0 \quad \text{at } z=\pm b, \tag{3-6}$$

where

$$F(z)=1-\exp\left\{-\alpha\left[1-\left(\frac{z}{b}\right)^2\right]^2\right\} \tag{3-7}$$

is a regularization function to remove the ∂vz0/∂r singularity at (r,z) = (1, ±b) between the thermocapil lary driving force on the free surface and the no-penetration conditions at the top and bottom boundaries. Base flow variables are denoted with subscript 0 to differentiate them from perturbation variables(which have subscript 1).

3B. Second-order vorticity transport formulation. In [Houchens and Walker 2005], a fourth-order stream function formulation was introduced for the base flow problem, with the stream function ψ defined as

$$v_{r0}=\frac{1}{r}\frac{\partial \psi}{\partial z}, \qquad v_{z0}=-\frac{1}{r}\frac{\partial \psi}{\partial r}. \tag{3-8}$$

The resulting equations were discretized using a global spectral collocation method with Chebyshev basis functions. In this formulation, the momentum equations can be combined into a single fourth-order partial differential equation governing ψ. Unfortunately, the coefficients on the derivatives of the Cheby shev functions increase dramatically as the derivative order increases. From a numerical standpoint, the combination of order-one coefficients on the first and second derivatives and huge third and fourth derivatives in one equation causes numerical difficulties. This imbalance in fact imposes a constraint on the maximum viable grid resolution in obtaining converged solutions. This consequently limited the maximum magnetic stabilization intensity (Ha) that could be studied [Houchens and Walker 2001].
Reducing the maximum Chebyshev derivative order improves the numerical performance, at the ex pense of more dependent variables. In this work, this is achieved by introducing the azimuthal vorticity ωθ into the formulation as

$$\omega_\theta = \frac{\partial v_{r0}}{\partial z} - \frac{\partial v_{z0}}{\partial r}. \tag{3-9}$$

The nondimensional governing equations of the second-order vorticity transport formulation are

$$\omega_\theta = \frac{1}{r}\frac{\partial^2 \psi}{\partial r^2} - \frac{1}{r^2}\frac{\partial \psi}{\partial r} + \frac{1}{r}\frac{\partial^2 \psi}{\partial z^2}, \tag{3-10}$$

$$\frac{1}{r}\frac{\partial \psi}{\partial z}\left[\frac{\partial \omega_\theta}{\partial r} - \frac{\omega_\theta}{r}\right] - \frac{1}{r}\frac{\partial \psi}{\partial r}\left[\frac{\partial \omega_\theta}{\partial z}\right] = \frac{\partial^2 \omega_\theta}{\partial r^2} + \frac{1}{r}\frac{\partial \omega_\theta}{\partial r} + \frac{\partial^2 \omega_\theta}{\partial z^2} - \frac{\omega_\theta}{r^2} - \frac{\mathrm{Ha}^2}{r}\frac{\partial^2 \psi}{\partial z^2}, \tag{3-11}$$

$$\mathrm{Pr}\left(\frac{1}{r}\frac{\partial \psi}{\partial z}\frac{\partial T_0}{\partial r} - \frac{1}{r}\frac{\partial \psi}{\partial r}\frac{\partial T_0}{\partial z}\right) = \frac{\partial^2 T_0}{\partial r^2} + \frac{1}{r}\frac{\partial T_0}{\partial r} + \frac{\partial^2 T_0}{\partial z^2}, \tag{3-12}$$

with boundary conditions

$$\psi = 0, \qquad \frac{\partial^2 \psi}{\partial r^2} - \frac{\partial \psi}{\partial r} = \mathrm{Re}_{\mathrm{FZ}}\frac{\partial T_0}{\partial z}F(z), \qquad \frac{\partial T_0}{\partial r} = 1 - \left(\frac{z}{b}\right)^2, \qquad \text{at} \qquad r = 1, \tag{3-13}$$

$$\frac{\partial \psi}{\partial z} = 0, \qquad \psi = 0, \qquad T_0 = 0, \qquad \text{at} \qquad z = b. \tag{3-14}$$

The base flow variables are represented with Chebyshev polynomials:

$$\psi\left(r, \frac{z}{b}\right) = r^2 \sum_{L=0}^{N_{RF}+1} \sum_{M=0}^{N_{ZF}+1} A_{LM} T_{2L}(r) T_{2M+1}\left(\frac{z}{b}\right), \tag{3-15}$$

$$\omega_\theta\left(r, \frac{z}{b}\right) = r \sum_{L=0}^{N_{RF}} \sum_{M=0}^{N_{ZF}} B_{LM} T_{2L}(r) T_{2M+1}\left(\frac{z}{b}\right), \tag{3-16}$$

$$T_0\left(r, \frac{z}{b}\right) = \sum_{L=0}^{N_{RT}} \sum_{M=0}^{N_{ZT}} C_{LM} T_{2L}(r) T_{2M}\left(\frac{z}{b}\right), \tag{3-17}$$

where $Tn® = \cos(n \arccos r)$ are the Chebyshev basis functions. As a result of radial symmetry (axisym metry), only even Chebyshev terms are utilized in r, with the overall radial symmetry set by the multiple of r in front of the representation. This corresponds to the behaviors as $r \to 0$, which were investigated for ψ, $\omega\theta$, and T using the Frobenius method. Moreover, due to the axial symmetry, only even or odd Chebyshev terms are nonzero in z. Taking advantage of axisymmetry and the axial symmetry, the unique computational domain for the base flow is reduced to $r \in (0, 1)$, $z \in (0, b)$ at $\theta = 0$ and is discretized using Gauss–Lobatto collocation grids ($NRF \times NZ\,F$ for the flow field and $NRT \times NZ\,T$ for the temperature field) given, for example, by

$$r_{IF} = \cos\frac{I_F \pi}{2N_{RF}} \qquad \text{for} \qquad I_F = 0, 1, 2, \ldots, N_{RF}, \tag{3-18}$$

$$z_{KF} = \cos\frac{K_F \pi}{2N_{ZF}} \qquad \text{for} \qquad K_F = 0, 1, 2, \ldots, N_{ZF}. \tag{3-19}$$

These grids weight the finest resolution toward the free surface and the solid boundary where it is most needed.

At r = 0 or z = 0, the governing equations (3-10) and (3-11) and the first two boundary conditions in (3-

13) (at $z = 0$) reduce to 0 = 0. To impose constraints at $r = 0$ and $z = 0$, the first nonzero leading order of these equations are applied. For example, after substituting the representations for ψ and $\omega\theta$ from (3-15) and (3-16), respectively, (3-10) becomes

$$\sum_{L=0}^{N_{RF}}\sum_{M=0}^{N_{ZF}} B_{LM} r T_{2L} T_{2M+1} - \sum_{L=0}^{N_{RF}+1}\sum_{M=0}^{N_{ZF}+1} A_{LM}\frac{r}{b^2} T_{2L} T''_{2M+1} - \sum_{L=0}^{N_{RF}+1}\sum_{M=0}^{N_{ZF}+1} A_{LM}(r T''_{2L} + 3T'_{2L}) T_{2M+1} = 0. \quad (3\text{-}20)$$

Equation (3-20) simplifies to $0 = 0$ at $r = 0$. Instead, if the Chebyshev basis functions are expanded in their Taylor series

$$T_{2L}(r) = (-1)^L\left[1 - 2L^2 r^2 + \tfrac{2}{3}L^2(L^2-1)r^4 + O(r^6)\right], \quad (3\text{-}21)$$

the coefficients of the nonzero leading order (r^1) can be used as a constraint at $r = 0$:

$$\sum_{L=0}^{N_{RF}}\sum_{M=0}^{N_{ZF}} B_{LM} r'(-1)^L T_{2M+1} - \sum_{L=0}^{N_{RF}+1}\sum_{M=0}^{N_{ZF}+1} A_{LM}\frac{r'}{b^2}(-1)^L T''_{2M+1} - \sum_{L=0}^{N_{RF}+1}\sum_{M=0}^{N_{ZF}+1} A_{LM}[r'(-1)^L(-4L^2) + 3(-1)^L(-4L^2 r')] T_{2M+1} = 0. \quad (3\text{-}22)$$

It was found that the constraints above at r = 0 and z = 0 enhance the accuracy of the solution greatly with minimal additional computational cost. Therefore these constraints were applied in all cases presented here. At the top boundary z = b, boundary conditions were applied using orthogonality, hence special treatment was not required at (r,z) = (0, b)

The ReFZ is ramped up starting from ReFZ < 1, where the flow field is almost stagnant, until the desired value is obtained. Solutions for lower ReFZ cases become initial guesses for larger ReFZ cases.

The governing equations and boundary conditions are solved using the Newton–Raphson iterative method.LU decomposition and back substitution is performed using the DGESV routine [Intel 2008] in LAPACK [Anderson et al. 1999]. The base flow code is written in Fortran 90.

3C. Magnetic damping. When exposed to an axial static magnetic field, radial and azimuthal flow mo tions are damped by the electromagnetic body force. Figure 3 demonstrates this magnetic damping effect by varying the Hartmann number Ha while keeping the material properties (Pr) and the heat input (ReFZ) fixed.

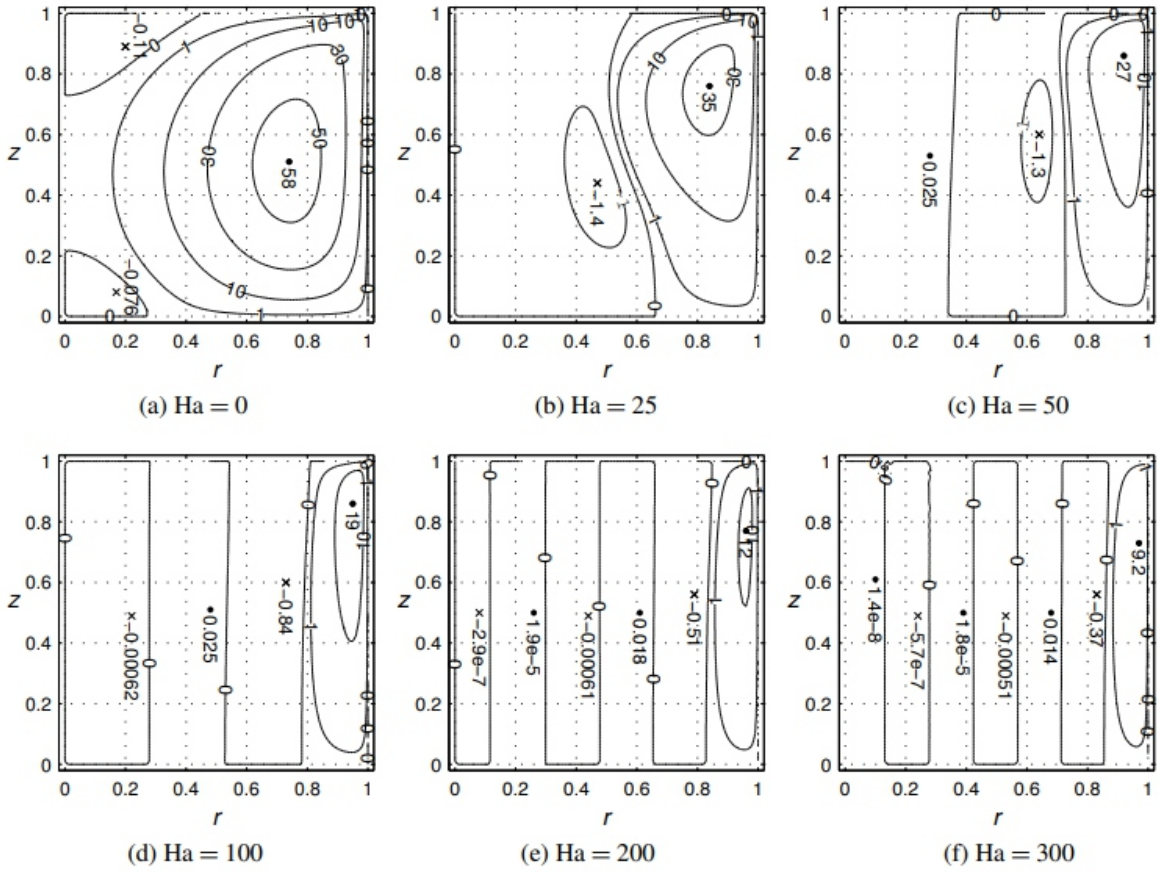

Figure 3. Magnetic damping effect on the stream function contours (Pr = 0.02, ReFZ =21,914.8).

Without magnetic damping (Ha = 0), a primary circulation "cell" forms due to the thermocapillary effect. Flow circulates counterclockwise throughout $r \in (0, 1)$ in the upper half of the liquid bridge. Small secondary recirculation cells also emerge in the interior due to strong convection. At Ha = 25, the electromagnetic effect weakens the primary circulation cell and confines it within $r \in (0.5, 1)$. When exposed to a magnetic field in the +z direction, radial inflow (in the −r direction) near the (r,z) = (1, 1) corner induces electric current in the +θ direction (into the page). This electric current leads to the Lorentz force exerted in the +r direction, which opposes the inflow moving in the −r direction. By continuity, the flow is turned downward and then circulates back as a loop.

As the magnetic field further intensifies, the primary circulation cell is confined more dramatically near the free surface, and more circulation cells develop in the interior. The most significant flow is always within the primary circulation cell. Extremum stream function values within each cell show that the interior of the liquid bridge is effectively stagnant, which is ideal for crystal growth from a melt.

Note that in this example ReFZ is chosen at 21,914.8, which is near the critical value for Pr = 0.02 at Ha = 50. This ReFZ value is well above the critical instability values for Ha = 0 and Ha = 25; therefore the actual flow would be perturbed from the base flow states shown here.

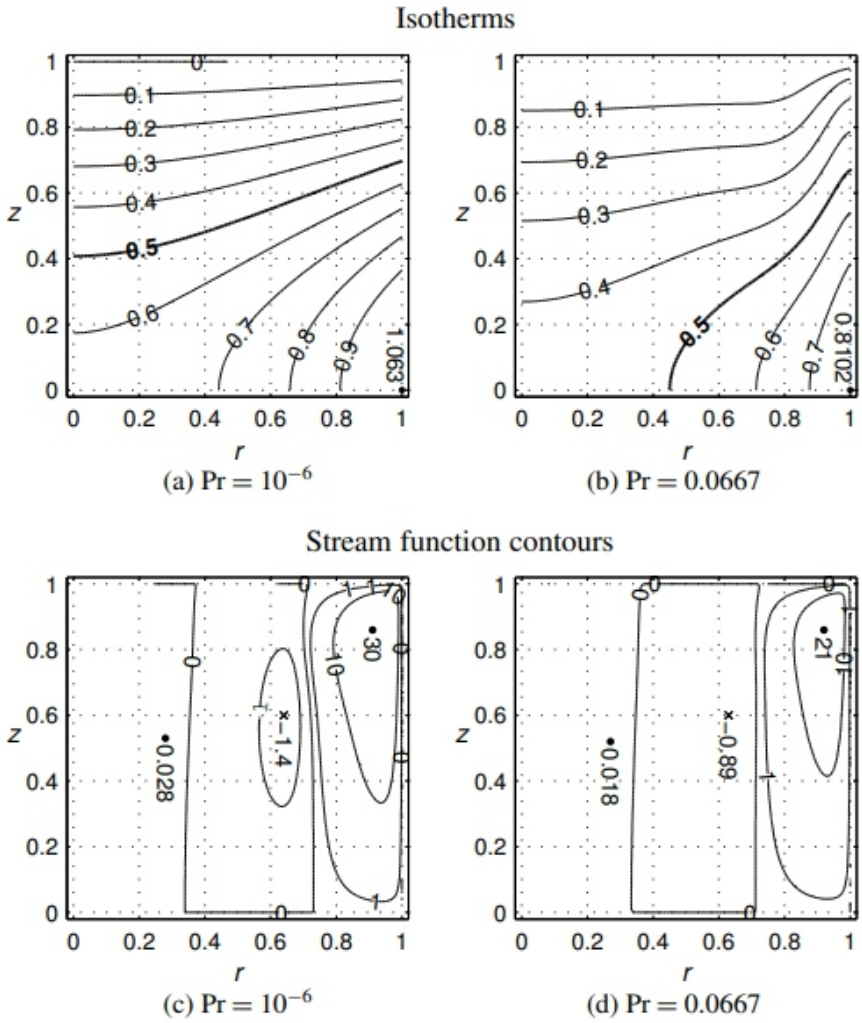

Figure 4. Prandtl number effect on the temperature field and the flow field (Ha = 50, ReFZ =21,914.8).

3D. Prandtl number effect. The crystal growth community has frequently studied the effect of Prandtl number Pr, representing different physical materials, in various liquid bridges, typically without magnetic stabilization. For example, Kasperski et al. [2000] first investigated the different characteristics of low and high-Pr full-zone instabilities. Levenstam et al. [2001] performed a fairly continuous Pr study using the half-zone with a focus on the intermediate Pr range which bridges the gap between the low and high-Pr regimes. Bouizi et al. [2007] presented full-zone instabilities over a wide range of Pr ∈ (0.001, 100) by three-dimensional nonlinear spectral computations.

For a liquid bridge with small Pr, conduction is dominant over convective heat transfer. In the limit of Pr → 0, the temperature field is decoupled from the flow field. For example, the isotherms for Pr = 10−6 (Figure 4a) indicate pure conduction. In this case Tmax = 1.0633 remains constant as the magnetic field varied over Ha ∈ (0, 300) (not shown). Tmax is always located at (r,z) = (1, 0), the location of maximum heat flux.

As Pr increases, Tmax is reduced due to convective heat transfer (at a fixed Ha) assisting conduction in distributing the thermal energy throughout the domain. At Pr = 0.0667, isotherms are bent by convection (Figure 4b). Notice that the T = 0.5 curve shifts by a large amount compared to the case of Pr = 10−6.

Compared to the temperature distribution, the Prandtl number has a less significant impact on the flow field with magnetic stabilization. In moving from Pr = 10−6 to Pr = 0.0667, the flow is weakened (see Figures 4c and 4d) due to the weaker thermocapillary driving force resulting from the smaller temperature gradient at the free surface. Otherwise, the cell thicknesses and locations of local extrema change little, primarily because the electromagnetic damping, proportional to the radial flow velocity, increases as the flow intensifies.

The primary flow instabilities for small-Pr liquid bridges with magnetic stabilization are hydrodynamic in nature. The first instability for Pr < 0.4 is characterized by stationary disturbances [Bouizi et al. 2007]. Within this range, [Houchens and Walker 2005] further suggested three subregimes with different axial symmetries of the perturbations, which were confirmed in [Bouizi et al. 2007], both in full-zone geometries. In [Levenstam and Amberg 1995; Leypoldt et al. 2000] the secondary instability was found to be three-dimensional and oscillatory in the half-zone.

For high-Pr liquid bridges, convective heat transfer is dominant over conduction and the instability mechanism is hydrothermal. The base flow first transitions to oscillatory perturbations (see [Leypoldt et al. 2000], for example). Due to strong thermal convection at high Pr, isotherms are dramatically distorted such that a large temperature gradient exists at the free surface near the top and bottom bound aries. In reality, the melt-solid interfaces may deform significantly from the assumed rigid plane due to this strong thermal convection. To accurately resolve high-Pr liquid bridges, more realistic boundary conditions are needed, hence this work is limited to low-Pr cases.

For a fixed Pr > 0 (with ReFZ fixed as in Figure 5), increasing Ha continuously confines the flow into a narrower region near the free surface and reduces the effectiveness of convective heat transfer into the interior. Thus Tmax increases, which enhances the thermocapillary driving effect. Therefore the flow

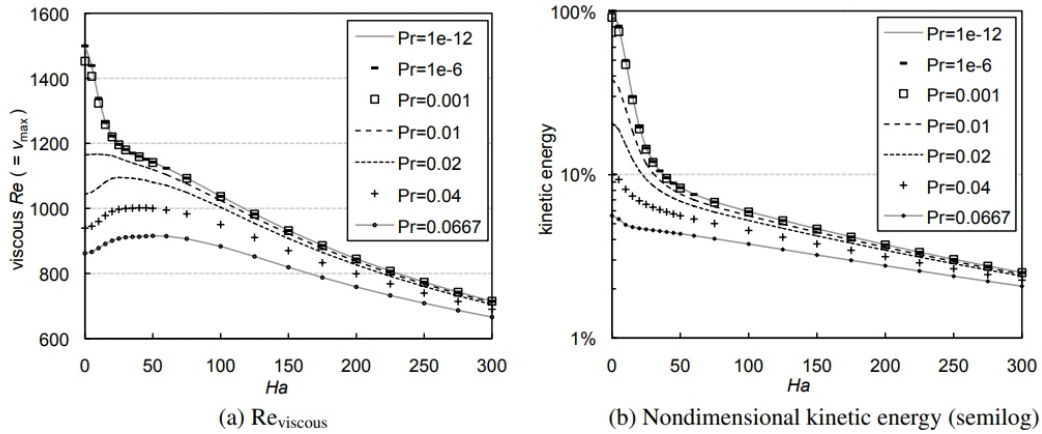

(a) $Re_{viscous}$ (b) Nondimensional kinetic energy (semilog)

Figure 5. Effects of Prandtl number and magnetic damping on viscous Reynolds number and

nondimensional kinetic energy (ReFZ =21,914.8 fixed in all cases).

velocity increases at the free surface, but this is limited to a narrow cell due to magnetic damping. Reviscous also increases proportionally to the maximum nondimensional velocity vmax which always occurs near (r,z) = (1, b). This explains the initial increase of Reviscous with Ha for Pr ≥ 0.02 in Figure 5a. Eventually magnetic damping is sufficiently large that vmax is reduced, even though Tmax continues to increase and approach 1.0633 (the value in the limit of no convective heat transfer). Also observe that Reviscous decreases monotonically with increasing Ha for Pr ≤ 0.001. For Pr ≤ 0.001 the temperature field is effectively decoupled from the flow field and Tmax remains constant as Ha increases. Therefore increasing Ha does not enhance the thermocapillary effect. Pr = 0.01 marks the division between these two trends.

The nondimensional kinetic energy, computed as the integral of velocity squared over the domain, drops quickly as Ha increases (see Figure 5b), which demonstrates the magnetic damping effect. For a fixed ReFZ (q*R*/k*, the fact that kinetic energy also drops as Pr (= μ*c*p /k*) increases can explained as follows. Assume that the dynamic viscosity μ* , specific heat c*p , and radius R* remain unchanged. Increasing Pr then corresponds to decreasing the thermal conductivity k* and consequently a reduction in maximum heat flux q* (to maintain a constant ReFZ). Therefore with less thermocapillary driving force, kinetic energy within the melt is reduced as Pr increases. Also note that the Pr = 0.001, Pr = 10−6 and Pr = 10−12 curves are virtually indistinguishable, which indicates that Pr = 0.001 is a good approximation for the limit of Pr → 0, at least over the range 0 ≤ Ha ≤ 300.

4. Normal-mode linear stability analysis

4A. Disturbances. Normal-mode linear stability analysis, which compares well with nonlinear simula tions in the half-zone [Levenstam et al. 2001], was used to study the stability of the base flow in the full-zone liquid bridge. The base flow was subjected to infinitesimal three-dimensional normal-mode disturbances of the form

$$\xi(r,\theta,z,t) = \xi_0(r,z) + \varepsilon\,\mathrm{Real}\{\exp(\lambda t + i\,m\theta)\xi_1(r,z)\} \qquad \text{for } \xi = v_r,\, v_z,\, P,\, T,\, j_\theta, \qquad (4\text{-}1)$$

$$\zeta(r,\theta,z,t) = \varepsilon\,\mathrm{Real}\{\exp(\lambda t + i\,m\theta) i\zeta_1(r,z)\} \qquad \text{for } \zeta = v_\theta,\, \phi,\, j_r,\, j_z, \qquad (4\text{-}2)$$

where ε is an infinitesimal magnitude and m denotes the azimuthal wave number of the disturbance. For uniqueness, disturbance waves must complete themselves as they travel through θ = 0 → 2π, therefore m is integer valued. Axisymmetric m = 0 cases were not investigated as they have been shown to be very stable in similar systems [Kasperski et al. 2000]. The extra factor of i in (4-2) accounts for the phase shift in the variables which are zero in the base state, yielding a purely real linear stability problem.

Disturbances adhere to one of two axial symmetries. When perturbation variables have the same axial symmetry as their corresponding base flow variables, the mode is denoted as “symmetric”. When perturbation variables have the opposite axial symmetry as their corresponding base flow variables, the

mode is denoted as “antisymmetric”. Any combination of these disturbance types will result in a critical ReFZ that larger than the smaller ReFZ,cr of these two.

Figure 6 shows an example of streamlines in the base flow along with the disturbed flow. In the ax isymmetric base flow state, a weightless fluid particle released at the starting point circulates on the black closed path (the stream function contour) within a fixed θ plane. This specific example first transitions to stationary antisymmetric disturbances with m = 2. At the critical ReFZ, a particle released at the same starting point changes its “orbiting radius” as it circulates, while oscillating within a θ = π/m wedge.

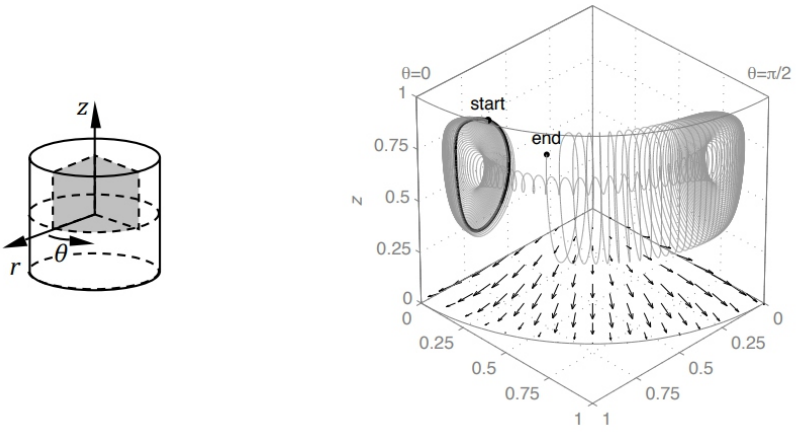

Figure 6. Streamlines in the base flow (black closed path) and disturbed flow (gray spiral path), and disturbed flow (vectors) at the midplane (Pr = 0.02, Ha = 0 at ReFZ,cr = 1546.58, stationary antisymmetric disturbances with m =2, base flow grid r ×z =35×45, temperature grid r×z =30×30, linear stability grid r×z =28×28, α =300, perturbation versus base flow maximum magnitude ratio 5%).

Note that the path is cut off intentionally at the “end” point to better show its spiral structure. Flow in other wedges and in the lower half of the liquid bridge can be inferred from the symmetry and mode number of the disturbance.

Arrows in the z = 0 plane of Figure 6 show the disturbed flow motion at the liquid bridge midplane. Flow circulates from the liquid bridge interior back to the free surface due to the viscous effect. The flow at z = 0 has no azimuthal component due to the antisymmetric disturbance mode. Perturbed flow crosses the midplane into the upper or lower half of the liquid bridge. In contrast, the half-zone assumes a no-slip, no-penetration midplane.

4B. Critical thermocapillary Reynolds number. The critical ReFZ,cr measures the critical point at which the base flow transitions to the first instability. Beyond ReFZ,cr, one or more infinitesimal disturbances grow in time, breaking either the axisymmetry or the axial symmetry or both, and

potentially evolving the motion to a periodic flow. The goal is to find the first transition to instability among all possible disturbance modes.

By substituting the disturbance variables of (4-1) and (4-2) into the governing equations and boundary conditions and linearizing (neglecting ε 2 terms) and discretizing, a generalized eigenvalue problem is obtained:

$$\underline{\underline{AM}}\,\underline{x} = \lambda\,\underline{\underline{BM}}\,\underline{x}, \tag{4-3}$$

The entire generalized system was solved using either the routine RGG in EISPACK or the routine DGGEV in LAPACK [Anderson et al. 1999], with refinement of the critical eigenvectors performed via the inverse iteration method [Saad 1992]. The real part of the leading eigenvalue (or pair) λR determines the stability of this system. If the imaginary part of the leading eigenvalue pair λI 6= 0, the base flow tran sitions to a periodic disturbance. Otherwise λI = 0 and the transition is stationary. For each disturbanc mode (Pr, Ha, m, antisymmetric or symmetric mode), a neutrally stable mode is found if the leading eigenvalue (or pair) has λR = 0. A slight increase in ReFZ causes this mode to become unstable and grow in time.

Finding the ReFZ associated with a neutrally stable mode is an iterative process. Starting from a stable ReFZ,s (with λR < 0) and an unstable ReFZ,u (with λR > 0), a better approximation ReFZ,3 is predicted using the regula falsi method. The new λR corresponding to ReFZ,3 is computed using the shifted inverse iteration method. The ReFZ,3 then replaces either ReFZ,s or ReFZ,u. In this way the bounds on the neutrally stable ReFZ are narrowed through iterations until convergence. The linear stability analysis code is written in Fortran 90.

Variables in the linear stability analysis are the velocity perturbations vr1 and vz1, temperature per turbation T1, and electric potential perturbation φ1. Reduction from the 9 primitive stability variables to these four is accomplished using incompressible continuity and θ momentum to solve for vθ1 and P1, respectively. The electric current density perturbations (jr1, jθ1, and jz1) are solved using Ohm's law and then substituted into conservation of charge. The resulting set of partial differential equations can be found in [Houchens and Walker 2001] for the half-zone. Similarly to the base flow analysis, these variables are represented as Chebyshev polynomials. Only even or odd terms in both r and z are nonzero due to the symmetries. In addition, by modeling antisymmetric and symmetric disturbance modes separately, the full-zone liquid bridge domain can be halved at the midplane. The price is that two codes have to be developed. An NR × NZ Gauss–Lobatto collocation grid is adopted for r ∈ (0, 1) and z ∈ (0, b), which is equivalent to a grid resolution of r × z = (2 × NR) × (4 × NZ) in the fulldomain liquid bridge simulation if no symmetries are observed. The finest stability analysis grid used was NR × NZ = 50 × 70 for high-Ha cases.

Disturbances with a wide range of azimuthal wave numbers m, for both the antisymmetric and sym

metric modes, are investigated. Axisymmetric disturbances (m = 0) are not studied in this work because they are unlikely to be the critical disturbance mode. For example [Bouizi et al. 2007] reported that ReFZ,cr for the m = 0 mode ranges from seven times to thousands of times larger than ReFZ,cr for the critical m = 2 mode for Pr ∈ (0.001, 0.04).

For a fixed Pr, a neutrally stable ReFZ versus Ha branch can be obtained for each disturbance mode.

The critical ReFZ,cr is the lowest among all neutrally stable ReFZ's. For example, the neutral stability branches for Pr = 0.02 (Figure 7a) show how the critical disturbance mode changes from m = 2 to 3 and then 4 for Ha ∈ (0, 50). The m = 2 symmetric branch (dashed line) deviates from the critical antisymmetric modes as Ha increases. Although other stability branches above the critical branch are not valid for predicting a second and third bifurcation, they provide insight into flow stability when subject to these perturbation modes.

Table 1 lists ReFZ values on the Pr = 0.02 neutral stability branches. For both antisymmetric and symmetric disturbance modes, m is tracked from 1 to 8 for Pr = 0.02, and to at least the critical m + 4 for Pr = 0.001. ReFZ values not shown in Table 1 are higher than these listed ReFZ's for the same Ha. The m = 5 antisymmetric branch never becomes critical up to Ha = 300 for Pr = 0.02.

The ReFZ,cr versus Ha curves for Pr = 0.02 and Pr = 0.001 (see Figure 7b) summarize the first instabilities over a wide Ha range. The ReFZ,cr increases quickly with increasing Ha, which demonstrates the magnetic stabilization effect. Stronger magnetic fields damp the flow, so that more driving energy must be fed in before the flow trips to an instability. The critical curves determine the minimum magnetic

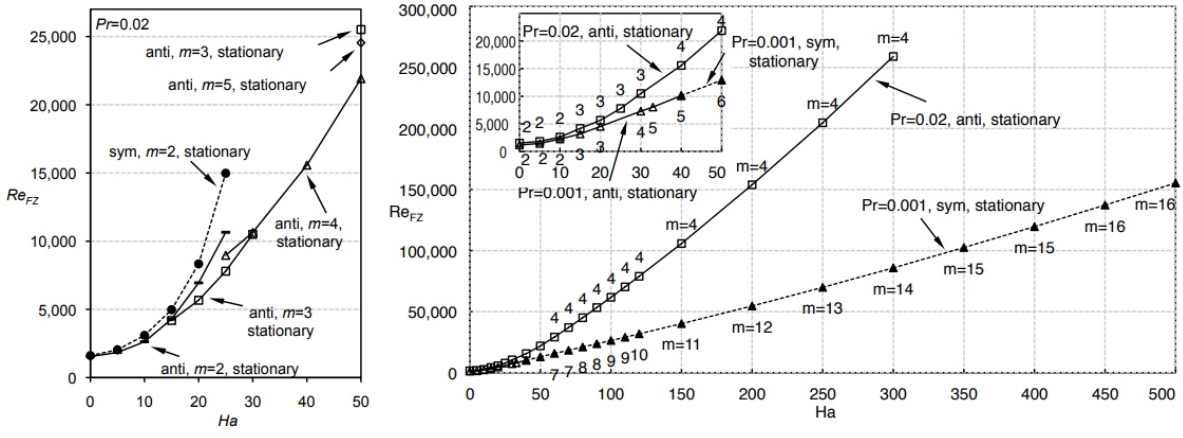

(a) Neutral stability branches

(b) First instability $Re_{FZ,cr}$ versus Ha curves

Figure 7. Example of neutral stability branches for Pr = 0.02 and the first instability critical curves for Pr = 0.02 and for Pr = 0.001.

Ha	Antisymmetric $m=2$	$m=3$	$m=4$	$m=5$	Symmetric $m=2$
0	1,546.58				1,618.42
5	1,842.97				2,041.81
10	2,629.52				3,098.39
15	4,291.10	4,187.74			4,978.35
20	6,946.57	5,671.88			8,337.20
25	10,653.30	7,800.11	8,964.73		14,980.91
30		10,501.11	10,642.13		
40			15,575.20		
50		25,513.47	21,914.83	24,545.29	
60			29,168.06	30,544.57	
70			36,961.68	37,672.75	
80			44,999.40	45,250.00	
90			53,316.88	53,583.48	
100			61,747.38	62,263.88	
110			70,289.58	71,229.01	
120			79,037.36	80,562.15	
150			105,776.82	109,765.83	
200		162,032.06	153,945.51		
250			204,740.95	225,107.28	
300		263,317.80	259,068.47	293,492.96	

Table 1. Neutrally stable ReFZ's for Pr = 0.02 branches (ReFZ,cr's are underlined).

field strength required to avoid instabilities in the optically heated float-zone crystal growth process. Note that Pr = 0.001 is chosen because its critical curve very likely marks the lower limit of critical curves for Pr → 0. According to [Houchens and Walker 2005], at Ha = 0 the ReFZ,cr for Pr = 10−10 is less than 1% smaller than ReFZ,cr for Pr = 0.001. Details of the perturbation flow field and the energy analysis between the base state and perturbed field are presented and validated with other liquid bridge studies in [Huang and Houchens 2011]. Here the focus is instead on the numerical issues that arise in the spectral collocation technique and linear stability analyses. The following sections are widely applicable to a range of partial differential equations. First, identification of spurious eigenvalues is discussed. Then, regularization and grid dependence issues are covered. Finally, the use of pseudospectra to investigate the robustness of stability analyses are addressed.

4C. Identifying spurious eigenvalues. In the linear stability analysis, unstable systems are identified by positive leading eigenvalues. However, some spurious eigenvalues (usually with very large magnitudes) emerge in the generalized eigenvalue problem, (4-3), bearing no physical meaning regarding system stability. It is crucial to identify and separate them from the remaining legitimate eigenvalues to correctly predict the stability of the system.

Legitimate eigenvalues are independent of linear stability grid resolution. In Table 2, to test if the

leading eigenvalue pair 350.47 ± 7542.09i on a 30 × 40 grid is legitimate or spurious, the linear stability code was run on two other grid sizes, 28×28 and 40×50. The fact that 350.47±7542.09i is not present on these two grids indicates that it is a spurious eigenmode. All other leading eigenvalues agree well, independent of the grid.

As a direct proof, perturbation variable contours are plotted (Figure 8a) using eigenvectors corre sponding to the spurious eigenvalue pair 350.47 ± 7542.09i. The checkerboard pattern has no physical justification, but is rather an oscillation of a high-order mode(s) in each direction between Gauss–Lobatto collocation points. This is clearly shown in the Chebyshev polynomial coefficient plot (Figure 8b) for vr1, where

$$v_{r1}\left(r, \frac{z}{b}\right) = r^{m-1} \sum_{L=0}^{N_R+1} \sum_{M=0}^{N_Z} \mathcal{A}_{LM} T_{2L}(r) T_{2M}\left(\frac{z}{b}\right). \tag{4-4}$$

Grid size	$r \times z = 28 \times 28$	$r \times z = 30 \times 40$	$r \times z = 40 \times 50$
Leading eigenvalues		$\underline{350.47 \pm 7542.09i}$	
	$-34.61 \pm 9.25i$	$-34.61 \pm 9.26i$	$-34.61 \pm 9.25i$
	$-94.58 \pm 110.75i$	$-94.58 \pm 110.75i$	$-94.58 \pm 110.75i$
	$-113.45 \pm 56.60i$	$-113.46 \pm 56.59i$	$-113.46 \pm 56.60i$
	$-129.35 \pm 175.31i$	$-129.35 \pm 175.31i$	$-129.35 \pm 175.31i$
	$-140.05 \pm 72.15i$	$-140.04 \pm 72.15i$	$-140.04 \pm 72.15i$
	$-197.10 \pm 320.75i$	$-197.10 \pm 320.75i$	$-197.10 \pm 320.75i$
	⋮	⋮	⋮

Table 2. Identification of a spurious eigenvalue (underlined) through grid refinement of the linear stability analysis (Pr=0.001, Ha=0, ReFZ =1000, m =1, α =400, symmetric mode).

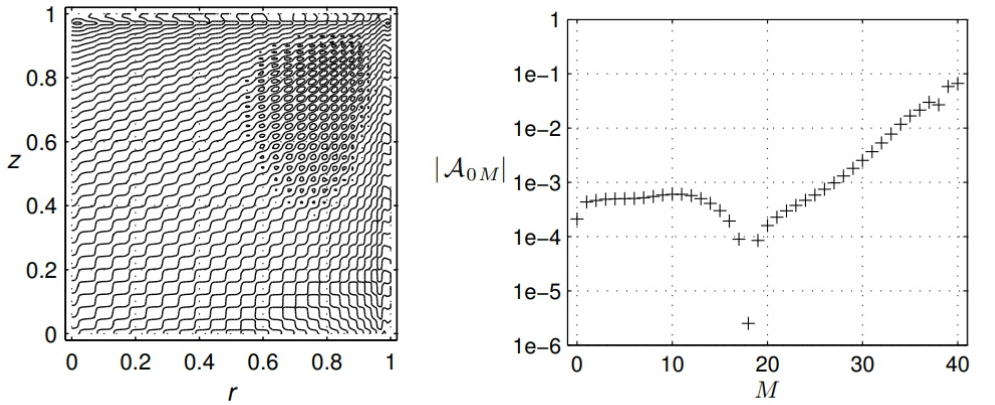

(a) v_{r1} contours (b) Chebyshev polynomial coefficients for v_{r1}

Figure 8. Perturbation contours and Chebyshev polynomial coefficients associated with the spurious eigenmode 350.47±7542.09i in Table 2 (Pr = 0.001, Ha = 0, ReFZ = 1000, m = 1, α = 400, linear stability grid r × z = 30 × 40).

The coefficients of the highest-order Chebyshev terms have the largest magnitudes, which are responsi ble for the high-frequency, oscillating contours. Note that for a legitimate eigenmode, the Chebyshev polynomial coefficients decay exponentially when the representation is sufficient. Therefore, for this case the legitimate leading eigenvalue is a complex pair with negative real part −34.61 ± 9.26i as shown in Table 2. The base flow is stable at ReFZ = 1000 for this branch (Pr = 0.001, Ha = 0, and m = 1 symmetric disturbance mode).

5. Numerical aspects

5A. Regularization of the vorticity singularity. A regularization function F(z) (from (3-7)) is introduced in the thermocapillary boundary condition to remove the singularity of the velocity gradient at the corner (r,z) = (1, b). While $\partial vz0/\partial r = 0$ at (r,z) = (1, b) due to the boundary condition vz0 = 0 at z = b, the thermocapillary boundary condition, without regularization, gives a nonzero $\partial vz0/\partial r$ at (r,z) = (1, b) due to the nonzero temperature gradient $\partial T0/\partial z$ at the free surface. This singularity is removed by multiplying the thermocapillary boundary condition by a function that decays quickly to 0 as $z \rightarrow b$ but remains equal or close to 1 for the rest of z.

An optimum value of the regularization parameter α is achieved when increasing α further has no measurable impact on the flow and the singularity is effectively removed. Figure 9 shows a test over a wide range of α. With a sufficiently large value the physics becomes independent of α, as indicated by the "desired range". But too large an α may provide insufficient regularization. In Figure 9, the vr0 contours bear wiggles and circles, indicating α =50,000 is too large for this case. With even less smoothing (higher α), the vorticity singularity may cause the numerical solver to predict the wrong physics, suggested by the sudden drop of the critical ReFZ beyond α =100,000. On the other hand, if the value of α is too small, the regularization effectively reduces the heat input at the free surface which reduces the driving force and explains the increase of the critical ReFZ ("too much regularization") for α in range 10–100 in Figure 9.

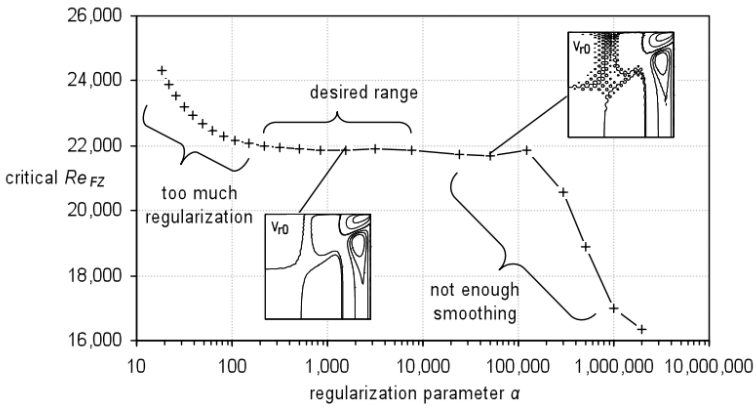

Figure 9. Searching for the desired range of regularization parameter α (semilog plot, Pr = 0.02, Ha = 50, flow grid r ×z = 40×40, temperature grid r ×z = 30×30, stability grid r × z = 40 × 40).

A fast-decaying regularization function is especially important for high-Pr liquid bridge simulation. Due to strong heat convection, the temperature at the free surface varies slowly along r = 1 until very close to (r,z) = (1, b). This feature is best preserved by a regularization function that decays quickly near (r,z) = (1, b). The choice of regularization function is arbitrary as long as the singularity is removed with minimum modification of the physics. For example, in [Bouizi et al. 2007] a power function regularization function F(z) = (1 − z 2n)2 was adopted, where n is a regularization parameter.

5B. Grid resolution and independence. A solution which does not vary with significant further grid refinement indicates that the grid resolution is sufficient and the results are reliable. Table 3 shows such a test based on the critical ReFZ. Significant resolution increases are introduced for the base flow grids and the stability analysis grid, but the ReFZ,cr barely changes, demonstrating grid independence was achieved.

More subtle inferences can be made from this test. ReFZ,cr increased slightly on finer grids in Table 3. This is expected because a fixed regularization parameter (α = 400) affects more grid points on a finer axial grid than on a coarser axial grid. The thermocapillary effect is weakened at more collocation

the critical Re_{FZ} for		stability grid ($r \times z$) 34×60	stability grid ($r \times z$) 50×70	% difference
flow grid, temperature grid	30×75, 25×25	61,775.37	61,840.74	**0.11%**
($r \times z$)	70×100, 40×40	61,789.51	61,841.79	**0.08%**
% difference		**0.02%**	**0.002%**	

Table 3. Grid dependence study based on ReFZ,cr for Pr = 0.02, Ha = 100, α = 400.

points on finer grids, therefore a higher ReFZ,cr is expected. However if this regularization effect were eliminated, ReFZ,cr would be lower on finer grids, because coarser grids tend to smear out the largest gradients, which contribute energy to the instability mechanism. On coarser grids, ReFZ,cr increases to compensate for this smearing effect until the energy is sufficient to trip the instability. Thus, in practice, it is necessary to carry out both grid and regularization dependence studies simultaneously. The regularization parameter must be increased as the grid is refined.

5C. Model robustness investigated by pseudospectra. As discussed above, the flow stability in the liquid bridge is determined by its eigenvalues. For the generalized eigenvalue problem, (4-3), each eigenvalue (each black dot in Figure 10) is associated with one flow perturbation eigenmode. Purely real eigenvalues correspond to perturbations in which the base flow transitions to steady, three-dimensional (not axisymmetric) perturbed flow. Complex eigenvalue pairs correspond to perturbations in which the base flow transitions to three-dimensional time-dependent flow, with the imaginary components repre senting the frequency.

Compared to the simplified numerical full-zone model, real world experiments include many imper

fections that are difficult to represent. For example, in experiments the heat flux will not be strictly parabolic or axisymmetric and the free surface will not be exactly cylindrical. It is therefore desirable to predict what impact these imperfections might have, to verify the robustness of the model as compared to the experiment it is intended to represent.

Furthermore, numerical errors in the model may also play a significant but unpredictable role. For example, round-off errors in the eigenvalue problem may accumulate during computation and affect the results. Simulation results are more meaningful provided they are valid even when the model is subject

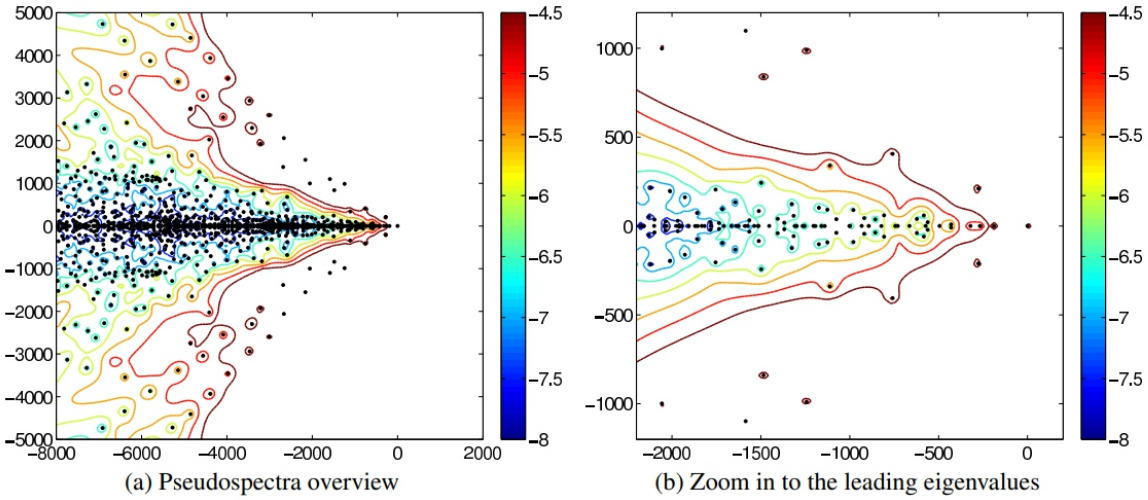

Figure 10. Eigenvalues (black dots) and their pseudospectra σ (contours) of the generalized eigenvalue problem (4-3) (Pr = 0.02, Ha = 50, ReFZ =21,879.5, flow grid r × z = 70 × 100, temperature grid r × z = 40 × 40, stability grid r × z = 35 × 50, α = 1000).

to these minor changes, whether these are purely numerical or result from the inability of the model to represent small imperfections in the experiment.

Pseudospectral analysis provides a quantitative measure to test model robustness. Small numerical errors are purposefully introduced into either or both **AM** and **BM** matrices in the eigenvalue problem **AM** x = λ **BM** x (see (4-3)). Note that is different from the ε used in the linear stability analysis. In fact, acts like a random perturbation on ε. The small errors introduced through can represent physical perturbations on the boundary conditions, geometry, and flow field of the model. They can also be purelynumerical perturbations. In this problem such perturbations could be relatively minor (introducing slight curvature in the free surface) or more egregious (violations of conservation of charge).

After introducing these scale errors, the modified generalized eigenvalue problem is solved again to investigate any physically meaningful changes. For example, a possible scenario of significant interest would result if a previously more-stable branch became the critical mode in the modified system. This has tremendous relevance in this problem, as only one known experimental study in a low-Pr fluid in the

half-zone configuration has indicated possible observation of the steady, three-dimensional transition before onset of periodicity [Takagia et al. 2001]. In other experiments, the instability has appeared to jump directly to the higher branch associated with the periodic transition, suggesting that the distinction between the preferred modes may be very subtle. Results will show, fortunately or unfortunately, that such sensitivity is not found in the full-zone model.

Introduced in [Reddy and Trefethen 1990], pseudospectra present a systematic method for carrying out such analyses. For an introduction and a simulation method (EigTool) for problems of small or moderate size, the reader is referred to [Embree and Trefethen 2011]. An extensive discussion on pseudospectra, including fluid mechanics applications, can be found in [Trefethen and Embree 2005].

For the large generalized eigenvalue problem in this work the matrix **AM** is perturbed with the random matrix **E** in the way described in [van Dorsselaer 1997] using

$$\begin{aligned}\sigma_\epsilon(\underline{\underline{\boldsymbol{AM}}}, \underline{\underline{\boldsymbol{BM}}}) &= \{z \in \boldsymbol{C} : \|(z\,\underline{\underline{\boldsymbol{BM}}} - \underline{\underline{\boldsymbol{AM}}})^{-1}\| > 1/\epsilon\} \\ &= \{z \text{ is an eigenvalue of } (\underline{\underline{\boldsymbol{AM}}} + \underline{\underline{\boldsymbol{E}}}, \underline{\underline{\boldsymbol{BM}}}) \text{ for some } \underline{\underline{\boldsymbol{E}}} \text{ with } \|\underline{\underline{\boldsymbol{E}}}\| < \epsilon\}.\end{aligned} \tag{5-1}$$

This analysis must be repeated until representative pseudospectra are obtained. Resulting pseudospectra σ contours indicate the sensitivity of the original eigenvalues to the random noise introduced via .

The results of this analysis are given by the color contours in Figure 10. The color gradient indicates the magnitude of the perturbation. The smallest = 10−8 perturbations do not affect the leading eigenvalues at a measurable level, hence the blue contours are not visible around these eigenvalues in the complex plane. The first blue envelope that can be observed at this order occurs for eigenvalues with real parts near −1500. As the order of increases, more eigenvalues are influenced. For example, a perturbation of size = 10−5 may move enclosed eigenvalues anywhere within the medium-red regions in Figure 10.

The leading real eigenvalue and complex eigenvalue pair are the most likely to become critical. The linear stability analysis predicts that the real eigenvalue will dominate. This is confirmed by the pseu dospectra in Figure 10. Namely, at the largest pseudospectral perturbation of = 10−4.5 , the leading real eigenvalue maintains its leading position and explores only a very small region near its origin. In fact, no dark red contours of any eigenvalue extend into the positive half of the real plane. Since the pseudospectra contours of all the eigenvalues remain behind the leading eigenvalue, the branches associated with these modes will not become critical, even in the modified system. Therefore the critical eigenmode (stationary, antisymmetric disturbances with m = 4 in this example) predicted by the original generalized eigenvalue problem remains valid under such perturbations. Therefore, in careful experiments it would be expected that the stationary mode would be observed first.

To quantitatively or qualitatively relate = 10−4.5 numerical perturbations to specific physical changes in the fluid model is appealing, but intractable without imposing further structure on the perturbation. Random changes in matrix elements are often nonphysical, resulting in violations of the conservation of

mass, energy, and momentum, and breaking the orthogonality of boundary conditions. Thus even a small may have significant impacts on the physical system. In fact, the entire domain in Figure 10 is contained in the contour σ (**AM**,**BM**) for ≥ 10−4.35. Nevertheless, the pseudospectra suggests the results of the linear stability analysis are quite robust, particularly for the leading eigenvalues which are of most interest.

6. Conclusions

A thermocapillary-driven full-zone liquid bridge with magnetic stabilization is modeled numerically.

A wide range of three-dimensional flow disturbances are tracked using a normal-mode linear stability analysis. The first instability curve for Prandtl number Pr = 0.02 (for example, molten silicon) is obtained up to an intermediate Hartmann number of Ha ∈ (0, 300). Within this range, the steady axisymmetric base flow first transitions to stationary three-dimensional disturbances with axial symmetries opposite to their base flow components (the antisymmetric disturbance mode). Moreover, first instabilities for Pr = 0.001, representing the Pr → 0 limit, are presented up to Ha = 500. For Pr = 0.001, the base flow also first transitions to stationary three-dimensional disturbances. Axial critical disturbance symmetries are antisymmetric below Ha = 40 and symmetric for Ha ∈ (40, 500). The critical azimuthal wave number m increases with Ha for both Pr = 0.02 and Pr = 0.001.

Magnetic stabilization effects are observed and quantitatively measured for a steady external magnetic field in the axial direction. The induced Lorentz force acts proportionally against radial flow motion, thus multiple cell-like circulation patterns form within the liquid bridge. The most significant flow is confined to an increasingly narrow region near the free surface as Ha increases. At the interior the flow is damped until it is almost stagnant, which provides steady crystal growth conditions at the interface. This damping effect is also confirmed by quantitative studies of the viscous Reynolds number and kinetic energy versus Ha. Because the flow disturbances are greatly suppressed by magnetic stabilization, a more intense thermocapillary driving force is needed to trip instabilities within the liquid bridge. For example, the critical thermocapillary Reynolds number ReFZ,cr at Ha = 300 is two orders of magnitude larger than when no magnetic field (Ha = 0) is applied.

Small-Prandtl number liquid bridges, dominated by heat conduction, are studied over the range Pr ∈ (10−12 , 0.0667). For Pr ≤ 0.001, the temperature field is effectively decoupled from the flow field, mim icking a pure conduction state such that the temperature distribution is almost unchanged over the range Ha = 0 → 300. Thermal convection becomes important as Pr increases. It helps unify the temperature distribution throughout the domain as suggested by the isotherms. At higher Pr, the temperature gradient on the free surface concentrates near the liquid-solid boundaries (r,z) = (1, ±b), which intensifies the thermocapillary effect in these regions. Interestingly, the flow “circulation cell” thicknesses and locations are almost unaffected by increases in Pr over the range studied, mainly because the

electromagnetic force, proportional to the radial flow velocity, also increases as convection intensifies. Numerical techniques and analyses are also highlighted extensively in this work. For example, the vorticity singularity in the spectral scheme is removed by applying an exponential regularization func tion. The desired range of the regularization parameter α is determined by balancing the removal of the singularity and the invariance of the physics. The generalized eigenvalue problem $\underline{\mathbf{AM\ x}} = \lambda\ \underline{\mathbf{BM\ x}}$ in the linear stability analysis is investigated from a numerical perspective. Spurious eigenvalue modes with no physical meaning are identified by a combination of grid dependence studies and plotting of the eigenmodes. The pseudospectra indicate that results predicted by this full-zone model are valid even if the model is subject to minor changes, be they numerical or physical.

Acknowledgements. The authors would like to thank Professor Mark Embree at Rice University for providing the pseudospectra plots and insights on the eigenvalue problem and pseudospectra analysis. All tests were run on the Shared University Grid at Rice (SUG@R) cluster. This work was partially supported by the United States Air Force Office of Scientific Research.

References

[Anderson et al. 1999] E. Anderson, Z. Bai, C. Bischof, S. Blackford, J. Demmel, J. Dongarra, J. Du Croz, A. Greenbaum, S.Hammarling, A. McKenney, and D. Sorensen, "Linear Algebra PACKage", 1999, available at http://www.netlib.org/lapack/lug/index.html.

[Bouizi et al. 2007] O. Bouizi, C. Delcarte, and G. Kasperski, "Stability study of the floating zone with respect to the Prandtl number value", Phys. Fluids 19:11 (2007), 114102.

[Chen et al. 1997] G. Chen, A. Lizée, and B. Roux, "Bifurcation analysis of the thermocapillary convection in cylindrical liquid bridges", J. Cryst. Growth 180:3-4 (1997), 638–647.

[Cröll et al. 1994] A. Cröll, P. Dold, and K. W. Benz, "Segregation in Si floating-zone crystals grown under microgravity and in a magnetic field", J. Cryst. Growth 137:1-2 (1994), 95–101.

[Davis 1993] S. H. Davis, "Effects of flow on morphological stability", pp. 859–897 in Handbook of crystal growth, vol. 1B, edited by D. T. J. Hurle, Elsevier, New York, 1993.

[van Dorsselaer 1997] J. L. M. van Dorsselaer, "Pseudospectra for matrix pencils and stability of equilibria", BIT 37:4 (1997), 833–845.

[Embree and Trefethen 2011] M. Embree and L. N. Trefethen, "Pseudospectra gateway", 2011, available at http://www.comlab. ox.ac.uk/pseudospectra.

[Eyer et al. 1979] A. Eyer, R. Nitsche, and H. Zimmermann, "A double-ellipsoid mirror furnace for zone crystallization experiments in spacelab", J. Cryst. Growth 47:2 (1979), 219–229.

[Eyer et al. 1985] A. Eyer, H. Leiste, and R. Nitsche, "Floating zone growth of silicon under microgravity in a sounding rocket", J. Cryst. Growth 71:1 (1985), 173–182.

[Houchens and Walker 2001] B. C. Houchens and J. S. Walker, "Magnetic damping of the

thermocapillary instability during floating-zone crystal growth in space", in Conference and exhibit on international space station utilization (Cape Canaveral, FL, 2001), AIAA, Reston, VA, 2001. Paper #2001-5053.

[Houchens and Walker 2005] B. C. Houchens and J. S. Walker, "Modeling the floating zone: instabilities in the half zone and full zone", J. Thermophys. Heat Transf. 19:2 (2005), 186–198.

[Huang and Houchens 2011] Y. Huang and B. C. Houchens, "Magnetic stabilization, transition and energy analysis in the Marangoni driven full-zone at low Prandtl numbers", Eur. Phys. J. Spec. Top. 192:1 (2011), 47–62.

[Intel 2008] Intel, "Intel math kernel library", 2008, available at http://software.intel.com/en-us/intel-mkl.

[Kasperski et al. 2000] G. Kasperski, A. Batoul, and G. Labrosse, "Up to the unsteadiness of axisymmetric thermocapillary flows in a laterally heated liquid bridge", Phys. Fluids 12:1 (2000), 103–119.

[Lan and Yeh 2004] C. W. Lan and B. C. Yeh, "Three-dimensional simulation of heat flow, segregation, and zone shape in floating-zone silicon growth under axial and transversal magnetic fields", J. Cryst. Growth 262:1-4 (2004), 59–71.

[Lan and Yeh 2005] C. W. Lan and B. C. Yeh, "Effects of rotation on heat flow, segregation, and zone shape in a small-scale floating-zone silicon growth under axial and transversal magnetic fields", Fluid Dyn. Mater. Process. 1:1 (2005), 33–44.

[Lappa 2004] M. Lappa, "Combined effect of volume and gravity on the three-dimensional flow instability in noncylindrical floating zones heated by an equatorial ring", Phys. Fluids 16:2 (2004), 331–443.

[Lappa 2005a] M. Lappa, "Analysis of flow instabilities in convex and concave floating zones heated by an equatorial ring under microgravity conditions", Comput. Fluids 34:6 (2005), 743–770.

[Lappa 2005b] M. Lappa, "Review: possible strategies for the control and stabilization of Marangoni flow in laterally heated floating zones", Fluid Dyn. Mater. Process. 1:2 (2005), 171–188.

[Levenstam and Amberg 1995] M. Levenstam and G. Amberg, "Hydrodynamical instabilities of thermocapillary flow in a half-zone", J. Fluid Mech. 297 (1995), 357–372.

[Levenstam et al. 2001] M. Levenstam, G. Amberg, and C. Winkler, "Instabilities of thermocapillary convection in a half-zone at intermediate Prandtl numbers", Phys. Fluids 13:4 (2001), 807–816.

[Leypoldt et al. 2000] J. Leypoldt, H. C. Kuhlmann, and H. J. Rath, "Three-dimensional numerical simulation of thermocapillary flows in cylindrical liquid bridges", J. Fluid Mech. 414 (2000), 285–314.

[Martinez and Eyer 1986] I. Martinez and A. Eyer, "Liquid bridge analysis of silicon crystal growth experiments under microgravity", J. Cryst. Growth 75:3 (1986), 535–544.

[Morthland and Walker 1996] T. E. Morthland and J. S. Walker, "Thermocapillary convection during

floating-zone silicon growth with a uniform or non-uniform magnetic field", J. Cryst. Growth 158:4 (1996), 471–479.

[Nakamura et al. 1998] S. Nakamura, T. Hibiya, K. Kakimoto, N. Imaishi, S. Nishizawa, A. Hirata, K. Mukai, S. Yoda, and T. S. Morita, "Temperature fluctuations of the Marangoni flow in a liquid bridge of molten silicon under microgravity on board the TR-IA-4 rocket", J. Cryst. Growth 186:1-2 (1998), 85–94.

[Prange et al. 1999] M. Prange, M. Wanschura, H. C. Kuhlmann, and H. J. Rath, "Linear stability of thermocapillary convection in cylindrical liquid bridges under axial magnetic fields", J. Fluid Mech. 394:1 (1999), 281–302.

[Reddy and Trefethen 1990] S. C. Reddy and L. N. Trefethen, "Lax-stability of fully discrete spectral methods via stability regions and pseudo-eigenvalues", Comput. Methods Appl. Mech. Eng. 80:1-3 (1990), 147–164.

[Saad 1992] Y. Saad, Numerical methods for large eigenvalue problems, Manchester University Press, Manchester, 1992. [Takagia et al. 2001] K. Takagia, M. Otaka, H. Natsui, T. Arai, S. Yoda, Z. Yuan, K. Mukai, S. Yasuhiro, and N. Imaishi, "Experimental study on transition to oscillatory thermocapillary flow in a low Prandtl number liquid bridge", J. Cryst. Growth 233:1-2 (2001), 399–407.

[Trefethen and Embree 2005] L. N. Trefethen and M. Embree, Spectra and pseudospectra: the behavior of nonnormal matrices and operators, Princeton University Press, Princeton, NJ, 2005.

CRITICAL THRESHOLD AND UNDERLYING DYNAMICAL PHENOMENA IN PEDESTRIAN-INDUCED LATERAL VIBRATIONS OF FOOTBRIDGES

STEFANO LENCI AND LAURA MARCHEGGIANI

ABSTRACT

The problem of lateral vibrations of footbridges due to the synchronization of the pedestrians' motion with that of the supporting structure is analyzed by means of a 3D discrete time model. The map is linear in the mechanical part, and nonlinear in the synchronization part. A very simple and predictive formula is obtained for the critical number of pedestrians, which also takes into account the imperfect resonance between the pedestrians' natural frequencies and the bridge frequency. It is shown that the underlying mechanism triggering the sudden appearance of swaying bridge motion is a perturbation of a pitchfork bifurcation. The results presented in this paper are not related to a specific real case and are based on a quite reasonable hypothesis, and therefore it is expected that they have general validity.

1. Introduction

As a consequence of the technological development of new materials and of the architectural trend toward lightness and slenderness, modern footbridges have small natural frequencies, which can resonate with those of the pedestrian-induced load [Živanovic et al. 2005; Venuti and Bruno 2009], which are in the ´ range 1.4–2.4 Hz for vertical forcing and in the range 0.7–1.2 Hz for horizontal (lateral) forcing. In this situation unwanted large bridge motions may occur.

Various footbridges have experienced excessive lateral vibrations due to pedestrian-induced loads; the most famous is the London Millennium Bridge, which underwent, on its opening day, large horizontal vibrations due to the synchronization of the pedestrians' motion with the natural modes of the structure [Dallard et al. 2001a; 2001b]. Other bridges which have suffered similar problems are the Toda Park Bridge [Fujino et al. 1993; Nakamura and Kawasaki 2006] and the Maple Valley Bridge [Nakamura and Kawasaki 2006] in Japan, the Solferino Footbridge in Paris [Danbon and Grillaud 2005], and the Alexandra Bridge in Ottawa [Dallard et al. 2001a].

The pedestrian-induced lateral vibrations occurred in bridges of different structural types (suspension, cable-stayed, and steel girder bridges) as well as on footbridges made of different materials (steel, posite steel-concrete, and reinforced and prestressed concrete) [Živanovic et al. 2005]. It is therefore ´ confirmed that a large-enough crowd of pedestrians can induce strong lateral vibrations on footbridges of any type, although this requires the lateral mode to have a low-enough natural frequency [Dallard et al. 2001a], approximately below 1.2 Hz, as stated.

The phenomenon behind pedestrian-induced lateral vibrations on footbridges is that of synchronous lateral excitation [Dallard et al. 2001a; Strogatz et al. 2005; Živanovic et al. 2005; Eckhardt et al. 2007].

People walking in a crowd exhibit a random level of synchrony, and in general produce a lateral force on the bridge. In fact, even if the bridge is still and the pedestrians are not synchronized at all, due to the stochasticity of the process the net force, which is the sum of all the lateral forces applied to the bridge by the footsteps of pedestrians, is not null, although it is possibly small. This small force produces small oscillations of the bridge.

As soon as the small bridge vibrations become perceptible to the unconscious human cognition pro cesses, pedestrians tend spontaneously to walk in synchrony with the bridge, by slightly changing their walking frequency and phase. Of course, this tendency is somehow proportional to the vibration am plitude, and so it is very small, and possibly negligible, for very small displacements. However, it is believed that this phenomenon starts for very low levels of amplitude of the motion, well below the amplitude threshold perceived by conscious feeling.

This instinctive behavior, which is the mechanism through which the pedestrians interact with the bridge, produces an increase of the synchronization level, and the associated net force grows. This estab lishes an unwanted positive feedback loop, where the increase in oscillation amplitude causes pedestrians to increase their lateral footfall forcing and their level of synchrony, by following the of the deck in order to balance themselves [Dallard et al. 2001a; 2001b]: the more the bridge moves, the more the crowd pushes it to move further.

It has been observed that for potentially susceptible spans there is a critical number of pedestrians Ncr that will cause the vibrations to increase suddenly to unacceptable levels. The oscillations are small below Ncr and, due to the synchronization, they increase rapidly above Ncr. This critical threshold is of great practical interest, and its prediction is the goal of almost all studies. This paper aims to provide a simple and reliable analytical prediction of Ncr, as well as to further understanding of the overall phenomenon.

The nature of the problem is nonlinear, as has been confirmed, for example, by tests performed on the London Millennium Bridge [Dallard et al. 2001a]; in spite of this, however, it can be detected within a mechanically linear framework, since even the “large” oscillations are orders of magnitude smaller than the span length. The nonlinearity is only in the interaction between the structure and pedestrians.

Several papers have recently addressed this topic, even if a standard and generally accepted model of pedestrian-induced lateral dynamic loading and of dynamical interaction with the bridge is still missing. Živanovic et al. [2005] have performed a comprehensive review of the existing literature on the topic ´ until 2003, while an updated review can be found in [Venuti and Bruno 2009].

Early studies on pedestrian-induced vibrations of footbridges [Blanchard et al. 1977; Matsumoto et al. 1978; Wheeler 1980] concerned only the measurement and modeling of the vertical component of pedes trian load on a motionless surface.

Dallard et al. [2001a; 2001b] have conducted a series of controlled crowd tests on the Millennium

Bridge and have proposed a load model based on empirical observations. Also a formula has been ob tained for the critical number of pedestrians; it actually depends only on the modal damping of the bridge through a proportionality constant which is strictly related to the specific real case-study (the Millennium Bridge). The findings of the present paper extend somewhat these works, by better highlighting the nature of this constant (for example, that it depends on the bridge natural frequency).

Nakamura [2004] has proposed an interactive forcing model analogous to the previous one, but which allows the schematization of the self-limiting nature of the synchronization phenomenon and the tion of the steady-state amplitude. Also this model is based on coefficients which have been estimated from experimental tests [Fujino et al. 1993; Nakamura and Kawasaki 2006] and cannot easily be generalized to other footbridges.

In [Newland 2003] the problem is approached by referring to the interaction phenomenon between fluid flow and structures which is widely studied in wind engineering and commonly known as lock-in.

His model includes the empirical assumption that 40% of the pedestrians are synchronized with the bridge lateral frequency, independent of the amplitude of the oscillations.

Fujino et al. [1993] have adopted a model of harmonic forcing by empirically tuning a synchronization parameter for the lateral vibrations of the Toda Park Bridge (according to their experimental data). This model does not predict any sudden transition to a vibrating state of the bridge but assumes a continuous increase in the vibration amplitude as the number of pedestrians increases.

Roberts [2005] has schematized the interaction between the pedestrians and the footbridge assuming that synchronization occurs when the pedestrians' motion is larger than the bridge motion; from this critical condition, he has obtained a limit number of pedestrians.

In [Ricciardelli and Pizzimenti 2007] a systematic experimental campaign has been performed aimed at characterizing dynamically the lateral force exerted by pedestrians on footbridges, both in the case of a still deck and in the case of a laterally moving deck; deterministic and stochastic lateral loading models for the static case have been provided and the bases have been put in place for more sophisticated dynamic models including crowd-structure interaction. The mechanism of crowd synchronization has been investigated only from the qualitative point of view, deferring quantitative study and modeling until after further measurements.

The excessive lateral vibrations of the Solferino Bridge in Paris have been explained in [Blekherman 2007] on the basis of autoparametric resonance by using a double pendulum model; the process of possible synchronization of pedestrian loading with the relevant vibrational modes, which are nonlinearly coupled in a ratio of 2:1 between their frequencies, depends on the achievement of parametric resonance.

Piccardo and Tubino [2008] have performed an interesting extensive critical analysis of the mechanisms identified in the literature and they have proposed a new forcing model based on experi

mental tests carried out on harmonically moving platforms [Dallard et al. 2001a]. The force exerted by pedestrians is modeled as harmonic with an amplitude depending on the deck lateral displacement, and a simple criterion defining the limit pedestrian mass is introduced. They mainly ascribe to a mechanism of parametric excitation the lateral sway motion induced by crowds in very flexible, lowly damped footbridges, with a first lateral natural frequency around 0.5 Hz corresponding to half of the first lateral walking frequency.

In Venuti et al. [2007] a first-order model has been developed based on the mass conservation equation, in order to macroscopically describe the dynamics of the crowd in the framework of hydrodynamic mod eling. The crowd, considered as a pedestrian flow, is assumed to behave like a continuous compressible fluid; the structural system is modeled by means of a generalized single degree of freedom (SDOF) model.

The two-way interaction between the crowd and the structure is studied. This model permits taking into account the triggering of the lock-in and its self-limited nature, previously explained only in [Strogatz et al. 2005]. The effects of the two different kinds of synchronization, that is, between the pedestrians and the structure and among the pedestrians, are introduced; the presence of different frequency components in the overall force exerted by the pedestrians is considered. Some parameters, used in the formulation of the model, come from reasonable qualitative considerations about pedestrian behavior and would require specific experimental tests to be confirmed.

In [Bodgi et al. 2007] a similar approach has been adopted to simulate the mechanics of synchronous lateral excitation induced by pedestrians on footbridges.

Strogatz et al. [2005] have been the first, to the best of our knowledge, to mathematically describe and predict the simultaneous growth of bridge movement and crowd synchronization, an observation that was unexplained in previous models but that is confirmed by analyses of video footage [Arup 2000] recorded during overcrowding conditions on real footbridges [Fujino et al. 1993; Dallard et al. 2001a]. They proposed a model (called SAMEO in [Marcheggiani and Lenci 2010] from the initials of the authors) which is particularly interesting for its contribution to the physical-mathematical explanation of the underlying mechanical event, as well as for the reasonable description of the phenomenon itself.

The SAMEO model is quite simple in its formulation and general enough to be possibly applied to any bridge at risk of synchronous lateral excitation. It models the bridge as a SDOF oscillator that interacts nonlinearly with each pedestrian. The pedestrians are modeled as limit-cycle phase oscillators (this choice comes from a similitude with biological systems, for example, fireflies). The key parameter of the model, C, measures the pedestrians sensitivity to bridge lateral vibrations; it can be determined only experimentally.

The SAMEO model has been investigated in depth in [Marcheggiani and Lenci 2010], where extensive numerical simulations have been performed in order to detect the effects of the main parameters on the

system's response, in particular on the critical threshold. Various extensions have been proposed to model some important aspects not considered in [Strogatz et al. 2005], such as, for example, the self-interaction between pedestrians.

Although the original model and its extensions are simple in their formulation and meaning, they are quite involved in terms of the associated equations of motion, which is a set of N + 2 (N being the number of pedestrians) nonlinear ordinary differential equations. This system can be fully solved only numerically, although some approximated analytical techniques have been obtained in [Abrams 2006] to get some partial information. This is a limitation of the model, together with the fact that it does not provide immediate information.

In order to overcome the previous drawbacks, in [Lenci and Marcheggiani 2008] a simplified model is proposed and applied with some success to the case of the Millennium Bridge. The main idea is that of passing from ordinary differential equations to maps, that is, from a continuous time system to a discrete time one. In particular, a peak-to-peak map [Candaten and Rinaldi 2000], similar to that introduced by Lorenz in discovering chaotic attractors, has been considered and analyzed in depth. The discrete time permits simple computations (which can be performed by hand), and provides a simple but very predictive formula for Ncr and a better understanding of the dynamical phenomena lurking in the background.

The work [Lenci and Marcheggiani 2008] is continued in this paper; another discrete time model is proposed, now based on the stroboscopic Poincaré map (instead of the peak-to-peak map). The mechani cal part is described by the position x and velocity y, while the bridge-pedestrian interaction is described by a new state variable σ measuring the degree of synchronization of the pedestrians. We thus get a 3D map, linear in the mechanical part and nonlinear only in the interaction part, whose behavior is analyzed without exact knowledge of the evolution law for σ. Just its overall properties and local behavior are used, thus providing a very general analysis, which in particular extends that of [Lenci and Marcheggiani 2008]. The main results are obtained by a bifurcation analysis of the fixed points of the map, which of course is specific to the considered simplified model.

This paper is organized as follows. In Section 2 the mechanical model is illustrated leading to the me chanical part of the discrete time model. Then, the pedestrian-bridge interaction is analyzed in Section 3, where the main properties of the third evolution law are discussed. The fixed points of the map, which are the dynamical behaviors of interest for the computation of the critical threshold, are considered in Section 4, where a simple formula for Ncr is obtained, and where the effect of imperfections is discussed. Some properties of the map in the resonant case are discussed in Section 5, and conclusions are presented in Section 6.

2. Mechanical model

Based on experience in real cases, in particular on that of the London Millennium Bridge mentioned in Section 1, we assume that the phenomenon of lateral synchronization involves only one lateral mode ϕ(Z) of the structure, so that the mechanical equation of motion is

$$M\,\ddot{X}(T) + B\,\dot{X}(T) + K\,X(T) = F(T), \tag{1}$$

where M, B, and K are the modal mass, damping, and stiffness, respectively, and X(T) is the modal amplitude. Note that M includes also the mass of the pedestrians, and in general is not a fixed number. However, in real cases the mass of pedestrians is about 10–15% of the total mass, and so it is expected that it does not play a key role. F(T) is the modal force, that is, the projection on the considered mode ϕ(Z) of the force F(Z, T) exerted by pedestrians along the span, F(T) = R L 0 F(Z, T)ϕ(Z)d Z. In fact, the load of each pedestrian depends not only on the force he applies on the bridge, but also on his position Z ∈ [0, L] along the span.

The definitions

$$\Omega = \sqrt{\frac{K}{M}}, \quad t = \Omega T, \quad \xi = \frac{B}{2\sqrt{MK}} = \frac{B\Omega}{2K}, \quad x(t) = X(T), \quad f(t) = \frac{F(T)}{K}, \tag{2}$$

where Ω is the natural frequency of the considered mode, permit us to rewrite (1) in the form

$$\ddot{x}(t) + 2\xi\dot{x}(t) + x(t) = f(t), \tag{3}$$

which will be used in the following. Note that the time t is dimensionless, while x has the dimension of length.

2.1. A single pedestrian and the stroboscopic Poincaré map. We initially consider the effect of a single pedestrian by assuming

$$f(t) = g\,\sin(\omega_p t - \phi), \tag{4}$$

where:

- $g > 0$ is the dimensionless amplitude, such that $G = gK \cong 30N$ is the maximum lateral force exerted by a pedestrian [Belli et al. 2001; Marcheggiani and Lenci 2010];
- ω_p is the dimensionless (circular) frequency, such that $f_p = \Omega_p/(2\pi) = \Omega\omega_p/(2\pi) = 0.7–1.2\,\text{Hz}$ is the pedestrian footstep native frequency [Živanović et al. 2005]; and
- $\phi \in [0, 2\pi]$ is the pedestrian phase, which depends on the time the pedestrian enters the bridge.

Equation (4) is an approximation of the real force, since experimental data concerning lateral walking forces on a still surface [Bodgi et al. 2007; Ricciardelli and Pizzimenti 2007] have shown that it is much closer to a square wave than to a harmonic force [Belli et al. 2001]. However, expression (4) can be considered as the first term in the Fourier series of the real excitation, thus capturing the most energy content and maintaining the simple expression needed for analytical computations.

The solution of (3) and (4) starting from $x(0) = x_n$ and $\dot{x}(0) = y_n$ is

$$x(t) = e^{-\xi t}\left[c_1 \sin\left(t\sqrt{1-\xi^2}\right) + c_2 \cos\left(t\sqrt{1-\xi^2}\right)\right] + g[d_1 \sin(\omega_p t) + d_2 \cos(\omega_p t)], \tag{5}$$

where

$$\begin{aligned} d_1 &= \frac{(1-\omega_p^2)\cos(\phi) - 2\xi\omega_p \sin(\phi)}{(1-\omega_p^2)^2 + (2\xi\omega_p)^2}, & d_2 &= \frac{-(1-\omega_p^2)\sin(\phi) - 2\xi\omega_p \cos(\phi)}{(1-\omega_p^2)^2 + (2\xi\omega_p)^2}, \\ c_1 &= \frac{\xi x_n + y_n - \omega_p g d_1 - \xi g d_2}{\sqrt{1-\xi^2}}, & c_2 &= -g d_2 + x_n. \end{aligned} \tag{6}$$

Note that the initial conditions do not modify d_1 and d_2, only c_1 and c_2.

After one period $T_p = 2\pi/\omega_p$ of the excitation we have from (5)

$$x(T_p) = e^{-\xi T_p}\left[c_1 \sin\left(T_p\sqrt{1-\xi^2}\right) + c_2 \cos\left(T_p\sqrt{1-\xi^2}\right)\right] + g d_2 \tag{7}$$

and

$$\dot{x}(T_p) = e^{-\xi T_p}\left[\left(-c_1\xi - c_2\sqrt{1-\xi^2}\right)\sin\left(T_p\sqrt{1-\xi^2}\right) + \left(-c_2\xi + c_1\sqrt{1-\xi^2}\right)\cos\left(T_p\sqrt{1-\xi^2}\right)\right] + g\omega_p d_1. \tag{8}$$

The main idea of this paper consists in moving from a continuous time system, (3), to a discrete one. This can be obtained by introducing an appropriate Poincaré section of the continuous flow, and by considering the associated Poincaré return map [Wiggins 1997].

We use the stroboscopic Poincaré map obtained by sampling the system position and velocity at each *excitation* period $T_p = 2\pi/\omega_p$, which is mathematically well defined. It is given by

$$\begin{Bmatrix} x_{n+1} \\ y_{n+1} \end{Bmatrix} = \begin{Bmatrix} f_x(x_n, y_n) \\ f_y(x_n, y_n) \end{Bmatrix} = e^{-\xi T_p} \begin{bmatrix} \alpha_x & \alpha_{xy} \\ -\alpha_{xy} & \alpha_y \end{bmatrix} \begin{Bmatrix} x_n \\ y_n \end{Bmatrix} + g \begin{Bmatrix} \beta_x \\ \beta_y \end{Bmatrix}, \tag{9}$$

where use is made of (7) and (8), and where $x_{n+1} = x(T_p)$ and $y_{n+1} = \dot{x}(T_p)$ (see [Wiggins 1997]), the functions $f_x(x_n, y_n)$ and $f_y(x_n, y_n)$ are defined by the last equality, and

$$\begin{aligned} \alpha_x &= \xi \frac{\sin\left(T_p\sqrt{1-\xi^2}\right)}{\sqrt{1-\xi^2}} + \cos\left(T_p\sqrt{1-\xi^2}\right), & \alpha_y &= -\xi \frac{\sin\left(T_p\sqrt{1-\xi^2}\right)}{\sqrt{1-\xi^2}} + \cos\left(T_p\sqrt{1-\xi^2}\right), \\ \alpha_{xy} &= \frac{\sin\left(T_p\sqrt{1-\xi^2}\right)}{\sqrt{1-\xi^2}}, & & \\ \beta_x &= e^{-\xi T_p}(-\omega_p d_1 \alpha_{xy} - d_2\alpha_x) + d_2, & \beta_y &= e^{-\xi T_p}(-\omega_p d_1 \alpha_y + d_2\alpha_{xy}) + \omega_p d_1. \end{aligned} \tag{10}$$

Note that in the resonant case $T_p = 2\pi/\sqrt{1-\xi^2}$ we have $\alpha_x = \alpha_y = 1$, $\alpha_{xy} = 0$, $\beta_x = d_2(1 - e^{-\xi T_p})$, and $\beta_y = \omega_p d_1(1 - e^{-\xi T_p})$.

2.2. Crowd of pedestrians. When a crowd of N uniformly distributed pedestrians is walking on the bridge the net force is

$$f(t) = \sum_{i=1}^{N} g_i \sin(\omega_{p,i} t - \phi_i). \tag{11}$$

In principle, the parameters gi and ωp,i are stochastic variables which depend on the age, health condition, height, etc., of the population of pedestrians. However, φi , which is also a stochastic depends only on the instant of time the pedestrian enters the bridge, and not on his human characteristics.

Single pedestrian action is modeled by (4) and the action of the crowd by (11); we neglect the in teractions between pedestrians, and focus only on the interaction of each pedestrian with the bridge, which is the main mechanism responsible for the considered phenomenon. For the pedestrian-pedestrian interactions, an interesting topic involving complex living systems, but which is out of the scope of this paper, we refer to, for example, [Johansson et al. 2008].

In the following we make the assumption that each pedestrian of the crowd has the same natural frequency, $\omega_{p,i} = \omega_p$. This is motivated by the fact that only pedestrians with a natural frequency close to that of the bridge can undergo the synchronization phenomenon we are dealing with, since it involves resonance. This fact is confirmed by the movie of the opening of the Millennium Bridge [Arup 2000], where it is clearly seen that only some pedestrians synchronize (it was estimated at about 40% [Newland 2003]). The others are not influenced by the bridge motion and maintain their natural walking, and so, by stochastic arguments, we can assume that they provide a zero net force on the bridge and thus are not of interest. We conclude that only a narrow band of native frequencies is of real interest, and we consider just one, ω_p, in order to fulfill the objective of having a simple, but predictive, model.

By the previous basic hypothesis, which guarantees that the stroboscopic Poincaré map is still well defined, we have that (11) becomes

$$f(t) = \sin(\omega_p t) \sum_{i=1}^{N} g_i \cos(\phi_i) - \cos(\omega_p t) \sum_{i=1}^{N} g_i \sin(\phi_i). \tag{12}$$

The summations appearing in (12) depend on the degree of synchronization of the pedestrians, that is, on the degree of correlation of their phases ϕ_i.

In the case of *perfectly asynchronous* pedestrians we have that ϕ_i is a stochastic variable uniformly distributed in $[0, 2\pi]$, which implies that

$$\sum_{i=1}^{N} g_i \cos(\phi_i) = \sum_{i=1}^{N} g_i \sin(\phi_i) = 0 \quad \Rightarrow \quad f(t) = 0. \tag{13}$$

This can be seen by a standard Monte Carlo analysis. In practice in this case for each pedestrian there exists, on average, a pedestrian with opposite phase.

In the *perfectly synchronous* case pedestrians have exactly the same phase, $\phi_i = \phi \pm 2n\pi$, so that

$$\sum_{i=1}^{N} g_i \cos(\phi_i) = \cos(\phi) \sum_{i=1}^{N} g_i = \cos(\phi) N g_{\text{av}}, \quad \sum_{i=1}^{N} g_i \sin(\phi_i) = \sin(\phi) \sum_{i=1}^{N} g_i = \sin(\phi) N g_{\text{av}}, \tag{14}$$

and

$$f(t) = N g_{\text{av}} \sin(\omega_p t - \phi). \tag{15}$$

In the previous expressions N is the number of (synchronized) pedestrians whose frequency is close to ω_p, that is, a subset of the total number of pedestrians walking on the bridge (see previous comments); only in calibrated experiments with controlled people is N the total number of pedestrians. The average

force of each pedestrian is gav, such that Gav = gavK ∼= 30N (see Section 2.1), and φ is the average phase; its value is inessential, and it will be used in due course to simplify the computations.

From the previous expressions we see that f (t) ranges from f (t) = 0 (the perfectly asynchronous case) to f (t) = N gav sin(ωpt − φ) (the perfectly synchronous case). In real cases the actual force is in between these two bounds, and depends on the degree of synchronization. Thus we assume

$$f(t) = N g_{\mathrm{av}} \sigma \sin(\omega_p t - \phi), \tag{16}$$

where σ is a dimensionless measure of the degree of synchronization, which ranges from 0 (the perfectly asynchronous case) to 1 (the perfectly synchronous case).

Equation (16) is formally identical to (4), so that mathematically we bring back the crowd case to that of an equivalent (single) pedestrian, and we can take advantage of the formulas of Section 2.1. In doing this, we use the "free" overall phase to simplify the expressions. In particular, by assuming (without loss of generality)

$$\sin(\phi) = \frac{-2\xi\omega_p}{\sqrt{(1-\omega_p^2)^2 + (2\xi\omega_p)^2}}, \quad \cos(\phi) = \frac{1-\omega_p^2}{\sqrt{(1-\omega_p^2)^2 + (2\xi\omega_p)^2}}, \tag{17}$$

we have

$$d_1 = \frac{1}{\sqrt{(1-\omega_p^2)^2 + (2\xi\omega_p)^2}}, \quad d_2 = 0, \tag{18}$$

so that

$$\beta_x = -\omega_p d_1 e^{-\xi T_p} \alpha_{xy}, \quad \beta_y = \omega_p d_1 (-e^{-\xi T_p} \alpha_y + 1). \tag{19}$$

The map (9) becomes

$$\begin{Bmatrix} x_{n+1} \\ y_{n+1} \end{Bmatrix} = e^{-\xi T_p} \begin{bmatrix} \alpha_x & \alpha_{xy} \\ -\alpha_{xy} & \alpha_y \end{bmatrix} \begin{Bmatrix} x_n \\ y_n \end{Bmatrix} + \sigma \bar{N} \begin{Bmatrix} -e^{-\xi T_p} \alpha_{xy} \\ 1 - e^{-\xi T_p} \alpha_y \end{Bmatrix}, \tag{20}$$

where

$$\bar{N} = \frac{N g_{\mathrm{av}} \omega_p}{\sqrt{(1-\omega_p^2)^2 + (2\xi\omega_p)^2}}. \tag{21}$$

3. Pedestrian-bridge interaction

In the previous section only the mechanical part has been considered. In order to model the dynamical bridge-pedestrian interaction and to describe the natural tendency of the systems to synchronize, we must consider also the human part, starting from the basic observation that the two parts influence each other.

The first step in this direction is to assume that not only xn and yn vary in (discrete) time, but also the synchronization parameter σ, which is now considered as a state variable, σn, and no longer as a (fixed)

parameter. Thus, (20) becomes

$$\begin{Bmatrix} x_{n+1} \\ y_{n+1} \end{Bmatrix} = \begin{Bmatrix} f_x(x_n, y_n, \sigma_n) \\ f_y(x_n, y_n, \sigma_n) \end{Bmatrix} = e^{-\xi T_p} \begin{bmatrix} \alpha_x & \alpha_{xy} \\ -\alpha_{xy} & \alpha_y \end{bmatrix} \begin{Bmatrix} x_n \\ y_n \end{Bmatrix} + \sigma_n \bar{N} \begin{Bmatrix} -e^{-\xi T_p} \alpha_{xy} \\ 1 - e^{-\xi T_p} \alpha_y \end{Bmatrix}. \tag{22}$$

Note that the passage from (20) to (22) is not a simple substitution of σ with σn, but a conceptual change which, for example, increases the dimension of the dynamical system.

The next step consists in proposing a (discrete time) evolution law for the new state variable σn:

$$\sigma_{n+1} = f_\sigma(x_n, y_n, \sigma_n), \tag{23}$$

so that (22) and (23) become a well-defined dynamical system. The choice of the function fσ (xn, yn, σn) entails modeling the bridge-pedestrian interaction, and so it is the key point. In fact, while for the mechanical part (22) there are physical (Newtonian) laws, for the human part (23) there are no corresponding axiomatic laws, and any choice is by definition subjective.

Common sense suggests that the degree of synchronization strongly depends on the amplitude,

$$A_n = \sqrt{x_n^2 + \frac{y_n^2}{\omega_p^2}}, \tag{24}$$

of the bridge motion, and weakly on the current synchronization σn. Thus, in this work we assume

$$\sigma_{n+1} = f_\sigma(A_n). \tag{25}$$

The following properties help in the characterization of the nonlinear function fσ (An):

(1) $f_\sigma(0) = 0$. In fact, in a (mathematically) *perfect* case, in the absence of motion there is no synchronization at all and the force on the bridge is zero. Actually, since the synchronization is a stochastic process, in real (or *imperfect*) cases even if the bridge is still, the lack of synchronization is not perfect, and there is a net force, although very small. This is achieved by assuming $f_\sigma(0) = \varepsilon$, $|\varepsilon| \ll 1$. In the sequel we will consider both the perfect and the imperfect cases.

(2) $f_\sigma(A_n)$ is a monotonic increasing function, since there is experimental evidence that the degree of synchronization increases with the amplitude of the motion.

(3) $f_\sigma(A_n)$ is as simple as possible, since there is no experimental evidence for strange behaviors for certain values of A_0. Mathematically this property can be formulated by assuming that $f_\sigma(A_n)$ is smooth, that is, continuously differentiable, in $]0, \infty[$ and that it has at maximum one inflection point.

(4) $\lim_{A_n \to \infty} f_\sigma(A_n) = 1$, as, for large excitation amplitudes, *all* the pedestrians synchronize (that is, there is no asymptotic limit less than 1). This property mathematically describes the saturation condition; in practice the rate of convergence toward 1 is important, since it is practically expected that for large but finite values of A_n we have achieved a practically complete synchronization.

Any function satisfying the previous four points is acceptable in principle.

For the forthcoming developments the most important characteristic of the function fσ (An) is its behavior around the origin An = 0. Without loss of generality we can assume the following local behavior:

$$f_\sigma(A_n) = \varepsilon + \gamma_k (A_n)^k + \ldots, \tag{26}$$

where ε is the imperfections parameter (see point (1)), k is a positive real number determining the local rate of convergence toward An = 0, and γk is a parameter measuring the "slope" of the local behavior, that is, the sensitivity of the pedestrians to the movement of the bridge. Both k and γk are parameters of the model to be determined theoretically or experimentally.

4. Fixed points

Now that we have the map ((22) and (25)) describing the evolution law for the coupled bridge-pedestrian system we can study its dynamic behavior. We start by considering the fixed points

$$x_0 = f_x(x_0, y_0, \sigma_0), \quad y_0 = f_y(x_0, y_0, \sigma_0), \quad \sigma_0 = f_\sigma(A_0), \quad A_0 = \sqrt{x_0^2 + \frac{y_0^2}{\omega_p^2}}, \tag{27}$$

which correspond to periodic oscillations of the original continuous time system.

Solving the first two equations of (27) yields

$$x_0 = 0, \quad y_0 = \sigma_0 \bar{N} \quad \Rightarrow \quad A_0 = \frac{\sigma_0 \bar{N}}{\omega_p}. \tag{28}$$

Substituting this expression in $(27)_3$ gives the nonlinear algebraic equations permitting determination of the fixed points:

$$\sigma_0 = f_\sigma\left(\frac{\sigma_0 \bar{N}}{\omega_p}\right) \quad \Rightarrow \quad \frac{\omega_p}{\bar{N}} A_0 = f_\sigma(A_0). \tag{29}$$

Equation (29) can be graphically solved by drawing the graph of $f_\sigma(A_0)$ and of the straight line $(\omega_p/\bar{N})A_0$, as schematically shown in Figure 1. This permits the inference of the main qualitative properties of the solution without exact knowledge of the function $f_\sigma(A_0)$.

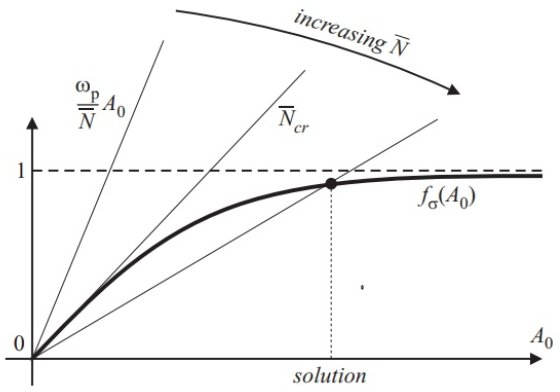

Figure 1. A schematic representation of the graphical solution of (29).

The solutions of (29) are now discussed by considering separately the perfect (ε = 0, Figure 1) and imperfect (ε 6= 0) cases, and by using N as a varying (driving) parameter for parametric analysis and for bifurcation diagrams.

4.1. Perfect case. In the perfect case fσ (0) = 0, so that we have the trivial (or rest) solution A0 = 0corresponding to the still bridge (see (29) and Figure 1). This is the main path of solutions.

To determine if there are secondary solutions bifurcating from the trivial one, we consider the local behavior (26) of fσ (A0), so that (29) becomes

$$\frac{\omega_p}{\bar{N}} A_0 = \gamma_k A_0^k + \dots . \tag{30}$$

From the previous equation we conclude that if $k \neq 1$ there are no solutions in the neighborhood of $A_0 = 0$ for finite values of $\bar{N}$, that is, there are no bifurcation points.

If, on the other hand, $k = 1$, then there is a branching at (we write γ instead of γ_1 for simplicity)

$$\bar{N}_{\text{cr}} = \frac{\omega_p}{\gamma}, \tag{31}$$

which, as shown in Figure 1, corresponds to the $\bar{N}$ providing the same slope at the origin for $f_\sigma(A_0)$ and $(\omega_p/\bar{N})A_0$.

Combining (21) and (31) we get

$$N_{\text{cr}} = \frac{\sqrt{(1-\omega_p^2)^2 + (2\xi\omega_p)^2}}{\gamma g_{\text{av}}}. \tag{32}$$

This expression is the most important result from a practical point of view, since it gives the critical number of pedestrians triggering the phenomenon of lateral synchronization, that is, the maximum num ber of (synchronizable) pedestrians allowed on the bridge deck. In fact, below this threshold there is only the rest solution, so nothing happens. It is just at this Ncr that a different solution becomes possible, and the swaying of the bridge appears. This is enough from a designer point of view, and it is valuable because (32) is a very simple formula obtained with reasonable hypotheses. In particular, it does not require knowledge of the whole function fσ (A0), but only of its local behavior.

The model parameter γ , which has dimensions of inverse length, measures the sensitivity of the pedestrians to the bridge motion. Its meaning can be understood by considering the following piecewise linear expression, which is the simplest choice for fσ (A0):

$$f_\sigma(A_0) = \begin{cases} \gamma A_0, & \text{for } 0 < A_0 \leq \dfrac{1}{\gamma}, \\ 1, & \text{for } A_0 \geq \dfrac{1}{\gamma}. \end{cases} \tag{33}$$

This expression shows that 1/γ can be approximately considered as the amplitude such that all the synchronizable pedestrians are actually synchronized. In fact, the limit for An → ∞ in point (4) is just a

mathematical issue, since in practice the phenomenon occurs for small (or moderately small) displacements, justifying the mechanically linear framework used in (1).

Expression (32) provides the critical number as a function of the pedestrians' native frequency ωp. The worst situation corresponds to the resonant case, because in this case each pedestrian has the maximum effect on the bridge. In fact, by minimizing (32) with respect to ωp we get

$$\omega_{p,\min} = \sqrt{1-2\xi^2} = \omega_{\text{res}}, \tag{34}$$

confirming, as expected, that the resonance is the worst situation. By inserting (34) into (32) we obtain

$$N_{\text{cr,min}} = \frac{2\xi}{\gamma g_{\text{av}}} = \frac{B}{\sqrt{MK}}\frac{1}{\gamma}\frac{K}{G_{\text{av}}} = \frac{B\Omega}{\gamma G_{\text{av}}}, \tag{35}$$

where we have assumed $4\xi^2 - 4\xi^4 \cong 4\xi^2$ due to the smallness of ξ, and where we remember that $G_{\text{av}} \cong 30N$ [Belli et al. 2001; Marcheggiani and Lenci 2010].

Expression (35) is the same one obtained in [Lenci and Marcheggiani 2008] with a different model, and agrees with the predictions of the more sophisticated SAMEO model studied in [Marcheggiani and Lenci 2010]. The fact that it is a result of two different models supports its reliability. In fact, in [Lenci and Marcheggiani 2008] it has been shown that it predicts very well experimental results from the literature. Furthermore, based on the results of the London Millennium Bridge, it has been shown that a reasonable value for γ, likely valid in any circumstance, is $\gamma = 0.14\text{–}0.17\,\text{cm}^{-1} = 14\text{–}17\,\text{m}^{-1}$. This means that there is a complete synchronization for $\delta = 1/\gamma = 6\text{–}7$ cm (δ refers to the [Lenci and Marcheggiani 2008] notation), a fact that agrees well with experimental observations [Arup 2000; Dallard et al. 2001a; 2001b]. This value also agrees well with the 4.5 cm identified as the limit lateral displacement in [Nakamura and Kawasaki 2006].

Expression (32) is the generalization of (35) to the case of nonperfect resonance, since, contrarily to (35), it permits the detection, still in a simple way, of the effects of ω_p.

Formula (35) is now extremely simple, since it requires only the knowledge of the real damping and circular frequency of the involved (lateral) mode

$$N_{\text{cr,min}} = 0.0022B\,[\text{kg}\,\text{sec}^{-1}]\,\Omega\,[\text{sec}^{-1}]. \tag{36}$$

In spite of its straightforwardness, it is very predictive. In fact, we remember that the critical number of pedestrians which destabilized the north span of the London Millennium Bridge was about 155 [Dallard et al. 2001a; 2001b]. Since for the north span we have [Strogatz et al. 2005] $M = 113000$ kg, $K = 4730000\,\text{kg}\,\text{sec}^{-2} \rightarrow \Omega = 6.47\,\text{sec}^{-1}$ (that is, the natural frequency is 1.03 Hz), and $B = 11000\,\text{kg}\,\text{sec}^{-1}$, we obtain from (36) $N_{\text{cr,min}} = 156$. Note that the mass of the critical number of pedestrians is about $m = 155 \times 80 = 12480$ kg, that is, 11% of the modal mass.

To further show its reliability, we apply (36) to the Toda Park Bridge, best known as the T-Bridge, a cable-stayed footbridge in Japan. According to [Nakamura and Kawasaki 2006] we have $M = 237000$ kg, $K = 8092000\,\text{kg}\,\text{sec}^{-2} \rightarrow \Omega = 5.84\,\text{sec}^{-1}$ (that is, the natural frequency is 0.93 Hz), and $B = 22200\,\text{kg}\,\text{sec}^{-1}$. Therefore the critical number of synchronizable pedestrians is $N_{\text{cr,min}} = 285$. In this case we do not have the experimental value of N_{cr}, as in the case of the Millennium Bridge, but we know from [Fujino et al. 1993] that with $N \cong 2000$ pedestrians (an extremely congested situation) the bridge experienced synchronized oscillations. Considering that about 20% of pedestrians synchronized, as explicitly remarked in [Fujino et al. 1993], we have $N \cong 400$, which is in good agreement with $N_{\text{cr,min}} = 285$ (we cannot expect equality, since we have data only for a synchronized situation).

In the case of the Maple Valley cable-stay bridge, also known as the M-Bridge, in Japan, we have that the third asymmetric and, to a minor extent, the fourth symmetric modes are involved in the lateral synchronization [Nakamura and Kawasaki 2006; Nakamura and Kawasaki 2009]. For the third mode we have synchronization, for example, when there are about 41 pedestrians on the deck (see [Nakamura and Kawasaki 2009, case M-6, Figure 11]). In this case we have [Nakamura and Kawasaki 2009] M = 97200 kg, K = 29648570 kgsec−2 → = 5.52 sec−1(that is, the natural frequency is 0.88 Hz), and B = 2905 kgsec−1 . Therefore the critical number of synchronizable pedestrians is Ncr,min = 35.

From the previous work we have seen that the main solution curve has a bifurcation point at Ncr. The type of bifurcation depends on the higher-order terms of the Taylor expansion (26):

$$f_\sigma(A_0) = \gamma A_0 + \gamma_2 (A_0)^2 + \gamma_3 (A_0)^3 + \dots, \tag{37}$$

so that from (29) the local behavior of the branching solution is

$$\bar{N}(A_0) = \frac{\omega_p}{\gamma} - \frac{\omega_p \gamma_2}{\gamma^2} A_0 - \frac{\omega_p (\gamma_3 \gamma - \gamma_2^2)}{\gamma^3} (A_0)^2 + \dots. \tag{38}$$

From (38) we see that if γ2 6= 0 we have a transcritical bifurcation. Otherwise, we have a supercritical pitchfork bifurcation if γ3 < 0 or a subcritical pitchfork bifurcation if γ3 > 0 (in this case fσ (A0) has an inflection point, which implies that the pitchfork is preceded by a saddle-node bifurcation for a lower value of N, see Figure 2); this is a consequence of the fact that the trivial solution is stable for N < Ncr. This is obvious by common sense, and can be proved mathematically by noticing that the Jacobian matrix of the map at the rest position is

$$\begin{bmatrix} \alpha_x e^{-\xi T_p} & \alpha_{xy} e^{-\xi T_p} & -\bar{N} \alpha_{xy} e^{-\xi T_p} \\ -\alpha_{xy} e^{-\xi T_p} & \alpha_y e^{-\xi T_p} & \bar{N}(1 - \alpha_y e^{-\xi T_p}) \\ 0 & \dfrac{\gamma}{\omega_p} & 0 \end{bmatrix}, \tag{39}$$

and the associated characteristic equation is (use is made of the property $\alpha_x \alpha_y + \alpha_{xy}^2 = 1$)

$$s^3 - e^{-\xi T_p}(\alpha_x + \alpha_y) s^2 + \left(\frac{\gamma \bar{N}}{\omega_p} (-1 + \alpha_y e^{-\xi T_p}) + e^{-2\xi T_p} \right) s + \frac{\gamma \bar{N} e^{-\xi T_p}}{\omega_p} (-e^{-\xi T_p} + \alpha_x) = 0. \tag{40}$$

In fact, (40) has one solution satisfying s = 1 for N = ωp/γ = Ncr, while below this threshold we have |s| < 1.

The whole bifurcation scenario for different values of γ2 and γ3 is qualitatively depicted in Figure 3.

It is worth remarking that, again, the most interesting properties are determined only by the local behavior of fσ (A0).

Up to now we have considered only the case k = 1, which is the most interesting from a practical point of view because it is the unique case in which the model has a bifurcation point, which describes well, both qualitatively and quantitatively, the real behavior. For the sake of completeness we consider now also

the cases k < 1 and k > 1. Functions with these characteristics are schematically shown in Figure 2.
By referring to Figure 2 the solution scenarios can be easily understood. For k < 1, and supposing that fσ (A0) has regular behavior with an always negative curvature (as the function in Figure 2, see point (3)), we see that, in addition to A0 = 0, for every value of N there is always one and only one solution A0. Furthermore, the function A0 = A0(N) is monotonically increasing and goes to infinity for N → ∞.

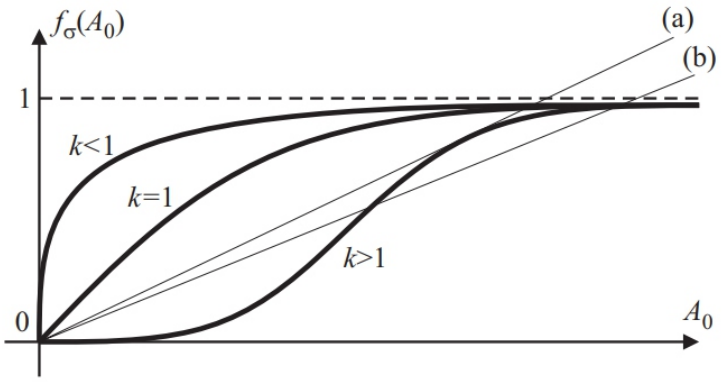

Figure 2. A schematic representation of fσ (A0) for different values of exponent k of (26).

The case k > 1 is slightly more involved. In fact we have that for small values of N (that is, very steep straight lines), there are no solutions. When N increases, at a certain threshold the line becomes tangent to the curve fσ (A0) (as line (a) in Figure 2), at a point ahead of the unique inflection point. Above this threshold there are always two solutions (see line (b) in Figure 2), one of which approaches zero and the other infinity as N → ∞. This is a saddle-node bifurcation, where a solution suddenly appears, far from the main path. This does not seem to capture the behavior observed in real cases, although we cannot exclude in principle that it could happen in different (unobserved up to now) situations. We only note that to detect the saddle-node threshold a local analysis around A0 = 0 is no longer sufficient.

4.2. Imperfect case. In the imperfect case fσ (0) = ε > 0, so that A0 = 0 is no longer a trivial solution. Considering the most interesting case k = 1 we have that

$$\frac{\omega_p}{\bar{N}} A_0 = \varepsilon + \gamma A_0 + \gamma_2 (A_0)^2 + \gamma_3 (A_0)^3 + \dots, \tag{41}$$

so that locally the solution is

$$\frac{\bar{N}}{\omega_p} = \frac{A_0}{\varepsilon} - \gamma \left(\frac{A_0}{\varepsilon}\right)^2 + (-\gamma_2 \varepsilon + \gamma^2)\left(\frac{A_0}{\varepsilon}\right)^3 - (\gamma_3^2 - 2\gamma\gamma_2\varepsilon + \gamma^3)\left(\frac{A_0}{\varepsilon}\right)^4 + \dots. \tag{42}$$

The main branch emanating from (A0, N) = (0, 0) is no longer at rest, although not so far from it, since ε is small — otherwise it cannot be considered as an imperfection and must be carefully considered in an appropriate way. There are no longer branching points and branching paths ensuing from the main one, a

fact that constitutes the main distinction with respect to the perfect case (Section 4.1).

All possible situations are qualitatively depicted in Figure 3, together with the corresponding perfect scenario. Each case of Figure 3 is clearly an unfolding of a local branching bifurcation, according to the fact that transcritical and pitchfork bifurcations are not structurally stable [Wiggins 1997].

Comparing the pictures of Figure 3 with the numerical simulations of the SAMEO model [Marcheg giani and Lenci 2010] and with the experimental outcomes (the results of the Arup tests can be looked up, for example, in [Newland 2001; Abrams 2006]) we see that the situation actually occurring is that of Figure 3c; in fact, for low values of N there are small (but not null) oscillations, which suddenly but not instantaneously (as it would be in the perfect case of a pitchfork bifurcation) increase around a critical threshold.

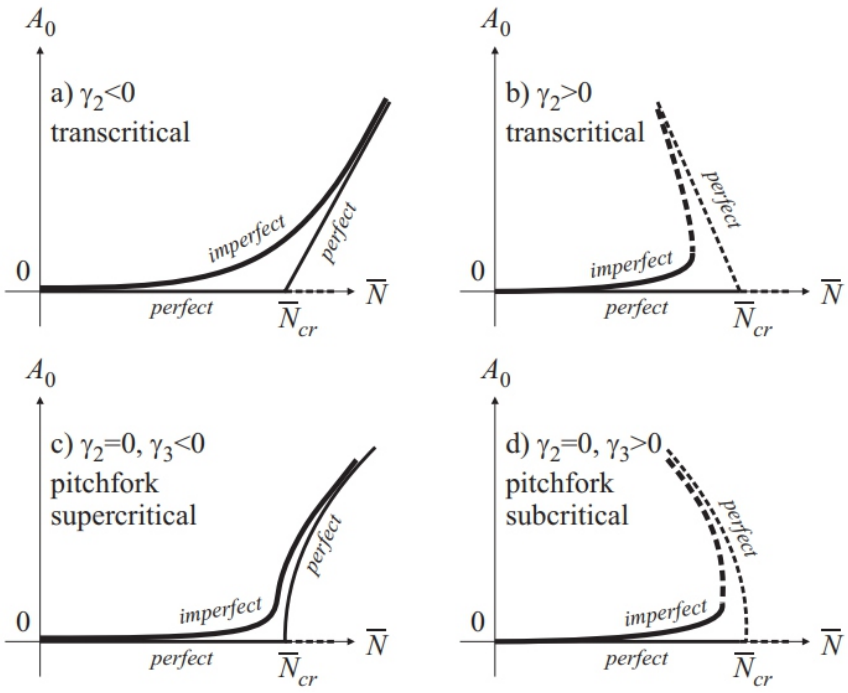

Figure 3. Qualitative bifurcation paths for perfect and imperfect cases; stable (solid lines) and unstable (dashed lines).

From the previous considerations we can draw the following conclusions:

• The theoretical critical value Ncr computed in the previous section is a reference value, of course of great engineering interest, and not the mathematically exact value of the critical threshold, which actually does not exist.

• The dynamical phenomenon underlying the problem of pedestrian-induced lateral vibrations of footbridges is a perturbation of a pitchfork bifurcation. This result was also obtained in [Lenci and Marcheggiani 2008] and is herein confirmed with a different model.

5. The resonant case

We have seen in the previous sections that the resonant case is the worst situation, and thus in this section it is studied in detail.

We start by noticing that the minimum of N_{cr} for varying ω_p is obtained for $\omega_p = \sqrt{1-2\xi^2}$ (see (34)). This is the *mathematical* resonance, corresponding to the maximum of the amplification factor [Clough and Penzien 1975]. The *engineering* resonance is given by $\omega_p = \sqrt{1-\xi^2}$ and corresponds to the coincidence between the external (excitation) and internal (natural) frequencies. When ξ is small, as occurs in practical cases, the difference is negligible.

In the engineering resonance case we have $\alpha_x = \alpha_y = 1$, $\alpha_{xy} = 0$, and the map given by (22) and (25) becomes ($T_p = 2\pi/\sqrt{1-\xi^2}$):

$$x_{n+1} = e^{-\xi T_p} x_n, \quad y_{n+1} = e^{-\xi T_p} y_n + \sigma_n \bar{N}(1 - e^{-\xi T_p}), \quad \sigma_{n+1} = f_\sigma(A_n). \tag{43}$$

From $(43)_1$ we conclude that, for any trajectory, $x_n \to 0$ for $n \to \infty$. This means that the (planar) invariant manifold $x = 0$ is globally attractive, so that the most interesting dynamics live on it. Note that due to $(28)_1$ the fixed points obtained in the previous section belong to the manifold.

On the invariant manifold system (43) reduces to the 2D map

$$y_{n+1} = (1-a) y_n + a\bar{N}\sigma_n, \quad \sigma_{n+1} = f_\sigma\left(\frac{|y_n|}{\omega_p}\right) = f_\sigma\left(\frac{|y_n|}{\sqrt{1-\xi^2}}\right) = \bar{f}_\sigma(|y_n|), \tag{44}$$

where $a = 1 - e^{-\xi T_p} = 1 - e^{-2\pi\xi/\sqrt{1-\xi^2}}$ is a positive number less than 1. In real structures it is possibly small, $a \cong 2\pi\xi$ (and in this case f_σ coincides with $\bar{f}_\sigma$), but this hypothesis is *not* required here.

Given an initial point $P_n = (y_n, \sigma_n)$ in the phase space $(\mathbb{R}, [0, 1])$ of (44), its image $P_{n+1} = (y_{n+1}, \sigma_{n+1})$ can be obtained by the following graphical procedure, which is a noticeable property of map (44) and which is illustrated in Figure 4:

(1) From P_n draw a vertical line and individuate points A and B where it intersects line r of equation $\sigma_n = y_n/\bar{N}$ and the function $\bar{f}_\sigma(|y_n|)$, respectively.

(2) From A draw the line s of slope $1/(a\bar{N})$ (which is more steep than line r since $a < 1$).

(3) From P_n draw a horizontal line and individuate the point C of intersection with s.

(4) From C draw a vertical line and from B a horizontal line. The intersection point is P_{n+1}.

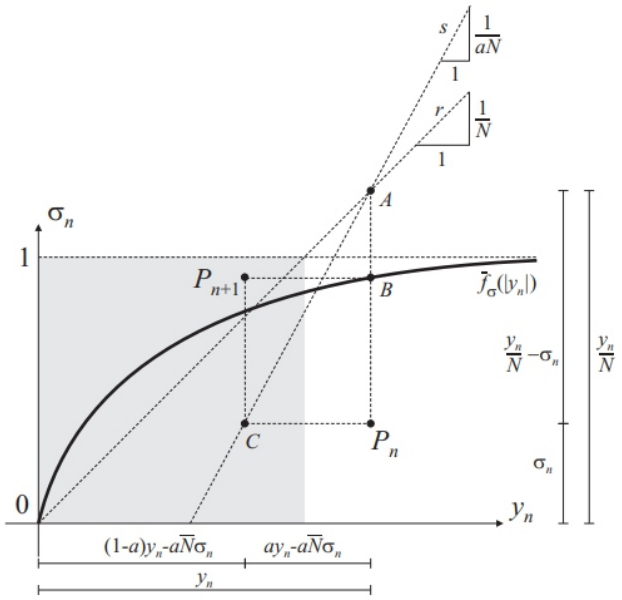

Figure 4. Sketch of the graphical construction of the 2D map (44). In gray is attracting region R = (yn, σn) ∈ ([0, N], [0, 1]).

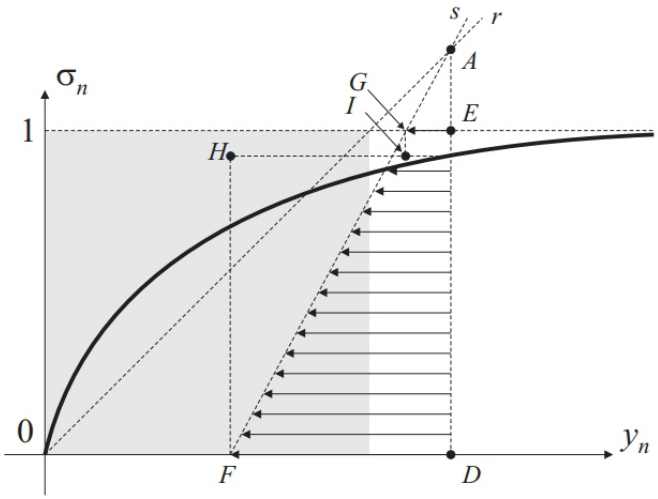

Figure 5. Some properties of the map (44).

From the previous graphical construction it is immediately seen that the unique nontrivial fixed point (when it exists, that is, above $\bar{N}_{cr}$) corresponds to y_0 such that points A and B coincide, that is, when line r intersects $\bar{f}_\sigma(|y_n|)$. This corresponds exactly to the point found by the graphical construction of Figure 1.

By using the graphical construction of Figure 4 it is possible to note the following properties, which are illustrated in Figure 5 and which further help in understanding the behavior of the 2D map:

- segment F-G is the diagram of the horizontal displacements of the points belonging to segment D-E, that is, the points having a fixed y_n and varying σ_n and
- the image of segment D-E is segment H-I.

It is useful to rewrite $(44)_1$ in the alternative form

$$\Delta y_n = y_{n+1} - y_n = a(\bar{N}\sigma_n - y_n). \tag{45}$$

Since $0 \leq \sigma_n \leq 1$, we have that

$$-ay_n \leq \Delta y_n \leq a(\bar{N} - y_n). \tag{46}$$

From the left-hand side inequality we see that for all negative y_n the difference Δy_n is positive, so that every point in the region $y_n < 0$ tends to move toward $y_n = 0$. From the right-hand side inequality, on the other hand, we see that for all $y_n > \bar{N}$ the difference Δy_n is negative, so that every point in the region $y_n > \bar{N}$ tends to move toward $y_n = \bar{N}$ (see an example in Figure 5). The conclusion is that the region $R = (y_n, \sigma_n) \in ([0, \bar{N}], [0, 1])$, which is shown in gray in Figures 4 and 5, is globally attracting, and the steady-state behavior lies therein. In fact, points belonging to R do not escape from it, since from $0 \leq y_n \leq \bar{N}$ and $0 \leq \sigma_n \leq 1$ it follows (see $(44)_1$) that $0 \leq y_{n+1} \leq \bar{N}$.

On the attracting region R the map (44) is *invertible*, because $\bar{f}_\sigma(y_n)$ is invertible on $\mathbb{R}^+$ by the assumptions made in Section 3.

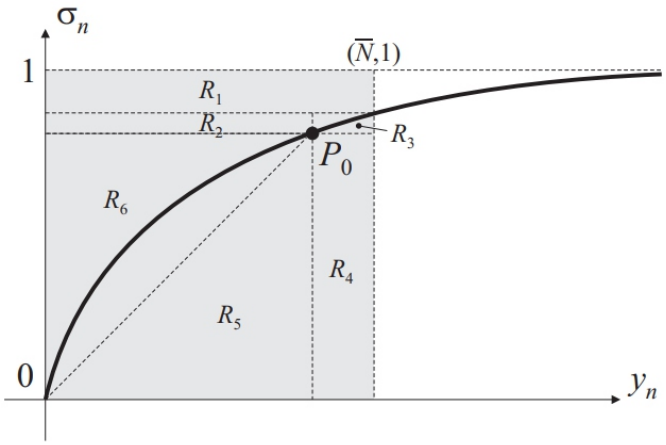

Figure 6. The six subregions of the attracting region of the map (44).

In the case $\bar{N} > \bar{N}_{\text{cr}}$ the region R can be divided into six subregions, as shown in Figure 6. From the graphical constructions introduced above we see that:

- $R_1 \to R_3 \cup R_4 \cup R_5 \cup R_6$;
- $R_2 \to R_4 \cup R_5 \cup R_6$;
- $R_3 \to R_3$;
- $R_4 \to R_2 \cup R_3$;
- $R_5 \to R_6$;
- $R_6 \to R_5 \cup R_6$.

An example is reported in Figure 7 where $\bar{f}_\sigma(y) = \tanh(y)$, $\bar{N} = 1.5$ $(> \bar{N}_{\text{cr}} = 1)$, and $a = 0.3$.

From the previous scheme we conclude that periodic or chaotic solutions (not necessarily stable) are possible only in R_3, alternating in R_2 and R_4, and alternating in R_5 and R_6. These considerations are the starting point for the detailed study of the dynamical behavior of the map (44), which is out of the

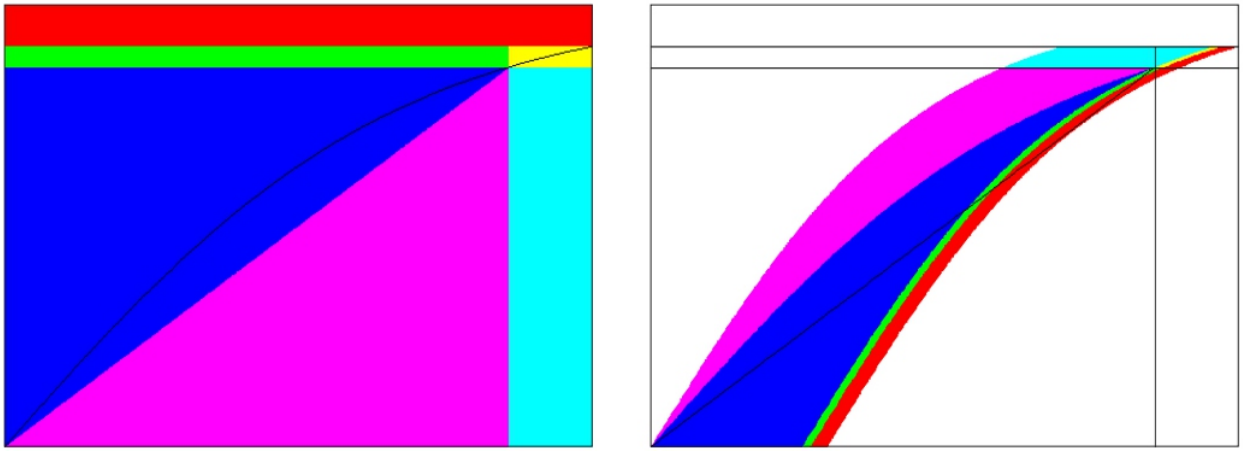

Figure 7. The six subregions of the attracting region and their images after one iteration of the map, where $\bar{f}_\sigma(y) = \tanh(y)$, $\bar{N} = 1.5$ ($> \bar{N}_{cr} = 1$), and $a = 0.3$.

scope of the present paper and is left for future work. We only note that in some isolated numerical simulations based on the example of Figure 7 we have seen that the bifurcated equilibrium point P0 is globally attractive for the whole phase space.

6. Conclusions

A 3D discrete-time dynamical system has been proposed for studying the pedestrian-induced lateral vibrations of footbridges. For the mechanical part, the model is based on the stroboscopic Poincaré map of the flow of the associated continuous time, one mode system, while the coupling between the pedestrians and the bridge motion has been modeled by assuming that the degree of synchronization of the pedestrians is a function fσ of the amplitude of the bridge oscillations.

The fixed points of the map have been studied in detail, without exact knowledge of fσ . Only the local behavior of fσ around the rest position and some qualitative properties have been used. Both the perfect and the imperfect cases have been considered.

In the perfect case it has been shown that in the unique case of interest in practice (corresponding tof0σ(0) = γ ∈]0,∞[) there is a main path of rest solutions. When the number of pedestrians N increases,at a certain threshold Ncr a secondary path bifurcates from the previous one, thus allowing for "large" oscillations of the bridge. This is the threshold of activation of the unwanted lateral oscillations, and it is of primary importance in practice. With the proposed model a very simple, predictive, and general formula is obtained for Ncr, a fact that constitutes the main result of this paper.

The imperfect case has been considered, by including the effect of small imperfections. It has been shown how the four possible fixed-points scenarios are modified by the imperfections. The one corre sponding to a perturbation of a pitchfork bifurcation is noted to agree with experimental observations on real cases (the Arup experiments on the Millennium Bridge) and with numerical simulations of a more

sophisticated model. Thus, it is concluded that the dynamical phenomenon underlying the synchronization problem is a perturbation of the pitchfork bifurcation.

The present paper is devoted to the construction of the model and to the study of the fixed points, which is sufficient to obtain the desired formula for the critical number of pedestrians and to understand the main dynamical aspects. The detailed study of the whole dynamics of the system, including more complex phenomena such as chaos, is worthwhile but out of the scope of this work, and is left for future work.

Acknowledgements

Lenci thanks the Organizing Committee of PACAM XI, and its President Adair Aguiar, for supporting his participation in the Congress. Thanks are also gratefully due to Carlos Mazzilli and Paulo Gonçalves for supporting a post-Congress visit at USP and PUC, during which part of this work has been developed.

References

[Abrams 2006] D. M. Abrams, Two coupled oscillator models: the Millennium Bridge and the Chimera state, Ph.D. thesis,Theoretical and Applied Mechanics, Cornell University, Ithaca, NY, 2006, available at http://hdl.handle.net/1813/3271.

[Arup 2000] Arup Group, "The Millennium Bridge", 2000. http://www.arup.com/MillenniumBridge/indepth/video.html.

[Belli et al. 2001] A. Belli, P. Bui, A. Berger, A. Geyssant, and J.-R. Lacour, "A treadmill ergometer for three-dimensional ground reaction forces measurement during walking", J. Biomech. 34:1 (2001), 105–112.

[Blanchard et al. 1977] J. Blanchard, B. L. Davies, and J. W. Smith, "Design criteria and analysis for dynamic loading of footbridges", pp. 90–107 in Symposium on Dynamic Behaviour of Bridges (Crowthorne, 1977), TRRL Supplementary Report 275, Transport and Road Research Laboratory, Crowthorne, U.K., 1977.

[Blekherman 2007] A. N. Blekherman, "Autoparametric resonance in a pedestrian steel arch bridge: Solferino bridge, Paris", J. Bridge Eng. 12:6 (2007), 669–676.

[Bodgi et al. 2007] J. Bodgi, S. Erlicher, and P. Argoul, "Lateral vibration of footbridges under crowd-loading: continuous crowd modeling approach", Key Eng. Mater. 347 (2007), 685–690.

[Candaten and Rinaldi 2000] M. Candaten and S. Rinaldi, "Peak-to-peak dynamics: a critical survey", Int. J. Bifurc. Chaos 10:8 (2000), 1805–1820.

[Clough and Penzien 1975] R. Clough and J. Penzien, Dynamics of structures, McGraw-Hill, New York, 1975.

[Dallard et al. 2001a] P. Dallard, A. J. Fitzpatrick, A. Flint, S. Le Bourva, A. Low, R. M. R. Smith, and M.

Willford, "The London Millennium Footbridge", Struct. Eng. 79:22 (2001), 17–33.

[Dallard et al. 2001b] P. Dallard, A. J. Fitzpatrick, A. Flint, A. Low, R. M. R. Smith, M. Willford, and M. Roche, "London Millennium Bridge: pedestrian-induced lateral vibration", J. Bridge Eng. 6:6 (2001), 412–417.

[Danbon and Grillaud 2005] F. Danbon and G. Grillaud, "Dynamic behaviour of a steel footbridge: characterization and modelling of the dynamic loading induced by a moving crowd on the Solferino Footbridge in Paris", in Proceedings of Footbridge 2005: 2nd International Conference (Venice, 2005), Office Technique pour l'Utilisation de l'Acier, Puteaux, 2005.

[Eckhardt et al. 2007] B. Eckhardt, E. Ott, S. H. Strogatz, D. M. Abrams, and A. McRobie, "Modeling walker synchronization on the Millennium Bridge", Phys. Rev. E 75:2 (2007), 021110.

[Fujino et al. 1993] Y. Fujino, B. M. Pacheco, S.-I. Nakamura, and P. Warnitchai, "Synchronization of human walking observed during lateral vibration of a congested pedestrian bridge", Earthq. Eng. Struct. Dyn. 22:9 (1993), 741–758.

[Johansson et al. 2008] A. Johansson, D. Helbing, H. Z. Al-Abideen, and S. Al-Bosta, "From crowd dynamics to crowd safety: a video-based analysis", Adv. Complex Syst. 11:4 (2008), 497–527.

[Lenci and Marcheggiani 2008] S. Lenci and L. Marcheggiani, "A discrete-time model for the phenomenon of synchronous lateral excitation due to pedestrians motion on footbridges", in Proceedings of Footbridge 2008: Footbridge for urban renewal: 3rd International Conference (Porto, 2008), edited by E. de Sá Caetano and Á. Cunha, University of Porto, College of Engineering (FEUP), Porto, 2008.

[Marcheggiani and Lenci 2010] L. Marcheggiani and S. Lenci, "On a model for the pedestrians-induced lateral vibrations of footbridges", Meccanica (Milano) 45:4 (2010), 531–551.

[Matsumoto et al. 1978] Y. Matsumoto, T. Nishioka, H. Shiojiri, and K. Matsuzaki, "Dynamic design of footbridges", IABSE Proc. 2 (1978), 1–15. Paper P-17/78.

[Nakamura 2004] S.-I. Nakamura, "Model for lateral excitation of footbridges by synchronous walking", J. Struct. Eng. (ASCE) 130:1 (2004), 32–37.

[Nakamura and Kawasaki 2006] S.-I. Nakamura and T. Kawasaki, "Lateral vibration of footbridges by synchronous walking", J. Constr. Steel Res. 62:11 (2006), 1148–1160.

[Nakamura and Kawasaki 2009] S.-I. Nakamura and T. Kawasaki, "A method for predicting the lateral girder response of footbridges induced by pedestrians", J. Constr. Steel Res. 65:8-9 (2009), 1705–1711.

[Newland 2001] D. E. Newland, "Vibration: problem and solution", pp. 88–93 in Blade of light: the story of London's Millennium Bridge, edited by D. Sudjic, Penguin/Millennium Bridge Trust, London, 2001.

[Newland 2003] D. E. Newland, "Pedestrian excitation of bridges: recent results", pp. 1–15 in Proceedings of the Tenth International Congress on Sound and Vibration (ICSV-10) (Stockholm, 2003),

edited by A. Nilsson and H. Boden, International Institute of Acoustics and Vibration (IIAV), Stockholm, 2003.

[Piccardo and Tubino 2008] G. Piccardo and F. Tubino, "Parametric resonance of flexible footbridges under crowd-induced lateral excitation", J. Sound Vib. 311:1-2 (2008), 353–371.

[Ricciardelli and Pizzimenti 2007] F. Ricciardelli and A. D. Pizzimenti, "Lateral walking-induced forces on footbridges", J.Bridge Eng. 12:6 (2007), 677–688.

[Roberts 2005] T. M. Roberts, "Lateral pedestrian excitation of footbridges", J. Bridge Eng. 10:1 (2005), 107–112.

[Strogatz et al. 2005] S. H. Strogatz, D. M. Abrams, A. McRobie, B. Eckhardt, and E. Ott, "Theoretical mechanics: crowd synchrony on the Millennium Bridge", Nature 438:7064 (2005), 43–44.

[Venuti and Bruno 2009] F. Venuti and L. Bruno, "Crowd-structure interaction in lively footbridges under synchronous lateral excitation: a literature review", Phys. Life Rev. 6:3 (2009), 176–206.

[Venuti et al. 2007] F. Venuti, L. Bruno, and N. Bellomo, "Crowd dynamics on a moving platform: mathematical modelling and application to lively footbridges", Math. Comput. Model. 45:3-4 (2007), 252–269.

[Wheeler 1980] J. E. Wheeler, "Pedestrian induced vibration in footbridges", Technical report 15, Main Roads Department, Perth, 1980.

[Wiggins 1997] S. Wiggins, Introduction to applied nonlinear dynamical systems and chaos, Texts in Applied Mathematics 2, Springer, New York, 1997.

[Živanovic et al. 2005] ´ S. Živanovic, A. Pavic, and P. Reynolds, "Vibration serviceability of footbridges under human-induced ´ excitation: a literature review", J. Sound Vib. 279:1-2 (2005), 1–74.

FREE VIBRATION OF A SIMULATION CANDU NUCLEAR FUEL BUNDLE STRUCTURE INSIDE A TUBE

XUAN ZHANG AND SHUDONG YU

ABSTRACT

This paper presents a numerical rigid-elasto model for vibration of a simulation nuclear fuel structure confined in a circular tube. The model is developed using the finite element method combined with the floating frame formulation. The nonlinear dynamic equations are derived using the Lagrange equations. Small-amplitude vibration about the static equilibrium position is obtained through linearization. Numerical results show that the fundamental mode is a rocking-like mode, in which rigid body translation and rotation are coupled with elastic deformations. Gravity is found to reduce the frequency of the fundamental mode without affecting the higher modes. Experiments are conducted for a single fuel bundle structure to validate the numerical results.

1. Introduction

Horizontally placed CANDU1 fuel bundles in a circular tube are used in the Canadian nuclear industry. During operation, the fuel bundles experience small-amplitude flow-induced vibration, which can result in significant wear to the supporting structures over a period of time.

Static deformations of fuel bundle structures have been investigated in [Cho et al. 2000; Horhoianu and Ionescu 2006]. Dynamic models of a horizontally placed rod bundle sitting on the inner surface of a tube have not been seen before in the literature.

A 43-element simulation fuel bundle is shown in Figure 1 on the next page. The bundle has 43 rods distributed in 3 rings and at the center. The rods are interconnected by two endplates. Each endplate consists of 3 circular rings and 16 ribs/webs. The weight of the bundle is supported by the bearing pads on the bottom rods in the outer ring, as shown on the right. Ideally there are four bearing pads in contact with the tube surface and supporting the bundle weight. The radial gaps between the tube surface and the bearing pads on the rods next to the bottom rods are about 30–50μm, which permits bundle vibration without impacting the supporting structure. This smallamplitude vibration results in a relatively large motion in the top parts of the bundle due to the large bundle diameter. When disturbed or excited, the bundle vibrates about its equilibrium position.

Fuel channel inspections at the Darlington nuclear station indicated that bundle vibrations, for example, rocking, induced by the coolant flow were responsible for the fretting between the pressure tube spacer sleeve and the inlet bundle bearing pads [Judah 1992]. Modeling the bundle vibration requires formulation of the rigid-elastic motions of a 3D bundle structure. The superimposition method [Schwab and Meijaard 2002] and the floating frame formulation [Shabana 2005] have been used to deal with rigid and elastic motions of a 3D body.

Extending from [Zhang and Yu 2010a], this paper presents a numerical procedure for modeling the rod bundles using the floating frame formulation. A rigid-elastodynamic model is established and applied to the study of the fundamental mode of a single bundle. The influence of gravity is discussed based on the simulation results. The simulation results are compared to experimental results.

2. Finite element model in the floating frame formulation

The floating frame formulation used in multibody dynamics is employed to couple the rigid body motion and the elastic deformation of the bundle. Nonlinear equations of motion are obtained for the bundle vibration, and then simplified to a set of linear equations for the small-amplitude vibrations about the equilibrium.

As shown in Figure 1, left, a global inertia frame is chosen in such a way that the X-axis is horizontal and the Y -axis is vertical. The origin of the global frame is chosen to be the center of the upstream endplate. To describe the rigid body motion, a reference frame x-y-z is also defined in the figure. The frame is rigidly attached to the mass center of the bundle so that it moves and rotates with the bundle.

This frame is regarded as the body frame of the bundle.

The bundle is discretized using two types of finite elements. The rods are modeled using a three-node higher-order beam element in conjunction with Euler–Bernoulli theory [Meirovitch 2001]. The endplates are modeled using a special nine-node isoparametric plate element [Yu and Wen 2007] in conjunction with the third-order thick plate theory of [Reddy 1984]. The finite element model is shown in Figure 1, right. The endplate is regarded as massless because its mass is significantly smaller than the mass of the rods. Therefore the stiffness of the endplate can be condensed using static substructuring. A superelement can then be achieved for each endplate using the procedures described in [Zhang and Yu 2010b].

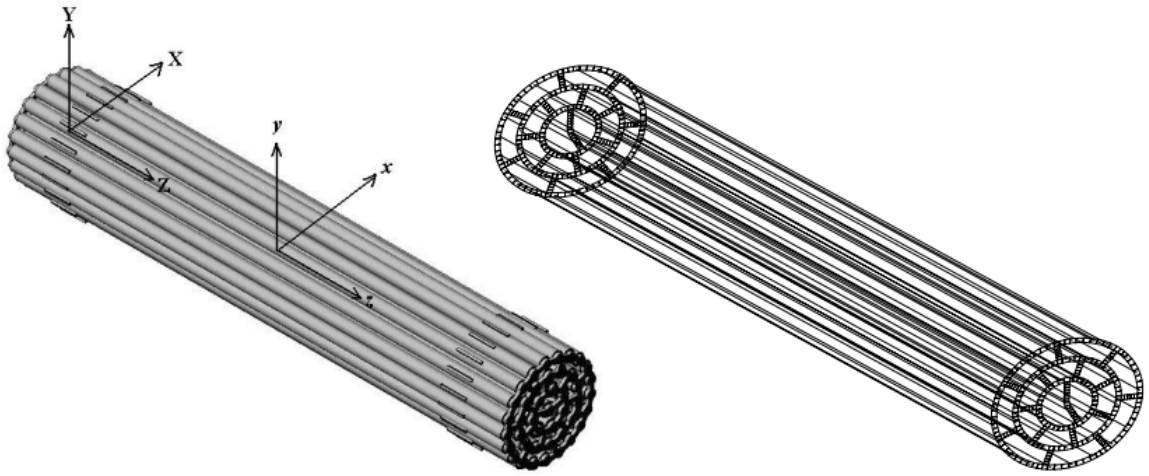

Figure 1. Rod bundle: isoparametric view (left) and finite-element mesh (right).

Two sets of degrees of freedom (DOFs) are considered in this model. The first set is the rigid body (body frame) displacement including translations uc and rotations φ measured in the global frame X-Y -Z. The second set is the deformation-induced displacement u f measured in the body frame. In the floating frame formulation [Shabana 2005], the displacement of an arbitrary material point on the bundle can be expressed as

$$\boldsymbol{u} = \boldsymbol{u}_c + [\boldsymbol{A}(\boldsymbol{\phi}) - \boldsymbol{A}_0]\boldsymbol{x} + \boldsymbol{A}(\boldsymbol{\phi})\boldsymbol{u}_f,$$

where $\boldsymbol{A}(\boldsymbol{\phi}) = \boldsymbol{A}_3\boldsymbol{A}_2\boldsymbol{A}_1$ is the Euler rotation matrix,

$$\boldsymbol{A}_3 = \begin{bmatrix} \cos\varphi_3 & -\sin\varphi_3 & 0 \\ \sin\varphi_3 & \cos\varphi_3 & 0 \\ 0 & 0 & 1 \end{bmatrix}, \quad \boldsymbol{A}_2 = \begin{bmatrix} \cos\varphi_2 & 0 & \sin\varphi_2 \\ 0 & 1 & 0 \\ -\sin\varphi_2 & 0 & \cos\varphi_2 \end{bmatrix}, \quad \boldsymbol{A}_1 = \begin{bmatrix} 1 & 0 & 0 \\ 0 & \cos\varphi_1 & -\sin\varphi_1 \\ 0 & \sin\varphi_1 & \cos\varphi_1 \end{bmatrix}.$$

φ_1, φ_2, and φ_3 are three Euler angles. $\boldsymbol{A}^0$ is the initial value of $\boldsymbol{A}$ and is equal to the identity matrix $\boldsymbol{I}$; $\boldsymbol{u}_f$ can be further expressed in terms of the finite element nodal displacement $\bar{\boldsymbol{u}}_f$ as

$$\boldsymbol{u}_f = \boldsymbol{t}^T\boldsymbol{N}(x)\boldsymbol{T}\bar{\boldsymbol{u}}_f,$$

where $\boldsymbol{N}(x)$ is the shape function of the beam element, while $\boldsymbol{t}$ and $\boldsymbol{T}$ are the transformation matrices between the element local frame and the body frame coordinates for the material point and the nodal DOFs, respectively. Vector $\boldsymbol{x}$ is the distance vector from the body frame origin to the material point measured in the body frame. Vector $\boldsymbol{x}$ can be expressed as $\boldsymbol{x} = \boldsymbol{x}_E^{(b)} + \boldsymbol{t}^T\boldsymbol{x}^{(e)}$, where $\boldsymbol{x}_E^{(b)}$ is the distance vector from the body frame origin to the element local frame origin measured in the body frame and $\boldsymbol{x}^{(e)}$ is the distance vector from the element local frame origin to the material point measured in the element local frame.

The velocity of the arbitrary material point is

$$\dot{\boldsymbol{u}} = \dot{\boldsymbol{u}}_c + \dot{\boldsymbol{A}}(\boldsymbol{x} + \boldsymbol{u}_f) + \boldsymbol{A}\dot{\boldsymbol{u}}_f = \begin{bmatrix} \boldsymbol{L}_r & \tilde{\boldsymbol{L}}_f \end{bmatrix} \begin{Bmatrix} \dot{\boldsymbol{u}}_r \\ \dot{\bar{\boldsymbol{u}}}_f \end{Bmatrix} = \boldsymbol{L}\dot{\boldsymbol{q}},$$

where

$$\boldsymbol{q} = \left\{\boldsymbol{u}_r^T \;\; \bar{\boldsymbol{u}}_f^T\right\}^T, \quad \boldsymbol{u}_r = \left\{\boldsymbol{u}_c^T \;\; \boldsymbol{\phi}^T\right\}^T, \quad \boldsymbol{L}_r = \begin{bmatrix} \boldsymbol{I} & \boldsymbol{B} \end{bmatrix}, \quad \tilde{\boldsymbol{L}}_f = [\tilde{\boldsymbol{A}}] = [\boldsymbol{A}\boldsymbol{t}^T\boldsymbol{N}(x)\boldsymbol{T}\bar{\boldsymbol{u}}_f],$$

$$\boldsymbol{B} = \left[\boldsymbol{A}_3\boldsymbol{A}_2\frac{\partial \boldsymbol{A}_1}{\partial \varphi_1}\boldsymbol{u}^* \;\; \boldsymbol{A}_3\frac{\partial \boldsymbol{A}_2}{\partial \varphi_2}\boldsymbol{A}_1\boldsymbol{u}^* \;\; \frac{\partial \boldsymbol{A}_3}{\partial \varphi_3}\boldsymbol{A}_2\boldsymbol{A}_1\boldsymbol{u}^*\right] = \boldsymbol{B}(\varphi, \boldsymbol{u}^*),$$

$$\boldsymbol{u}^* = \boldsymbol{x} + \boldsymbol{u}_f = \boldsymbol{x} + \boldsymbol{t}^T\boldsymbol{N}(x)\boldsymbol{T}\bar{\boldsymbol{u}}_f.$$

The kinetic energy of the system can then be expressed as

$$T = \int_V \frac{1}{2}\rho\dot{\boldsymbol{u}}^T\dot{\boldsymbol{u}}\,dV = \frac{1}{2}\begin{Bmatrix} \dot{\boldsymbol{u}}_r \\ \dot{\bar{\boldsymbol{u}}}_f \end{Bmatrix}^T \begin{bmatrix} \boldsymbol{M}_{rr} & \boldsymbol{M}_{rf} \\ \boldsymbol{M}_{fr} & \boldsymbol{M}_{ff} \end{bmatrix} \begin{Bmatrix} \dot{\boldsymbol{u}}_r \\ \dot{\bar{\boldsymbol{u}}}_f \end{Bmatrix} = \frac{1}{2}\dot{\boldsymbol{q}}^T\boldsymbol{M}\dot{\boldsymbol{q}}, \tag{1}$$

where

$$\boldsymbol{M}_{rr} = \int_V \rho\boldsymbol{L}_r^T\boldsymbol{L}_r\,dV, \quad \boldsymbol{M}_{rf} = \int_V \rho\boldsymbol{L}_r^T\tilde{\boldsymbol{L}}_f\,dV, \quad \boldsymbol{M}_{fr} = \int_V \rho\tilde{\boldsymbol{L}}_f^T\boldsymbol{L}_r\,dV, \quad \boldsymbol{M}_{ff} = \int_V \rho\tilde{\boldsymbol{L}}_f^T\tilde{\boldsymbol{L}}_f\,dV.$$

The potential energy of the system is simply the summation of the elastic potential energy Ve and the gravity potential energy Vg:

$$V = V_e + V_g, \quad V_e = \frac{1}{2}\begin{Bmatrix} \boldsymbol{u}_r \\ \bar{\boldsymbol{u}}_f \end{Bmatrix}^T \begin{bmatrix} \boldsymbol{0} & \boldsymbol{0} \\ \boldsymbol{0} & \boldsymbol{K}_{ff} \end{bmatrix} \begin{Bmatrix} \boldsymbol{u}_r \\ \bar{\boldsymbol{u}}_f \end{Bmatrix} = \frac{1}{2}\boldsymbol{q}^T \boldsymbol{K} \boldsymbol{q}, \quad V_g = \int_V \rho g \begin{bmatrix} 0 & 1 & 0 \end{bmatrix} \boldsymbol{r}\, dV, \tag{2}$$

where $\boldsymbol{K}_{ff}$ is the stiffness matrix obtained using the finite element method for the bundle and $\boldsymbol{r}$ is the distance vector from the global origin to the arbitrary material point.

The bundle is assumed to be constrained at the four bearing pad locations. The bundle cannot move due to the large weight and the frictional force between the bundle and the hosting tube. It is justified to consider the nodes as simply supported at the four bearing pad locations when small oscillatory motion is studied. Therefore, the following constraint conditions apply:

$$\boldsymbol{u}^{(i)} = \boldsymbol{u}_c + [\boldsymbol{A}(\boldsymbol{\phi}) - \boldsymbol{A}^0]\boldsymbol{x}^{(i)} + \boldsymbol{A}(\boldsymbol{\phi})\bar{\boldsymbol{u}}_f^{(i)} = \boldsymbol{0}, \tag{3}$$

where superscript (i) represents the i-th constrained node ($i = 1, \ldots, 4$).

According to the free and constrained DOFs, (1) and (2) can be partitioned

$$T = \frac{1}{2}\begin{Bmatrix} \dot{\boldsymbol{u}}_r \\ \dot{\bar{\boldsymbol{u}}}_{fc} \\ \dot{\bar{\boldsymbol{u}}}_{fi} \end{Bmatrix}^T \begin{bmatrix} \boldsymbol{M}_{11} & \boldsymbol{M}_{12} & \boldsymbol{M}_{13} \\ \boldsymbol{M}_{21} & \boldsymbol{M}_{22} & \boldsymbol{M}_{23} \\ \boldsymbol{M}_{31} & \boldsymbol{M}_{32} & \boldsymbol{M}_{33} \end{bmatrix} \begin{Bmatrix} \dot{\boldsymbol{u}}_r \\ \dot{\bar{\boldsymbol{u}}}_{fc} \\ \dot{\bar{\boldsymbol{u}}}_{fi} \end{Bmatrix}, \quad V_e = \frac{1}{2}\begin{Bmatrix} \boldsymbol{u}_r \\ \bar{\boldsymbol{u}}_{fc} \\ \bar{\boldsymbol{u}}_{fi} \end{Bmatrix}^T \begin{bmatrix} \boldsymbol{K}_{11} & \boldsymbol{K}_{12} & \boldsymbol{K}_{13} \\ \boldsymbol{K}_{21} & \boldsymbol{K}_{22} & \boldsymbol{K}_{23} \\ \boldsymbol{K}_{31} & \boldsymbol{K}_{32} & \boldsymbol{K}_{33} \end{bmatrix} \begin{Bmatrix} \boldsymbol{u}_r \\ \bar{\boldsymbol{u}}_{fc} \\ \bar{\boldsymbol{u}}_{fi} \end{Bmatrix}, \tag{4}$$

where $\bar{\boldsymbol{u}}_{fc} = \left\{\bar{\boldsymbol{u}}_f^{(1)^T} \;\; \bar{\boldsymbol{u}}_f^{(2)^T} \;\; \bar{\boldsymbol{u}}_f^{(3)^T} \;\; \bar{\boldsymbol{u}}_f^{(4)^T}\right\}^T$ represents the DOFs corresponding to the constrained nodes and $\bar{\boldsymbol{u}}_{fi}$ represents the unconstrained DOFs.

From (3), $\bar{\boldsymbol{u}}_{fc}$ can be expressed in terms of $\boldsymbol{u}_r$. The independent DOFs become $\tilde{\boldsymbol{q}} = \{\boldsymbol{u}_r^T \;\; \bar{\boldsymbol{u}}_{fi}^T\}^T$. Substituting into (4), the kinetic energy and elastic potential energy become

$$\begin{aligned} T &= \frac{1}{2}\dot{\tilde{\boldsymbol{q}}}^T \begin{bmatrix} \boldsymbol{M}_{11} & \boldsymbol{M}_{13} \\ \boldsymbol{M}_{31} & \boldsymbol{M}_{33} \end{bmatrix} \dot{\tilde{\boldsymbol{q}}} + \bar{T}(\dot{\tilde{\boldsymbol{q}}}, \tilde{\boldsymbol{q}}) = \frac{1}{2}\dot{\tilde{\boldsymbol{q}}}^T \boldsymbol{M}_s \dot{\tilde{\boldsymbol{q}}} + \bar{T}(\dot{\tilde{\boldsymbol{q}}}, \tilde{\boldsymbol{q}}), \\ V_e &= \frac{1}{2}\tilde{\boldsymbol{q}}^T \begin{bmatrix} \boldsymbol{K}_{11} & \boldsymbol{K}_{13} \\ \boldsymbol{K}_{31} & \boldsymbol{K}_{33} \end{bmatrix} \tilde{\boldsymbol{q}} + \bar{V}_e(\tilde{\boldsymbol{q}}) = \frac{1}{2}\tilde{\boldsymbol{q}}^T \boldsymbol{K}_s \tilde{\boldsymbol{q}} + \bar{V}_e(\tilde{\boldsymbol{q}}), \end{aligned} \tag{5}$$

where

$$\begin{aligned} \bar{T}(\dot{\tilde{\boldsymbol{q}}}, \tilde{\boldsymbol{q}}) &= \tfrac{1}{2}(\dot{\boldsymbol{u}}_r^T \boldsymbol{M}_{12}\dot{\bar{\boldsymbol{u}}}_{fc} + \dot{\bar{\boldsymbol{u}}}_{fc}^T \boldsymbol{M}_{21}\dot{\boldsymbol{u}}_r + \dot{\bar{\boldsymbol{u}}}_{fi}^T \boldsymbol{M}_{32}\dot{\bar{\boldsymbol{u}}}_{fc} + \dot{\bar{\boldsymbol{u}}}_{fc}^T \boldsymbol{M}_{23}\dot{\boldsymbol{u}}_r + \dot{\bar{\boldsymbol{u}}}_{fc}^T \boldsymbol{M}_{22}\dot{\bar{\boldsymbol{u}}}_{fc}), \\ \bar{V}_e(\tilde{\boldsymbol{q}}) &= \tfrac{1}{2}(\boldsymbol{u}_r^T \boldsymbol{K}_{12}\bar{\boldsymbol{u}}_{fc} + \bar{\boldsymbol{u}}_{fc}^T \boldsymbol{K}_{21}\boldsymbol{u}_r + \bar{\boldsymbol{u}}_{fi}^T \boldsymbol{K}_{32}\bar{\boldsymbol{u}}_{fc} + \bar{\boldsymbol{u}}_{fc}^T \boldsymbol{K}_{23}\boldsymbol{u}_r + \bar{\boldsymbol{u}}_{fc}^T \boldsymbol{K}_{22}\bar{\boldsymbol{u}}_{fc}). \end{aligned}$$

Gravity potential can also be expressed as a composite function of $\tilde{\boldsymbol{q}}$:

$$V_g = V_g[\boldsymbol{u}_r, \bar{\boldsymbol{u}}_{fc}(\boldsymbol{u}_r), \bar{\boldsymbol{u}}_{fi}] = V_g(\tilde{\boldsymbol{q}}).$$

Assuming no nonconservative load, the equations of motion of the system can be obtained using the Lagrange equations [Meirovitch 2001]:

$$\frac{d}{dt}\left(\frac{\partial T}{\partial \dot{\tilde{\boldsymbol{q}}}}\right)^T - \left(\frac{\partial T}{\partial \tilde{\boldsymbol{q}}}\right)^T + \left(\frac{\partial V_e}{\partial \tilde{\boldsymbol{q}}}\right)^T + \left(\frac{\partial V_g}{\partial \tilde{\boldsymbol{q}}}\right)^T = \boldsymbol{0}. \tag{6}$$

Substituting (2)–(4) into (6), notice that $\boldsymbol{M}_s$ depends on $\tilde{\boldsymbol{q}}$ while $\boldsymbol{K}_s$ is a constant. The equations of motion become

$$\boldsymbol{M}_s\ddot{\tilde{\boldsymbol{q}}} + \dot{\boldsymbol{M}}_s\dot{\tilde{\boldsymbol{q}}} + \frac{d}{dt}\left(\frac{\partial \bar{T}}{\partial \dot{\tilde{\boldsymbol{q}}}}\right) - \frac{\partial}{\partial \tilde{\boldsymbol{q}}}(\tfrac{1}{2}\dot{\tilde{\boldsymbol{q}}}\boldsymbol{M}_s\dot{\tilde{\boldsymbol{q}}})^T - \frac{\partial \bar{T}}{\partial \tilde{\boldsymbol{q}}} + \boldsymbol{K}_s\tilde{\boldsymbol{q}} + \boldsymbol{R}(\tilde{\boldsymbol{q}}) + \boldsymbol{H}(\tilde{\boldsymbol{q}}) = \boldsymbol{0},$$

where $\boldsymbol{R}$ represents the nonlinear term from the derivative of the elastic potential energy and $\boldsymbol{H}$ represents the force and moment induced by gravity:

$$\boldsymbol{R}(\tilde{\boldsymbol{q}}) = \frac{\partial \bar{V}_e}{\partial \tilde{\boldsymbol{q}}} = \begin{bmatrix} \boldsymbol{K}_{12}\bar{\boldsymbol{u}}_{fc} + \left(\frac{\partial \bar{\boldsymbol{u}}_{fc}}{\partial \boldsymbol{u}_r}\right)^T \boldsymbol{K}_{21}\boldsymbol{u}_r + \left(\frac{\partial \bar{\boldsymbol{u}}_{fc}}{\partial \boldsymbol{u}_r}\right)^T \boldsymbol{K}_{23}\bar{\boldsymbol{u}}_{fi} + \left(\frac{\partial \bar{\boldsymbol{u}}_{fc}}{\partial \boldsymbol{u}_r}\right)^T \boldsymbol{K}_{22}\bar{\boldsymbol{u}}_{fc} \\ \boldsymbol{K}_{32}\bar{\boldsymbol{u}}_{fc} \end{bmatrix} = \begin{bmatrix} \boldsymbol{R}_r \\ \boldsymbol{R}_{fi} \end{bmatrix},$$

$$\boldsymbol{H}(\tilde{\boldsymbol{q}}) = \frac{\partial V_g}{\partial \tilde{\boldsymbol{q}}} = \left\{ \left(\frac{\partial V_g}{\partial \boldsymbol{u}_r} + \frac{\partial V_g}{\partial \bar{\boldsymbol{u}}_{fc}} \frac{\partial \bar{\boldsymbol{u}}_{fc}}{\partial \boldsymbol{u}_r}\right)^T, \left(\frac{\partial V_g}{\partial \bar{\boldsymbol{u}}_{fi}}\right)^T \right\}^T,$$

where

$$\frac{\partial V_g}{\partial \boldsymbol{u}_r} = \int_V \rho g \begin{bmatrix} 0 & 1 & 0 \end{bmatrix} \begin{bmatrix} \boldsymbol{I} & \boldsymbol{B} \end{bmatrix} dV, \quad \frac{\partial V_g}{\partial \bar{\boldsymbol{u}}_{fc}} = \int_V \rho g \begin{bmatrix} 0 & 1 & 0 \end{bmatrix} \begin{bmatrix} \tilde{\tilde{\boldsymbol{A}}} \end{bmatrix} dV,$$

and $\tilde{\tilde{\boldsymbol{A}}}$ is a fraction of $\tilde{\boldsymbol{A}}$ which corresponds to the constraint DOFs $\boldsymbol{u}_{fc}$. From (3), it can be obtained that

$$\frac{\partial \bar{\boldsymbol{u}}_{fc}}{\partial \boldsymbol{u}_r} = -\boldsymbol{A}^{-1} \begin{bmatrix} \boldsymbol{I} & \boldsymbol{B}(\boldsymbol{u}_c^*) \end{bmatrix},$$

where $\boldsymbol{u}_c^* = \boldsymbol{x} + \bar{\boldsymbol{u}}_{fc}(\tilde{\boldsymbol{q}})$.

The damping effect caused by the velocity terms is not within the scope of this paper. Ignoring the velocity terms $\dot{\boldsymbol{M}}_s\dot{\tilde{\boldsymbol{q}}}$, $(\partial/\partial\tilde{\boldsymbol{q}})\left(\frac{1}{2}\dot{\tilde{\boldsymbol{q}}}\boldsymbol{M}_s\dot{\tilde{\boldsymbol{q}}}\right)$, $\partial\bar{T}/\partial\tilde{\boldsymbol{q}}$, and those in $(d/dt)(\partial\bar{T}/\partial\dot{\tilde{\boldsymbol{q}}})$, the governing equations become

$$\boldsymbol{M}_s\ddot{\tilde{\boldsymbol{q}}} + \boldsymbol{K}_s\tilde{\boldsymbol{q}} + \boldsymbol{S}(\ddot{\tilde{\boldsymbol{q}}}, \tilde{\boldsymbol{q}}) + \boldsymbol{R}(\tilde{\boldsymbol{q}}) + \boldsymbol{H}(\tilde{\boldsymbol{q}}) = \boldsymbol{0}, \tag{7}$$

where

$$\boldsymbol{S}(\ddot{\tilde{\boldsymbol{q}}}, \tilde{\boldsymbol{q}}) = \begin{bmatrix} \boldsymbol{M}_{12}\ddot{\bar{\boldsymbol{u}}}_{fc} + \left(\frac{\partial \bar{\boldsymbol{u}}_{fc}}{\partial \boldsymbol{u}_r}\right)^T \boldsymbol{M}_{21}\ddot{\boldsymbol{u}}_r + \left(\frac{\partial \boldsymbol{u}_{fc}}{\partial \boldsymbol{u}_r}\right)^T \boldsymbol{M}_{23}\ddot{\bar{\boldsymbol{u}}}_{fi} + \left(\frac{\partial \bar{\boldsymbol{u}}_{fc}}{\partial \boldsymbol{u}_r}\right)^T \boldsymbol{M}_{22}\ddot{\bar{\boldsymbol{u}}}_{fc} \\ \boldsymbol{M}_{32}\ddot{\bar{\boldsymbol{u}}}_{fc} \end{bmatrix} = \begin{bmatrix} \boldsymbol{S}_r \\ \boldsymbol{S}_{fi} \end{bmatrix}.$$

If the dynamic terms in (7) are dropped, a static equilibrium solution of the system q˜0 can be obtained through iteration. A Fortran90 code is implemented to solve for the equilibrium solution. For a convergence criterion of 0.001 for the L2 norm of the displacement vector, it takes two steps to reach the converged equilibrium solution. Figure 2 shows the scaled global deformation of the bundle at three different locations for the equilibrium solution.

Denoting $\boldsymbol{\delta}$ as the deviation from the equilibrium position, the generalized coordinates can be expressed as $\tilde{\boldsymbol{q}} = \tilde{\boldsymbol{q}}^0 + \boldsymbol{\delta}$. Substituting this equation into (7), dropping the constant terms and linearizing the nonlinear terms with a Taylor expansion at $\tilde{\boldsymbol{q}}^0$, the governing equation for oscillation about the equilibrium can be obtained as

$$\boldsymbol{M}_s\ddot{\boldsymbol{\delta}} + \boldsymbol{S}(\ddot{\boldsymbol{\delta}}, \tilde{\boldsymbol{q}}^0) + \left(\boldsymbol{K}_s + \frac{\partial \boldsymbol{R}}{\partial \tilde{\boldsymbol{q}}}(\tilde{\boldsymbol{q}}^0) + \frac{\partial \boldsymbol{H}}{\partial \tilde{\boldsymbol{q}}}(\tilde{\boldsymbol{q}}^0)\right)\boldsymbol{\delta} = \boldsymbol{0}. \tag{8}$$

The term $\boldsymbol{S}(\ddot{\boldsymbol{\delta}}, \tilde{\boldsymbol{q}}^0)$ can be further linearized using the Taylor expansion at $\ddot{\boldsymbol{\delta}} = \boldsymbol{0}$, and (8) becomes

$$\left(\boldsymbol{M}_s + \frac{\partial \boldsymbol{S}}{\partial \ddot{\boldsymbol{\delta}}}(\boldsymbol{0}, \tilde{\boldsymbol{q}}^0)\right)\ddot{\boldsymbol{\delta}} + \left(\boldsymbol{K}_s + \frac{\partial \boldsymbol{R}}{\partial \tilde{\boldsymbol{q}}}(\tilde{\boldsymbol{q}}^0) + \frac{\partial \boldsymbol{H}}{\partial \tilde{\boldsymbol{q}}}(\tilde{\boldsymbol{q}}^0)\right)\boldsymbol{\delta} = \boldsymbol{0}, \tag{9}$$

where

$$\frac{\partial \boldsymbol{S}}{\partial \ddot{\boldsymbol{\delta}}}(\boldsymbol{0}, \tilde{\boldsymbol{q}}^0) = \begin{bmatrix} \dfrac{\partial \boldsymbol{S}_r}{\partial \ddot{\boldsymbol{u}}_r} & \left(\dfrac{\partial \ddot{\bar{\boldsymbol{u}}}_{fc}}{\partial \ddot{\boldsymbol{u}}_r}\right)^T \boldsymbol{M}_{23} \\ \boldsymbol{M}_{32}\left(\dfrac{\partial \ddot{\bar{\boldsymbol{u}}}_{fc}}{\partial \ddot{\boldsymbol{u}}_r}\right) & \boldsymbol{0} \end{bmatrix}_{\substack{\ddot{\boldsymbol{\delta}}=\boldsymbol{0} \\ \tilde{\boldsymbol{q}}=\tilde{\boldsymbol{q}}^0}}, \quad \frac{\partial \boldsymbol{R}}{\partial \tilde{\boldsymbol{q}}}(\tilde{\boldsymbol{q}}^0) = \begin{bmatrix} \dfrac{\partial \boldsymbol{R}_r}{\partial \boldsymbol{u}_r} & \left(\dfrac{\partial \bar{\boldsymbol{u}}_{fc}}{\partial \boldsymbol{u}_r}\right)^T \boldsymbol{K}_{23} \\ \boldsymbol{K}_{32}\left(\dfrac{\partial \bar{\boldsymbol{u}}_{fc}}{\partial \boldsymbol{u}_r}\right) & \boldsymbol{0} \end{bmatrix}_{\tilde{\boldsymbol{q}}=\tilde{\boldsymbol{q}}^0},$$

$$\frac{\partial \ddot{\boldsymbol{u}}_{fc}}{\partial \ddot{\boldsymbol{u}}_r} \doteq \begin{bmatrix} -\boldsymbol{A}^{-1} - \boldsymbol{A}^{-1}\boldsymbol{B}(\varphi, \boldsymbol{u}^{(1)}) \\ \vdots \\ -\boldsymbol{A}^{-1} - \boldsymbol{A}^{-1}\boldsymbol{B}(\varphi, \boldsymbol{u}^{(4)}) \end{bmatrix}, \quad \frac{\partial \boldsymbol{u}_{fc}}{\partial \boldsymbol{u}_r} \doteq \begin{bmatrix} -\boldsymbol{A}^{-1} - \boldsymbol{A}^{-1}\boldsymbol{B}(\varphi, \boldsymbol{u}^{*(1)}) \\ \vdots \\ -\boldsymbol{A}^{-1} - \boldsymbol{A}^{-1}\boldsymbol{B}(\varphi, \boldsymbol{u}^{*(4)}) \end{bmatrix},$$

$$\frac{\partial \boldsymbol{H}}{\partial \tilde{\boldsymbol{q}}} = \sum_{i=1}^{Ne} \int_{V_i} \begin{bmatrix} \boldsymbol{0} & \boldsymbol{0} & \boldsymbol{0} \\ \boldsymbol{0} & \dfrac{\partial \boldsymbol{B}_{2,:}}{\partial \boldsymbol{\phi}} & \dfrac{\partial \boldsymbol{B}_{2,:}}{\partial \boldsymbol{u}_f} \\ \boldsymbol{0} & \dfrac{\partial \tilde{\boldsymbol{A}}_{2,:}}{\partial \boldsymbol{\phi}} & \boldsymbol{0} \end{bmatrix}_{\tilde{\boldsymbol{q}}=\tilde{\boldsymbol{q}}^0} dV,$$

and where the subscript (2, :) represents the second row of the matrix. $\dfrac{\partial \boldsymbol{S}_r}{\partial \ddot{\boldsymbol{u}}_r}$ and $\dfrac{\partial \boldsymbol{R}_r}{\partial \boldsymbol{u}_r}$ are 6×6 matrices.

3. Numerical solutions and discussion

A numerical solution to the governing equations of motion, (9), is sought. The geometry and material properties of the bundle are listed in Table 1. The numerical solution shows that the fundamental natural frequency is 6.1 Hz. After normalizing the eigenvector, it is found that the Z-direction rigid body rotation is the primary dominant component and the X-direction rigid body translation is the secondary. The

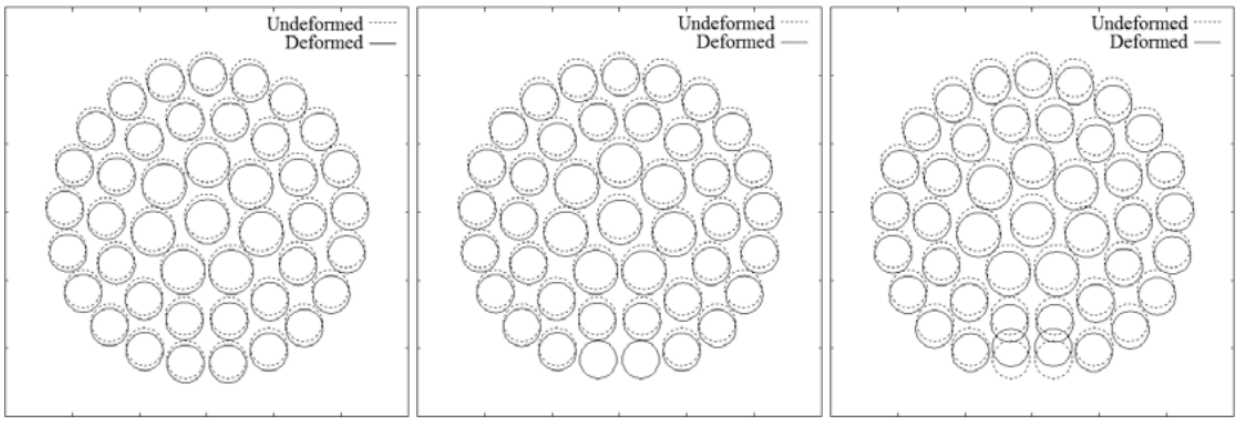

Figure 2. Scaled deformation in equilibrium at different locations: bundle ends (left),bearing pads (middle), and midspan (right).

Parameter	Symbol	Value
Bundle length (mm)	L	500.0
Outer ring mean radius (mm)	R_1	42.5
Intermediate ring mean radius (mm)	R_2	30.0
Inner ring mean radius (mm)	R_3	16.5
Ring and rib width (mm)	b	3.4
Endplate thickness (mm)	t	3.0
Young's modulus (GPa)	E	200.0
Poisson's ratio	ν	0.3
Shear modulus (GPa)	G	76.9

Table 1. Geometric dimensions and material properties.

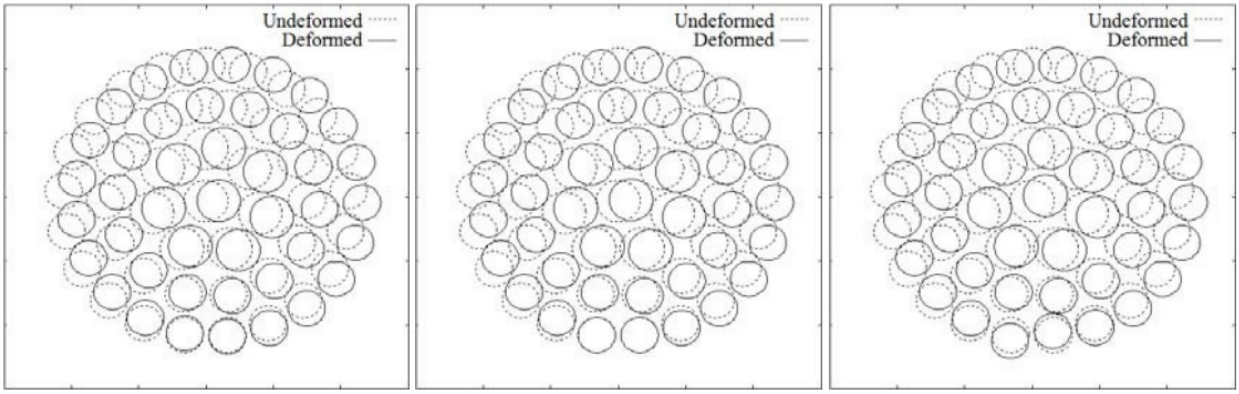

Figure 3. Scaled deviation of the rocking mode at different locations: bundle ends (left),bearing pads (middle), and midspan (right).

elastic DOFs are negligibly small except those on the two supporting rods at the bottom. To visualize the solution, the mode shape of the small deviation is shown in Figure 3. The total displacement, which is the static deformation superposed with the scaled deviation eigenvector, is shown in Figure 4. The mode exhibits a rocking motion in terms of the total displacement.

It is necessary to validate the accuracy of the meshing scheme and the numerical methods used in this paper against independent finite element code. Most general finite element codes do not incorporate the floating frame formulation; therefore comparison can be made on a conventional finite element model of the bundle structure. The above rigid-elasto model is degraded to a conventional finite element model by removing the floating frame formulation. The modal solution from this model is compared to that of an independent finite element model developed in ANSYS®ED 8.0 using straight beam elements. The comparison of the natural frequencies is shown in Table 2.

From the above solutions, it can be seen that the rigid body motion and gravity have a significant influence on the rocking frequency. The structural solution, which does not include the rigid body DOFs and the gravity terms, shows a frequency of 7.7 Hz, while the rigid-elasto solution shows a frequency of

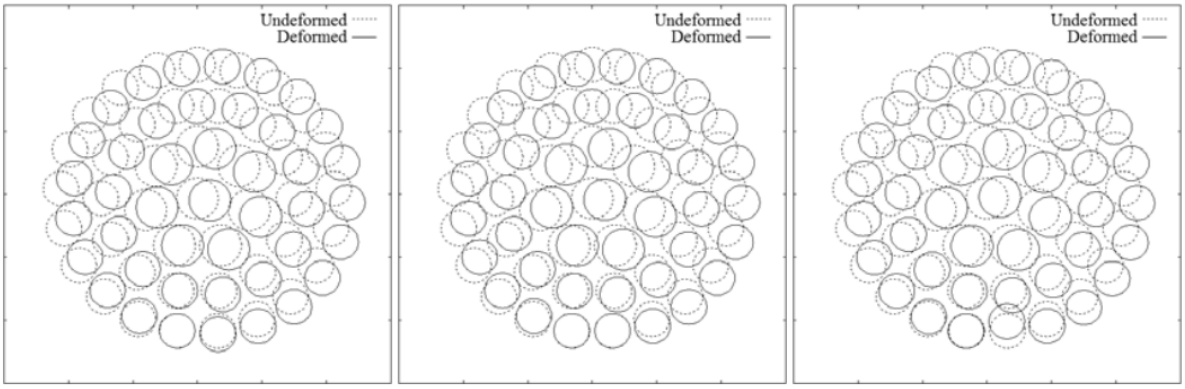

Figure 4. Scaled total displacement of the rocking mode at different locations: bundle ends (left), bearing pads (middle), and midspan (right).

Mode	Natural frequencies (Hz)	
	This paper	ANSYS ED 8.0
1	7.7	7.5
2	50.8	50.0
3	93.0	87.7
4	93.8	93.2
5	94.3	93.6
6	94.8	94.0

Table 2. Validation on the current finite element model (without floating frame formulation) against ANSYS ED 8.0

Mode	Frequencies (Hz)		Difference (%)
	With	Without	
1	6.1	7.7	20.8
2	50.4	50.8	0.8
3	91.9	93.0	1.2
4	93.8	93.8	0.0
5	94.2	94.3	0.1
6	94.4	94.8	0.4

Table 3. Influence of gravity. Frequencies are shown for with and without floating frame formulation and gravity.

6.1 Hz. The difference is 20.8%. It can be seen in Table 3 that the influence of gravity is only significant on the fundamental mode. This is because the fundamental mode is related to rigid body rotations and gravity does positive work when the bundle rocks from the equilibrium position to either side. The

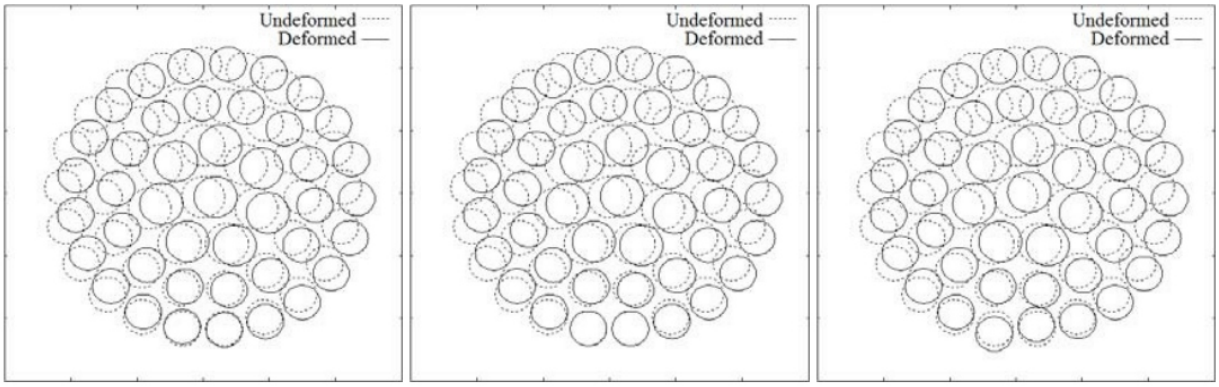

Figure 5. Scaled deformation of the rocking mode at different locations without floating frame formulation and nonlinear terms: bundle ends (left), bearing pads (middle), and midspan (right).

second mode is a pure vertical motion and the gravity work cancels itself in the motion. Higher modes are characterized by the bending deformation of the rods, and thus receive little influence from gravity. The fundamental mode of the structural solution is also shown in Figure 5 for comparison.

Although the influence of gravity is important, it needs to be clarified that the impact is delivered "indirectly". The major influence of gravity is enforced through the equilibrium solution hidden in the nonlinear terms $\partial \boldsymbol{S}/\partial \ddot{\boldsymbol{\delta}}$ and $\partial \boldsymbol{R}/\partial \tilde{\boldsymbol{q}}$, especially the latter. The $\partial \boldsymbol{R}_r/\partial \boldsymbol{u}_r$ term in $\partial \boldsymbol{R}/\partial \tilde{\boldsymbol{q}}$ can be further expressed as

$$\frac{\partial \boldsymbol{R}_r}{\partial \boldsymbol{u}_r} = \left[\boldsymbol{K}_{12} \frac{\partial \boldsymbol{u}_{fc}}{\partial \boldsymbol{u}_r} + \left(\frac{\partial \boldsymbol{u}_{fc}}{\partial \boldsymbol{u}_r} \right)^T \boldsymbol{K}_{21} + 2 \left(\frac{\partial \boldsymbol{u}_{fc}}{\partial \boldsymbol{u}_r} \right)^T \boldsymbol{K}_{22} \frac{\partial \boldsymbol{u}_{fc}}{\partial \boldsymbol{u}_r} \right]_{\tilde{\boldsymbol{q}}^0} + \left[\boldsymbol{u}_r^T \frac{\partial \boldsymbol{h}_i^A}{\partial \boldsymbol{u}_r} + \frac{\partial}{\partial \boldsymbol{u}_r} (\boldsymbol{h}_i^B \boldsymbol{u}_{fi}) + \boldsymbol{u}_r^T \frac{\partial \boldsymbol{h}_i^C}{\partial \boldsymbol{u}_r} \right]_{\tilde{\boldsymbol{q}}^0}, \quad (10)$$

where $\boldsymbol{h}_i^A$, $\boldsymbol{h}_i^B$, and $\boldsymbol{h}_i^C$ are the i-th rows of $(\partial \boldsymbol{u}_{fc}/\partial \boldsymbol{u}_r)^T \boldsymbol{K}_{21}$, $(\partial \boldsymbol{u}_{fc}/\partial \boldsymbol{u}_r)^T \boldsymbol{K}_{23}$, and $(\partial \boldsymbol{u}_{fc}/\partial \boldsymbol{u}_r)^T \boldsymbol{K}_{22}$, respectively. The terms in the second set of brackets in (10) contain the equilibrium solution which is a consequence of gravity. If this term is dropped, the rocking frequency will increase to a value which is almost identical to the structural solution. It should be noticed that the coupling term between the constraint DOF and the rigid body DOF terms $\boldsymbol{K}_{12}$ and $\boldsymbol{K}_{21}$ is actually zero; therefore, the corresponding terms in the second set of brackets are dominant. Even a small quantity in the second set of brackets may have a strong influence on the result. Dissimilarly to this, the contributions from the nonlinear terms in $\partial \boldsymbol{S}/\partial \ddot{\boldsymbol{\delta}}$ are very small compared to those from $\boldsymbol{M}_{12}$ and $\boldsymbol{M}_{21}$, and hence have little influence on the result.

Influences from the nonlinearity in the Euler rotation matrix $\boldsymbol{A}$, the derivative matrix $\boldsymbol{B}$, and the constraint equations are relatively small compared to the indirect influence of gravity. However, if the constraint equations are linearized so that $\partial \boldsymbol{u}_{fc}/\partial \boldsymbol{u}_r$ becomes a constant, then the derivatives of $\boldsymbol{h}_i^A$, $\boldsymbol{h}_i^B$, and $\boldsymbol{h}_i^C$ in (10) will become zero and hence the influence from gravity will be lost.

There is also a "direct" influence of gravity, the $\partial \boldsymbol{H}/\partial \tilde{\boldsymbol{q}}$ term. This represents the rate of change in the gravity-induced moment with respect to the displacement. Although this term is derived from the gravity potential, its impact is negligible in this application, because the rods in the bundle are almost evenly distributed. Numerical solution shows that the values of the elements in the $\partial \boldsymbol{H}/\partial \tilde{\boldsymbol{q}}$ term are a few orders lower in magnitude then those in the $\boldsymbol{K}_s$ and $\partial \boldsymbol{R}/\partial \tilde{\boldsymbol{q}}$ terms.

4. Experiment

An experiment was carried out to determine the rocking frequency of the bundle. Lateral oscillation in the horizontal direction of the bundle may be related to the rocking motion of the bundle. Its frequency can be obtained by monitoring the oscillatory motion of a point on the outer ring of the bundle near the end. Instead of using accelerometers, a noncontact displacement sensor is used for vibration measurement. This type of sensor is more sensitive to low frequency, relatively large displacement vibrations.

To measure the bundle vibration, a 43-rod bundle is placed inside a 4-inch PVC tube supported by strong steel columns, as shown in Figure 6. A noncontact differential variable reluctance transducer (MicroStrain NC-DVRT-1.5) is used to recode the lateral displacement of the bundle. The sensor detects the distance between a target object and the face of the transducer head. The reluctance of the coils within the sensor is changed when the face of the transducer is in close proximity to a ferrous or highly conductive material. The transducer outputs a voltage signal that is a nonlinear function of the distance. The typical repeatability of this transducer is ±2μm and the frequency range is 0 to 800 Hz. The trans ducer is mounted at one side of the tube near the end of the bundle. The transducer head penetrates the tube wall and approaches the rod around the 4 o'clock position. The initial gap from the head of the transducer is around 200μm for the best gain factor in the output. The time-domain voltage signal is sampled with a sampling rate of 5 kHz and recorded using a data acquisition system. The voltage signal is then converted to gap distance and analyzed using code written in Matlab to obtain the spectral information.

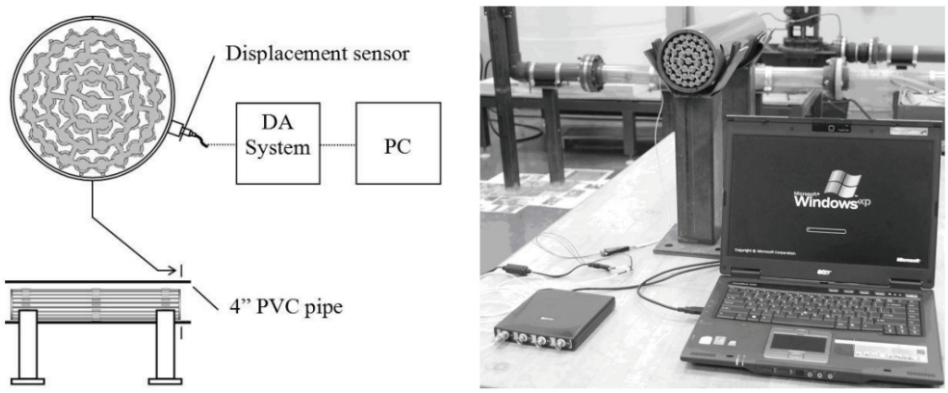

Figure 6. Experimental setup.

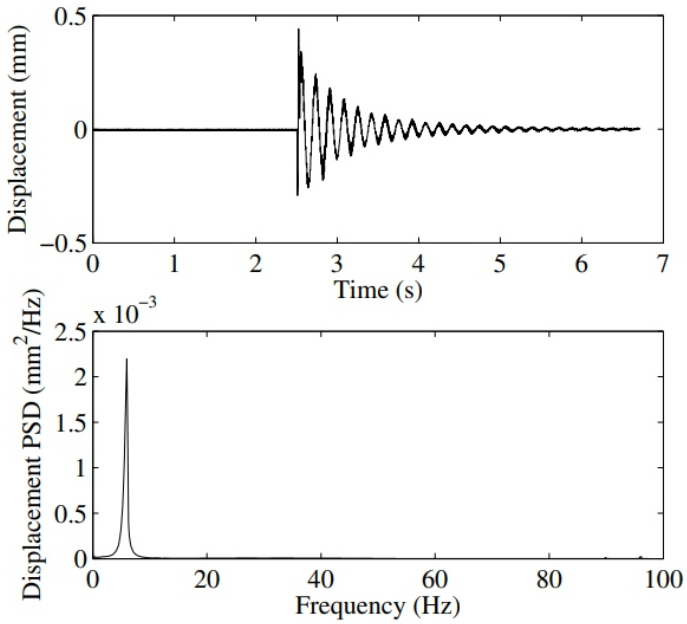

Figure 7. The response of the bundle to an impulse.

The response of the bundle to an impulse is recorded and analyzed. The time-domain displacement of the monitored point and its power spectral density are shown in Figure 7. The response of the rocking mode is found to be clear and free of noise from higher modes, such as the 90–100 Hz mode group corresponding to the first bending mode of the rods. The rocking mode frequency is 6.0 Hz. The damping ratio calculated from the difference between the peaks in the time-domain signal is about 0.05. For such a low damping ratio, the effect of damping on natural frequencies is negligible.

The tube is built from PVC, a material softer than steel. When the steel bearing pads contact the tube inner surface, the soft material will deform. This deformation leads to a contact stiffness and may have an influence on the fundamental frequency. It is necessary to examine the contact stiffness and compare it to the overall equivalent stiffness that relates to the bundle deformation with the current boundary conditions. The Boussinesq point contact solution [Johnson 1985] is used to estimate the order of magnitude of the normal contact stiffness kC. Based on the solution, the normal elastic deformation w at the contact location when a point object indents on a semiinfinite elastic space in the normal direction can be expressed as

$$w = \frac{2P(1-\nu)}{4\pi Gr}, \tag{11}$$

where P is the normal contact force, r is the contact point radius, G is the shear modulus of the elastic space (G = 1 GPa for PVC), and ν is the Poisson's ratio of the elastic space (ν = 0.41 for PVC). The order

of magnitude of the contact stiffness on one bearing pad can then be estimated as $kC,1 \sim P/w = \pi Gr/(1 - \nu) \approx 107$. The overall contact stiffness provided by the contact of the four bearing padsis $kC = 4kC,1 \sim 4 \times 107$. Because the most potential energy in the rocking mode comes from the deformation of the two rods that contact the tube through bearing pads, it is reasonable to compare kC with the equivalent stiffness of these rods. The equivalent stiffness can be conveniently estimated by dividing the weight of the bundle and the vertical displacement of its mass center from a static analysis.

The order of magnitude of the equivalent stiffness is obtained as $kE \sim 1 \times 106$, which is far smaller than kC. This indicates that the contact stiffness can be considered infinite and the tube can be regarded as rigid with regards to the lower bundle vibration modes.

5. Conclusions

The vibration of a 43-rod simulation CANDU fuel bundle horizontally placed in a supporting tube is studied through numerical models and experiments. The floating frame formulation and nonlinear constraint conditions are employed in a finite element model to predict the natural frequencies of the small-amplitude oscillations about the equilibrium position. The fundamental mode is found to be a low frequency rocking mode, which is a combination of rigid body motion and elastic deformation, but is dominated by the rigid body rotation about a bundle axis. Gravity is found to influence the rocking motion, and to reduce the frequency. The simulation results are in good agreement with experimental results.

References

[Cho et al. 2000] M.-S. Cho, K.-S. Sim, H. C. Suk, and S.-K. Chang, "Static strength analysis of CANDU-6 reactor fuel bundle", Nucl. Eng. Des. 200:3 (2000), 407–419.

[Horhoianu and Ionescu 2006] G. Horhoianu and D. V. Ionescu, "A finite element model for static strength analysis of CANDU fuel bundle", Kerntechnik 71:4 (2006), 203–207.

[Johnson 1985] K. L. Johnson, Contact mechanics, Cambridge University Press, London, 1985.

[Judah 1992] J. Judah, "Overview of fuel inspections at the Darlington nuclear generating station", pp. 1–22 in 3rd International CNS CANDU Fuel Conference (Chalk River, 1992), Canadian Nuclear Society, Toronto, ON, 1992.

[Meirovitch 2001] L. Meirovitch, Fundamentals of vibrations, McGraw-Hill, Boston, 2001.

[Reddy 1984] J. N. Reddy, "A simple higher-order theory for laminated composite plates", J. Appl. Mech. (ASME) 51:4 (1984), 745–752.

[Schwab and Meijaard 2002] A. L. Schwab and J. P. Meijaard, "Small vibrations superimposed on a prescribed rigid body motion", Multibody Syst. Dyn. 8:1 (2002), 29–49.

[Shabana 2005] A. A. Shabana, Dynamics of multibody systems, 3rd ed., Cambridge University Press,

Cambridge, 2005.

[Yu and Wen 2007] S. D. Yu and D. C. Wen, "An efficient plate finite element and its application to three-dimensional deformations of CANDU fuel endplate rings", Nucl. Eng. Des. 237:4 (2007), 342–352.

[Zhang and Yu 2010a] X. Zhang and S. D. Yu, "Theoretical and experimental investigations of oscillatory rolling motion of a rod bundle inside a tube", in Proceedings of 11th Pan-American Congress of Applied Mechanics (PACAM XI) (Foz do Iguaçu, 2010), edited by A. R. Aguiar and T. L. Attard, Brazilian Society of Mechanical Sciences and Engineering, Rio de Janeiro, 2010. Paper #PAC0512.

[Zhang and Yu 2010b] X. Zhang and S. D. Yu, "A thick plate model for bending and twisting of CANDU fuel endplates", Nucl. Eng. Des. 240:10 (2010), 2565–2570.

Instructions for Authors

Essentials for Publishing in this Journal

1 Submitted articles should not have been previously published or be currently under consideration for publication elsewhere.

2 Conference papers may only be submitted if the paper has been completely re-written (taken to mean more than 50%) and the author has cleared any necessary permission with the copyright owner if it has been previously copyrighted.

3 All our articles are refereed through a double-blind process.

4 All authors must declare they have read and agreed to the content of the submitted article and must sign a declaration correspond to the originality of the article.

Submission Process

All articles for this journal must be submitted using our online submissions system. http://enrichedpub.com/ . Please use the Submit Your Article link in the Author Service area.

Manuscript Guidelines

The instructions to authors about the article preparation for publication in the Manuscripts are submitted online, through the e-Ur (Electronic editing) system, developed by **Enriched Publications Pvt. Ltd**. The article should contain the abstract with keywords, introduction, body, conclusion, references and the summary in English language (without heading and subheading enumeration). The article length should not exceed 16 pages of A4 paper format.

Title

The title should be informative. It is in both Journal's and author's best interest to use terms suitable. For indexing and word search. If there are no such terms in the title, the author is strongly advised to add a subtitle. The title should be given in English as well. The titles precede the abstract and the summary in an appropriate language.

Letterhead Title

The letterhead title is given at a top of each page for easier identification of article copies in an Electronic form in particular. It contains the author's surname and first name initial .article title, journal title and collation (year, volume, and issue, first and last page). The journal and article titles can be given in a shortened form.

Author's Name

Full name(s) of author(s) should be used. It is advisable to give the middle initial. Names are given in their original form.

Contact Details

The postal address or the e-mail address of the author (usually of the first one if there are more Authors) is given in the footnote at the bottom of the first page.

Type of Articles

Classification of articles is a duty of the editorial staff and is of special importance. Referees and the members of the editorial staff, or section editors, can propose a category, but the editor-in-chief has the sole responsibility for their classification. Journal articles are classified as follows:

Scientific articles:

1. Original scientific paper (giving the previously unpublished results of the author's own research based on management methods).

2. Survey paper (giving an original, detailed and critical view of a research problem or an area to which the author has made a contribution visible through his self-citation);

3. Short or preliminary communication (original management paper of full format but of a smaller extent or of a preliminary character);

4. Scientific critique or forum (discussion on a particular scientific topic, based exclusively on management argumentation) and commentaries. Exceptionally, in particular areas, a scientific paper in the Journal can be in a form of a monograph or a critical edition of scientific data (historical, archival, lexicographic, bibliographic, data survey, etc.) which were unknown or hardly accessible for scientific research.

Professional articles:

1. Professional paper (contribution offering experience useful for improvement of professional practice but not necessarily based on scientific methods);
2. Informative contribution (editorial, commentary, etc.);
3. Review (of a book, software, case study, scientific event, etc.)

Language

The article should be in English. The grammar and style of the article should be of good quality. The systematized text should be without abbreviations (except standard ones). All measurements must be in SI units. The sequence of formulae is denoted in Arabic numerals in parentheses on the right-hand side.

Abstract and Summary

An abstract is a concise informative presentation of the article content for fast and accurate Evaluation of its relevance. It is both in the Editorial Office's and the author's best interest for an abstract to contain terms often used for indexing and article search. The abstract describes the purpose of the study and the methods, outlines the findings and state the conclusions. A 100- to 250-Word abstract should be placed between the title and the keywords with the body text to follow. Besides an abstract are advised to have a summary in English, at the end of the article, after the Reference list. The summary should be structured and long up to 1/10 of the article length (it is more extensive than the abstract).

Keywords

Keywords are terms or phrases showing adequately the article content for indexing and search purposes. They should be allocated heaving in mind widely accepted international sources (index, dictionary or thesaurus), such as the Web of Science keyword list for science in general. The higher their usage frequency is the better. Up to 10 keywords immediately follow the abstract and the summary, in respective languages.

Acknowledgements

The name and the number of the project or programmed within which the article was realized is given in a separate note at the bottom of the first page together with the name of the institution which financially supported the project or programmed.

Tables and Illustrations

All the captions should be in the original language as well as in English, together with the texts in illustrations if possible. Tables are typed in the same style as the text and are denoted by numerals at the top. Photographs and drawings, placed appropriately in the text, should be clear, precise and suitable for reproduction. Drawings should be created in Word or Corel.

Citation in the Text

Citation in the text must be uniform. When citing references in the text, use the reference number set in square brackets from the Reference list at the end of the article.

Footnotes

Footnotes are given at the bottom of the page with the text they refer to. They can contain less relevant details, additional explanations or used sources (e.g. scientific material, manuals). They cannot replace the cited literature.
The article should be accompanied with a cover letter with the information about the author(s): surname, middle initial, first name, and citizen personal number, rank, title, e-mail address, and affiliation address, home address including municipality, phone number in the office and at home (or a mobile phone number). The cover letter should state the type of the article and tell which illustrations are original and which are not.